SLAC – 325
UC – 34D
(E)

A STUDY OF LOW Q^2 RADIATIVE BHABHA SCATTERING*

Dean Albert Karlen

Stanford Linear Accelerator Center
Stanford University
Stanford, California 94305

March 1988

Prepared for the Department of Energy
under contract number DE-AC03-76SF00515

---

* Ph.D. Dissertation

Abstract

This thesis presents a study of electron-positron scattering, via nearly real photon exchange, where in the process one or more high energy photons are produced. The motivations behind the work are twofold. Firstly, the study is a sensitive test of the theory of electron-photon interactions, quantum electrodynamics. A deviation from the theory could indicate that the electron is a composite particle. Secondly, a thorough understanding of this process is necessary for experiments to be done in the near future at the Stanford Linear Collider and the LEP facility at CERN.

Calculations for the process to third and fourth order in perturbation theory are described. Methods for simulating the process by a Monte Carlo event generator are given. Results from the calculations are compared to data from the Mark II experiment at the PEP storage ring. The ratio of measured to calculated cross sections are

$$0.993 \pm 0.017 \pm 0.015 \quad \text{and} \quad 0.99 \pm 0.16 \pm 0.08$$

for final states with one and two observed photons respectively, where the first errors are statistical and the second systematic. The excellent agreement verifies the calculations of the fourth order radiative correction. No evidence for electron substructure is observed.

Acknowledgments

My first word of thanks must go to all the people that have contributed to the Mark II collaboration in the past. When I joined the group in 1983, the experiment was already well underway. The results presented in this thesis owe much to the quality work performed by these people.

I acknowledge my advisors, Bob Hollebeek and Jonathan Dorfan, for their encouragement through my graduate career. Many thanks go to my co-workers that made the many days at SLAC enjoyable, especially Charlotte Hee, Bruce LeClaire, Spencer Klein, René Ong, and Tom Steele. I especially thank Keith Riles for discussing physics and sharing an apartment over the years, and for a critical proof reading of this thesis.

The many new people that have joined the Mark II collaboration in the past few years for SLC have revitalized the group. It was exciting to be associated with this dynamic team. My analysis benefited from the work by many of these newcomers, in particular Barrett Milliken and Chris Hawkes for their careful study of the liquid argon calorimeter. I also thank Giovanni Bonvicini and others for discussions of radiative corrections, an important physics topic at the SLC.

A graduate student's life is usually concentrated on work, and mine proved to be no exception. There was some relief, however, and I thank Allan Miller for introducing me into the percussion sections of various groups in the area, and Dave Blockus for introducing me to the many hilly bicycle routes. The weekly SLAC soccer and volleyball games were welcome interruptions to the many hours spent in front of a terminal.

Most of all, I would like to thank my parents and family for their understanding and love, which helped me complete this thesis.

Contents

Tables

Figures

1

Introduction

High energy physics is the study of fundamental particles and their interactions. The list of particles thought to be fundamental that have been discovered so far is rather large – five quarks: up (u), down (d), strange (s), charm (c), bottom (b), and six leptons: electron (e), muon (μ), tau (τ), electron neutrino (ν_e), muon neutrino (ν_μ), tau neutrino (ν_τ). The particles influence each other by electromagnetic, weak, strong, and gravitational forces. Gravity is so weak that it is often ignored in particle physics. The remaining interactions are described by the exchange of gauge bosons,

$$\left.\begin{array}{ll} \text{photon } (\gamma) & \} \text{ electromagnetic} \\ W,\ Z & \} \text{ weak} \\ \text{gluon } (g) & \} \text{ strong} \end{array}\right\} \text{electro-weak} \Bigg\} \ ?$$

The electromagnetic and weak interactions are unified in the electro-weak theory of Glashow[1], Weinberg[2], and Salam[3]. Much work is in progress to include also the strong and gravitational forces, to form a grand unified theory[4].

The fundamental particles can be organized into a 'periodic' table according to the interactions in which they take part,

$$\left.\begin{array}{ll} \text{quarks} & \left\{\begin{array}{lll} \text{u} & \text{c} & \\ \text{d} & \text{s} & \text{b} \end{array}\right\} \text{strong} \\ \text{leptons} & \left\{\begin{array}{lll} e & \mu & \tau \\ \nu_e & \nu_\mu & \nu_\tau \end{array}\right. \end{array}\right\} \text{electro-weak}$$

The table is further organized according to the electromagnetic charges of the particles: $+\frac{2}{3}$, $-\frac{1}{3}$, -1, and 0 unit charges for the four rows, respectively. The columns of the table represent the three generations, each consisting of a quark doublet and lepton doublet, except for the third generation where the top quark partner for the bottom quark has not yet been discovered. Ordinary matter is composed of particles of the first generation only. The particles of the other generations are more massive and decay into the particles of the first generation, with the possible exception of the neutrinos which may be massless and stable.

This thesis is a precise study of the electromagnetic interactions of electrons at high energies. The particular process studied is low Q^2 radiative Bhabha scattering, where an electron and positron scatter, via the exchange of an almost real photon, and produce one or more high energy photons. The calculation and measurement of this process is not only a test of the theory of electron-photon interactions, quantum electrodynamics (QED), but is also an application of QED necessary for future experiments.

The picture presented at the beginning of this chapter is not complete, and some of the missing pieces may be within the reach of upcoming experiments at the Stanford Linear Collider and the LEP facility at CERN. Some searches for new physics involve the study of very low multiplicity events in electron positron collisions, in which radiative Bhabha scattering is the dominant background such as neutrino counting experiments[5–8] and some searches for supersymmetry[8–12] and compositeness[13,14].

In neutrino counting experiments, the decay rate of the Z into light weakly interacting neutral particles is directly found by measuring the single photon cross section, from the process shown in fig. 1.1. If there is a fourth generation with a neutrino lighter than half the mass of the Z, the measured cross section for this process would be enhanced by over 20%. The measurement is also sensitive to other neutral weakly interacting particles that have not yet been observed, such as neutral supersymmetric particles. Another signal for supersymmetry, is the observation of single electron events, arising from the production and decay of a supersymmetric

electron. A possible signal of electron compositeness, is the production of an excited state and its decay into an electron photon pair. Radiative Bhabha scattering where one or both electrons escape detection at low angles is the largest background to all of these signals, and hence must be well understood.

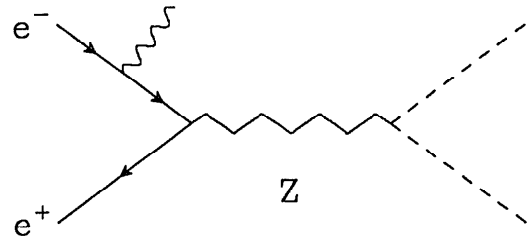

Figure 1.1. A Feynman diagram of the process measured by single photon experiments. An electron radiates the photon before annihilating with an positron and producing a Z. The Z decays into weakly interacting neutral particles which are undetected.

Other applications of this work include the measurement of luminosity[15], and the study of detector resolutions. It is important to note that the weak interaction does not significantly affect this process; therefore the calculations are useful over a wide range of energies.

1.1 Outline of thesis

In chapter 2, calculations of low Q^2 radiative Bhabha scattering and its radiative correction are described. The results of these calculations are complicated differential cross section formulae which cannot be integrated analytically. A numerical approach is required, and in chapter 3, the Monte Carlo methods of integrating these cross sections are described. Results from the Monte Carlo event generator program for some typical experiments are given. The majority of this work has already been published[16].

The remainder of the thesis deals with measurements made with the MarkII detector to confirm these calculations. Chapter 4 describes the MarkII detector as it existed between the years 1981 through 1984, while it was stationed at the PEP storage ring at SLAC. In chapter 5, the analysis of the data taken with the MarkII detector is described. The integrated luminosity is determined with wide

angle Bhabha scattering, allowing a precise comparison of the measured single and double radiative Bhabha cross sections with the calculations of chapter 2 and 3. Also, a search for excited states of the electron is performed as a test of electron compositeness.

2

QED calculations

Quantum Electro-Dynamics (QED) is one of the most successful theories ever developed. It accurately predicts a wide variety of phenomena[17,18] from low energy tests (anomalous magnetic moments) and atomic measurements (Lamb shift, hyperfine structure)[19] to high energy scattering processes[20]. Its remarkable success has made QED a model for the weak and the strong forces.

The perturbative approach in calculating QED processes is possible duc to the smallness of the coupling constant, $\alpha \approx 1/137$. In high energy scattering processes, sufficient accuracy is usually obtained by including diagrams only up to the next to lowest order. This chapter discusses the calculation of radiative Bhabha scattering in the lowest order, as well as the radiative correction to the process, in the case of low Q^2 scattering.

2.1 Lowest order calculations

To the lowest order, radiative Bhabha scattering,

$$e^+(p_+)\, e^-(p_-) \rightarrow e^+(q_+)\, e^-(q_-)\, \gamma(k) \quad , \tag{2.1}$$

is described by the eight diagrams of fig. 2.1. The exact cross section was first calculated in refs. 21 and 22. In the ultrarelativistic limit, in which initial and final state energies are assumed much larger than m_e and no two fermion lines are nearly

collinear, the cross section may be written in a compact form[23]:

$$
\begin{aligned}
d^5\sigma_{\rm BK} &= \frac{\alpha^3}{\pi^2 s}\, A\, W_{\rm IR}\, W_{\rm m}\, d^5\Gamma \ , \\
A &= (ss'(s^2+s'^2)+tt'(t^2+t'^2)+uu'(u^2+u'^2))/(ss'tt') \ , \\
W_{\rm IR} &= \frac{s}{x_1x_2}+\frac{s'}{y_1y_2}-\frac{t}{x_1y_1}-\frac{t'}{x_2y_2}+\frac{u}{x_1y_2}+\frac{u'}{x_2y_1} \ , \\
W_{\rm m} &= 1-\frac{m_e^2(s-s')}{s^2+s'^2}\left(\frac{s'}{x_1}+\frac{s'}{x_2}+\frac{s}{y_1}+\frac{s}{y_2}\right) \ , \\
d^5\Gamma &= \delta^4(p_+ + p_- - q_+ - q_- - k)\frac{d^3\mathbf{q}_+}{2q_+^0}\frac{d^3\mathbf{q}_-}{2q_-^0}\frac{d^3\mathbf{k}}{2k^0} \ , \\
s &= (p_+ + p_-)^2 \ , \qquad t = (p_+ - q_+)^2 \ , \qquad u = (p_+ - q_-)^2 \ , \\
s' &= (q_+ + q_-)^2 \ , \qquad t' = (p_- - q_-)^2 \ , \qquad u' = (p_- - q_+)^2 \ , \\
x_1 &= p_+\cdot k \ , \quad x_2 = p_-\cdot k \ , \quad y_1 = q_+\cdot k \ , \quad y_2 = q_-\cdot k \ .
\end{aligned}
\tag{2.2}
$$

This equation, however, does not include all mass dependent terms that are significant in the region studied here. When the positron is scattered at a small angle, the invariant, t, can become of order m_e^2. Then a term containing m_e^2/t^2 could be of the same order as a term containing $1/t$.

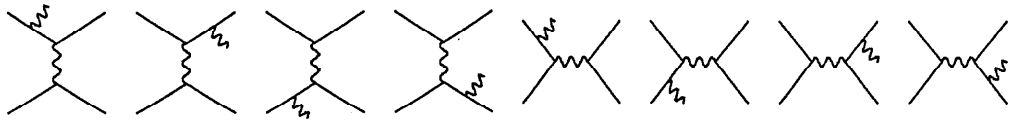

Figure 2.1. Lowest order diagrams for radiative Bhabha scattering.

To find the m_e^2/t^2 term, I calculate the cross section from the only two diagrams that could contribute, shown in fig. 2.2. Following the convention of Bjorken and

Drell[24], the matrix element is

$$\mathcal{M} = ie^3 \bar{u}(q_-) \frac{1}{(p_+ - q_+)^2} \epsilon^\nu M_{\nu\mu}\, u(p_-)\, \bar{v}(p_+)\, \gamma^\mu\, v(q_+) \ ,$$
$$M_{\nu\mu} = \gamma_\mu \frac{(\not{p}_- - \not{k} + m_e)}{(p_- - k)^2 - m_e^2} \gamma_\nu + \gamma_\nu \frac{(\not{q}_- + \not{k} + m_e)}{(q_- + k)^2 - m_e^2} \gamma_\mu \ . \tag{2.3}$$

Squaring, averaging over initial state polarizations, and summing over final state polarizations gives,

$$\frac{1}{4} \sum_{\text{pol}} |\mathcal{M}|^2 = \frac{-e^6}{16(2m_e)^4 t^2} \mathrm{Tr}\left[(\not{q}_- + m_e) M_{\nu\mu} (\not{p}_- + m_e) M^{\rho\nu}\right]$$
$$\times\ \mathrm{Tr}\left[(-\not{p}_+ + m_e)\gamma^\mu (-\not{q}_+ + m_e)\gamma_\rho\right] \ . \tag{2.4}$$

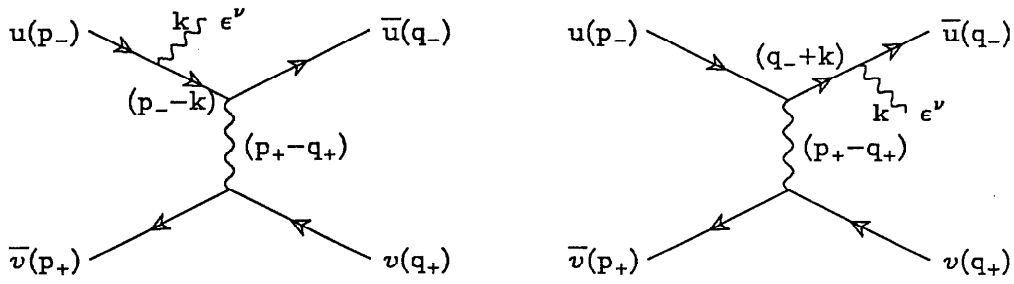

Figure 2.2. Two lowest order diagrams used to calculate the term containing m_e^2/t.

The symbolic manipulation program, REDUCE[25], is used to evaluate the traces, resulting in the cross section given by,

$$d^5\sigma = \frac{\alpha^3}{\pi^2 s} \left(s^2 + s'^2 + u^2 + u'^2 + \frac{m_e^2}{t} Z\right) \left(\frac{-1}{x_2 y_2 t}\right) d^5\Gamma \ ,$$
$$Z = 8(x_2^2 + y_2^2) + \frac{(ss' - uu')^2}{x_2 y_2} + m_e^2\, \mathrm{O}(s) + t\, \mathrm{O}(s) \ , \tag{2.5}$$

where $\mathrm{O}(s)$ refers to a function of order s or less.

Consider the second term of Z, and define

$$\varrho = \tfrac{1}{4}(ss' - uu') = (p_+ \cdot p_-)(q_+ \cdot q_-) - (p_+ \cdot q_-)(q_+ \cdot p_-) + m_e^2 (p_+ + q_+) \cdot (p_- + q_-) \ , \quad (2.6)$$

where the first two terms nearly cancel to give a small result. To evaluate this invariant expression in the lab system, let $q_+ = (1-\varepsilon)p_+ + \delta$, where $0 < \varepsilon < 1$, δ is a four-vector, and $\boldsymbol{\delta} \perp \mathbf{p}_+$. Then,

$$\begin{aligned} &\varrho = (p_+ \cdot p_-)(\delta \cdot q_-) - (p_+ \cdot q_-)(\delta \cdot p_-) + m_e^2 (p_+ + q_+) \cdot (p_- + q_-) \ , \\ &\delta \cdot q_- = \delta^0 q_-^0 - \boldsymbol{\delta} \cdot \mathbf{q}_- \ , \qquad \delta \cdot p_- = \delta^0 p_-^0 \ , \\ &\delta^0 = \frac{\varepsilon m_e^2 - \frac{1}{2}t}{p_+^0} \ , \qquad \boldsymbol{\delta}^2 = \delta^{0\,2} - \varepsilon^2 m_e^2 - (1-\varepsilon)t \ . \end{aligned} \quad (2.7)$$

After substitution it is seen that,

$$\varrho = \sqrt{-t}\, \mathrm{O}(s^{\frac{3}{2}}) + m_e\, \mathrm{O}(s^{\frac{3}{2}}) \ , \quad (2.8)$$

and so the second term in Z can be ignored since it only contains terms of order $t\,\mathrm{O}(s)$ and $m_e^2\,\mathrm{O}(s)$.

As a check of the m_e^2 term, a previous calculation[21] was found to give the same result in the ultrarelativistic limit as eqn. 2.5. The term containing m_e^2/t'^2 is simply found by applying charge conjugation,

$$p_+ \leftrightarrow p_- \quad , \quad q_+ \leftrightarrow q_- \quad (2.9)$$

to the result. The lowest order cross section is then given by,

$$d^5\sigma_{e^+e^-\to e^+e^-\gamma} = d^5\sigma_{\mathrm{BK}} - \frac{\alpha^3}{\pi^2 s} 8 m_e^2 \left(\frac{(x_2^2 + y_2^2)}{x_2 y_2 t^2} + \frac{(x_1^2 + y_1^2)}{x_1 y_1 t'^2} \right) d^5\Gamma \ . \quad (2.10)$$

This modification can change total cross sections that include 0° electron scattering by as much as 5% or more.

2.2 Radiative correction

To describe radiative Bhabha scattering more accurately, it is necessary to include the next order of the perturbative expansion. The virtual correction, shown in fig. 2.3 a-d, and double radiative Bhabha scattering, fig. 2.3e, need to be included in the calculation. However, this is a very complex problem since there are more than 150 diagrams in this next order. The cross section for double radiative Bhabha scattering, described by 40 diagrams, has been evaluated[26-28], but a calculation of the virtual correction to radiative Bhabha scattering has not yet been published.

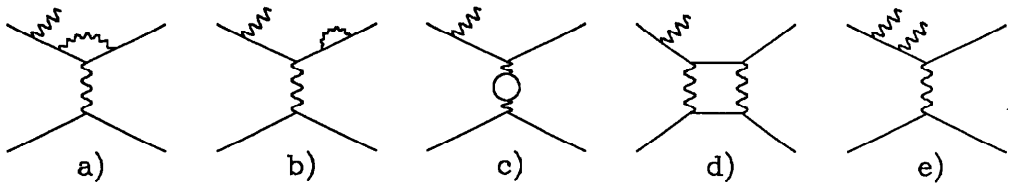

Figure 2.3. Some representative diagrams of the next order correction to radiative Bhabha scattering: a) Vertex correction; b) Electron self energy correction; c) Vacuum polarization; d) Box diagrams; e) Double radiative Bhabha scattering.

Since calculations for the exact treatment of radiative Bhabha scattering to order α^4 are not available, I make use of the Equivalent Photon Approximation[29,30] (EPA) for the next order correction. The method, described in the next section, only includes the diagrams shown in fig. 2.4. This is expected to be a good approximation of the total radiative correction, as I argue in the remainder of this section. Many of the arguments rely on the requirement that one of the electrons is scattered at a small angle, and thus the method cannot be used for general radiative Bhabha scattering.

The annihilation diagrams are not included, but since they are significantly suppressed by the requirement that a final state electron be below some small angle, this is a good approximation. This is confirmed in section 3.4 by comparing the lowest order result with and without the annihilation diagrams. In the following discussion, only the class of diagrams where the photon is radiated from the electron while the positron is deflected only slightly will be considered. The charge conjugate diagrams can be included separately, simply by reversing the charges. The interference between

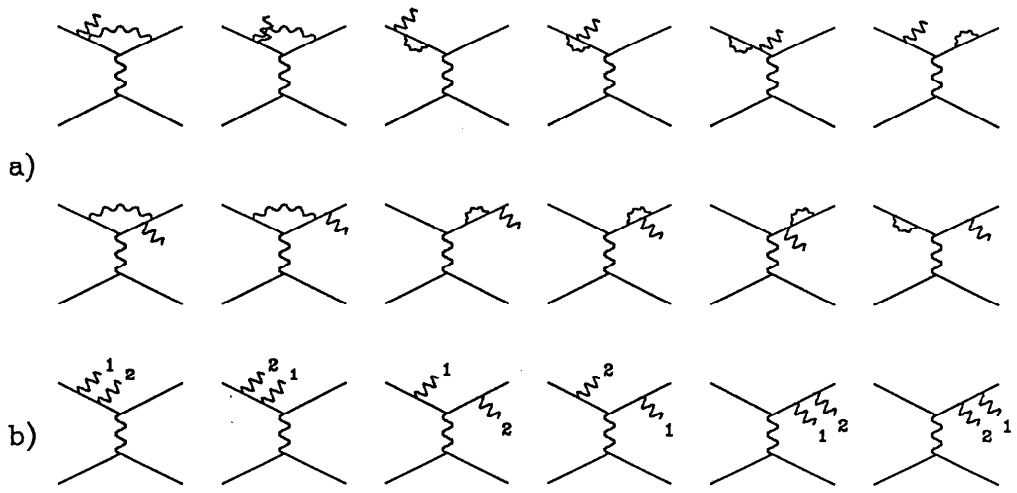

Figure 2.4. Diagrams included in the approximation of the radiative correction to radiative Bhabha scattering: a) Virtual correction diagrams; b) Double radiative Bhabha diagrams.

these two sets of diagrams will thus not be included, but the net effect is expected to be small due to the peaking behavior. That is, the contribution to the total cross section is seen in lowest order to be strongly peaked at 0° scattering of the electron or positron with little overlap. Again this is confirmed in section 3.4 for the lowest order.

Figure 2.4 contains no radiative correction to the positron. The radiation spectrum from this leg is proportional to[31]

$$\left(\frac{\hat{e}\cdot p_+}{k\cdot p_+}-\frac{\hat{e}\cdot q_+}{k\cdot q_+}\right)^2 , \tag{2.11}$$

where k is the momentum of a photon with polarization $\hat{e}$. In the limit that $\mathbf{p}_+$ and $\mathbf{q}_+$ are collinear, the radiation spectrum goes to zero and so it is expected that the radiative correction to the positron will be small. An explicit calculation[32] of the radiative correction to the multiperipheral two photon diagrams of the process, $e^+e^- \rightarrow e^+e^-\mu^+\mu^-$, confirms this. This process is similar to the one studied here, except that both the electron and the positron are predominately scattered at small angles. The total correction is seen to be very small (on the order of 1%). Only when one or both of the electrons are required to be scattered at large angles, does the

correction become more important. A recent calculation of the radiative correction to the equivalent photon spectrum shows that the virtual and real photon emission terms cancel exactly[33].

Vacuum polarization, shown in fig. 2.3c, is not included but has a small effect since the cross section is dominated by small angle scattering of the positron, where $Q^2 = O(m_e^2)$. Box diagrams, an example of which is shown in fig. 2.3d, are also not included. This contribution is very difficult to calculate[34], but results from similar processes indicate that although they have an infrared divergence that is cancelled by interference of soft photon emission, the net effect of the diagrams is small. Tsai[35] has shown that the combined effect of all such diagrams in Møller scattering at 1 GeV is a correction of the order 0.1% or less. Box diagrams in two photon processes have also been evaluated[34] and the total correction was found to be less than the 0.01% level.

2.3 Application of the EPA to radiative Bhabha scattering

This section discusses the application of the EPA to radiative Bhabha scattering. The lowest order process is treated, as a simple example, which is compared to the exact calculation as a check of the accuracy of the method. The method of calculating the dominant radiative correction, by including the diagrams of fig. 2.4, is also described.

2.3.1 Lowest order calculation

When the positron scatters at a small angle, the diagrams of fig. 2.2 dominate and the EPA factorizes the process into a part describing photon emission from the positron,

$$e^+(p_+) \rightarrow e^+(q_+)\ \gamma(\tilde{k})\ , \tag{2.12}$$

and a part describing photon scattering,

$$\gamma(\tilde{k})\ e^-(p_-) \rightarrow \gamma(k)\ e^-(q_-)\ . \tag{2.13}$$

The cross section can be written as,

$$d^5\sigma^{\rm EPA}_{e^+e^-\to e^+e^-\gamma} = d^3n_{e^+\to e^+\gamma}\, d^2\sigma_{\gamma e^-\to\gamma e^-} \ , \tag{2.14}$$

where $d^3n_{e^+\to e^+\gamma}$ is the equivalent photon spectrum and $d^2\sigma_{\gamma e^-\to\gamma e^-}$ is the Compton cross section. Equation 2.14 is valid only when the positron scatters at a small angle, corresponding to quasi-real photon exchange. More precisely, ref. 29 shows that if $Q^2 \ll \tilde{s}$, where $\sqrt{\tilde{s}}$ is the center of mass energy of the γe^- system, then eqn. 2.14 is valid with the equivalent photon spectrum given by,

$$\begin{aligned} dn(Q^2,\hat{s}) &= \frac{\alpha}{\pi}\frac{d\hat{s}}{\hat{s}}\frac{dQ^2}{Q^2}\left[1-\frac{\hat{s}}{s}+\frac{1}{2}\left(\frac{\hat{s}}{s}\right)^2-\frac{m_e^2}{Q^2}\left(\frac{\hat{s}}{s}\right)^2\right] \ , \\ Q^2 &= -t \ , \qquad \hat{s} = 2p_-\cdot\tilde{k} \ , \end{aligned} \tag{2.15}$$

Using the relations,

$$\begin{aligned} t &= -2E_bq_+^0\left[(1-\cos\theta_{q_+})+\frac{2m_e^2}{s}\left(\frac{E_b-q_+^0}{q_+^0}\right)^2\right] \ , \\ \tilde{s} &= (p_-+\tilde{k})^2 = 4E_b(E_b-q_+^0)+m_e^2 \ , \end{aligned} \tag{2.16}$$

and that $\hat{s}\approx\tilde{s}$, the equivalent photon spectrum can be written in terms of the degrees of freedom of the positron,

$$\begin{aligned} d^3n_{e^+\to e^+\gamma} &= \frac{2\alpha}{\pi^2}\frac{1}{-t}\frac{s}{\tilde{s}}\left[1-\frac{\tilde{s}}{s}+\frac{1}{2}\left(\frac{\tilde{s}}{s}\right)^2+\frac{m_e^2}{t}\left(\frac{\tilde{s}}{s}\right)^2\right]d^3\Gamma_n \ , \\ d^3\Gamma_n &= \frac{dt\, d\tilde{s}\, d\phi_{q_+}}{4s} = \frac{d^3\mathbf{q_+}}{2q_+^0} \ . \end{aligned} \tag{2.17}$$

The differential cross section for Compton scattering, eqn. 2.13, was first calculated by Klein and Nishina[36]. Their result may be written as,

$$\begin{aligned} d^2\sigma_{\gamma e^-\to\gamma e^-} &= \frac{4\alpha^2}{\tilde{s}}\,U\,d^2\Gamma \ , \\ d^2\Gamma &= \delta^4(p_-+\tilde{k}-q_--k)\,\frac{d^3\mathbf{q_-}}{2q_-^0}\frac{d^3\mathbf{k}}{2k} \ , \end{aligned} \tag{2.18}$$

where U appears in ref. 37 as,

$$U = \left(\frac{x_2}{y_2} + \frac{y_2}{x_2}\right) - 2m_e^2\left(\frac{1}{x_2} - \frac{1}{y_2}\right) + m_e^4\left(\frac{1}{x_2} - \frac{1}{y_2}\right)^2 . \tag{2.19}$$

By taking the dominant terms in U, substituting eqns. 2.17 and 2.18 into eqn. 2.14, and identifying $\tilde{k} = p_+ - q_+$, the EPA radiative Bhabha cross section formula is found to be,

$$d^5\sigma^{\mathrm{EPA}}_{e^+e^-\to e^+e^-\gamma} = \frac{\alpha^3}{\pi^2 s} 4(x_2^2 + y_2^2)\left(\frac{s^2 + (s-\tilde{s})^2}{\tilde{s}^2} + \frac{2m_e^2}{t}\right)\left(\frac{-1}{x_2 y_2 t}\right) d^5\Gamma . \tag{2.20}$$

Using the relations,

$$\begin{aligned} \tilde{s} &= s + u' + t - 3m_e^2 , \\ x_2 &= -\tfrac{1}{2}(s' + u + t) + 2m_e^2 , \\ y_2 &= \tfrac{1}{2}(s + u' + t) - 2m_e^2 , \end{aligned} \tag{2.21}$$

the cross section can be written as,

$$d^5\sigma^{\mathrm{EPA}}_{e^+e^-\to e^+e^-\gamma} = \frac{\alpha^3}{\pi^2 s}\left(s^2 + s'^2 + u^2 + u'^2 + \frac{m_e^2}{t} 8(x_2^2 + y_2^2) + Y\right)\left(\frac{-1}{x_2 y_2 t}\right) d^5\Gamma ,$$

$$Y = 2\frac{su - s'u'}{(s+u')^2}(ss' - uu') + m_e^2\,\mathrm{O}(s) + t\,\mathrm{O}(s) . \tag{2.22}$$

This result agrees with the t channel cross section, eqn. 2.5, apart from the extra term, Y. This term is, however, small since it contains $(ss' - uu') = \sqrt{-t}\,\mathrm{O}(s^{\frac{3}{2}})$, as shown in section 2.1. The m_e^2/t^2 term is the same as found before in the t channel calculation.

In the lowest order, it is seen that the EPA reproduces the t channel calculation in the limit of small t. In order to check that the EPA is valid in particular regions under study, section 3.4 numerically compares eqn. 2.20 with the exact cross section given by eqn. 2.10.

2.3.2 *Radiative correction*

It is well known that the correction to a process due to soft real photon emission is infrared divergent. This is seen in eqn. 2.11 which diverges as $k \to 0$. There is

also an infrared divergence associated with virtual photon emission. When virtual and real photon corrections are combined, the result is finite[31,38]. In the context of simulating a process with the next order radiative correction, it is useful to consider separately two classes of events. In the first class, the next order photon is deemed to be undetectable given the finite resolution of an experiment. In this class, the lowest order process and the complete virtual correction is combined with real photon emission integrated up to a cutoff energy, $E_{\rm cut}$. This analytic correction, free from divergences, can be written in the form

$$d\sigma^{\rm vs} = (1+\delta)\, d\sigma^0 \,, \tag{2.23}$$

where $d\sigma^0$ is the lowest order cross section and δ depends on the photon cutoff energy. In the second class of events, the next order photon is considered detectable but the cross section has no divergence, since a minimum photon energy is imposed.

The analytic correction term, δ, for radiative Bhabha scattering is the same as that for Compton scattering in the region of validity of eqn. 2.14, since

$$\begin{aligned} d^5\sigma^{\rm vs}_{e^+e^-\to e^+e^-\gamma} &= d^3 n_{e^+\to e^+\gamma}\, d^2\sigma^{\rm vs}_{\gamma e^-\to \gamma e^-} \\ &= d^3 n_{e^+\to e^+\gamma}\, d^2\sigma_{\gamma e^-\to \gamma e^-}(1+\delta) \\ &= d^5\sigma_{e^+e^-\to e^+e^-\gamma}(1+\delta) \,. \end{aligned} \tag{2.24}$$

The radiative correction to Compton scattering was first calculated by Brown and Feynman[37]. They, however, chose to define the soft photon cutoff energy in the frame where the electron is initially at rest and thus their equation of the integrated soft real photon emission cannot be used. Since $E_{\rm cut}$ is defined in the rest frame of the electron, the soft photon cutoff is highly anisotropic in the laboratory system. Also, their equation is valid only if[39] $E_{\rm cut} \ll m_e$, which is very much less than a typical experimental resolution. Instead, the evaluation of δ in the γe center of mass system by Mork[40] will be used. The boost from this system to the laboratory system is

not as large as from the electron rest frame and the expression is valid if $E_{\rm cut} \ll \sqrt{s}$. After correcting four misprints[41], the analytic correction term is given by,

$$\begin{aligned}\delta = -\frac{\alpha}{\pi U}\Big\{ & 2(1-2y)U\ln(2\frac{E_{\rm cut}}{m_e}) + \frac{\pi^2}{6}\left(4 - 3t - \frac{1}{t} - \frac{2}{E^4t^3}\right) \\ & + 4(2-U)y^2 - 4y + \tfrac{3}{2}U + \frac{2}{E^2t^2} + 4\left(1-\frac{1}{2t}\right)\ln^2 E \\ & + \left(2t + \frac{1}{t} - 2 + \frac{2}{E^4t^3}\right) L_2(1-E^2t) \\ & + \left[2 - 5t - \frac{2}{t} + 4y\left(\frac{2}{t} + t - 2\right)\right]\ln E \\ & - \tfrac{1}{2}U\ln^2(1-t) - UL_2(t) \\ & + \left[1 - \frac{2}{t} - \frac{2}{E^2t^2} - \frac{\frac{1}{2}E^2}{1-E^2t} + 4y\left(t - 1 + \frac{1}{2t}\right)\right]\ln(E^2t)\Big\}\,,\end{aligned} \tag{2.25}$$

$$E = \frac{\sqrt{s}}{m_e}\,, \quad t = \tfrac{1}{2}(1+\beta_-\cos\theta_k)\,, \quad y = \ln\left[E\sin(\theta_k/2)\right]\,, \quad U = t + 1/t,$$

where $L_2(x)$ is the second order Spence function,

$$L_2(x) = -\int_0^1 \frac{\ln u}{\frac{1}{x} - u}\, du\,. \tag{2.26}$$

The cross section for the process $e^+e^- \to e^+e^-\gamma\gamma$, in which both photons have energies greater than $E_{\rm cut}$ in the γe center of mass system, can be obtained by another application of the EPA

$$d^8\sigma_{e^+e^-\to e^+e^-\gamma\gamma} = d^3n_{e^+\to e^+\gamma}\, d^2\sigma_{\gamma e^-\to e^-\gamma\gamma}\,, \tag{2.27}$$

The cross section for double Compton scattering,

$$\gamma(\tilde{k})\, e^-(p_-) \to e^-(q_-)\,\gamma(k)\,\gamma(k_s)\,, \tag{2.28}$$

was first calculated by Mandle and Skyrme[42]. Their result may be written in the form,

$$d^5\sigma_{\gamma e^-\to e^-\gamma\gamma} = \frac{\alpha^3}{\pi^2\tilde{s}}\frac{X_{\rm MS}}{m_e^2}\,d^5\Gamma\ ,$$
$$d^5\Gamma = \delta^4(p_- + \tilde{k} - q_- - k - k_s)\,\frac{d^3\mathbf{q_-}}{2q_-^0}\,\frac{d^3\mathbf{k}}{2k^0}\,\frac{d^3\mathbf{k_s}}{2k_s^0}\ , \tag{2.29}$$

where $X_{\rm MS}$ appears in ref. 43 as,

$$X_{\rm MS} = 2(ab-c)\,[(a+b)(x+2) - (ab-c) - 8] - 2x(a^2+b^2) - 8c$$
$$+ \frac{4x}{AB}\left[(A+B)(x+1) - (aA+bB)(2+z\frac{1-x}{x}) + x^2(1-z) + 2z\right]$$
$$- 2\rho[ab + c(1-x)]$$

$$a = \sum_1^3 \frac{1}{\kappa_i}\ ,\quad b = \sum_1^3 \frac{1}{\kappa_i'}\ ,\quad c = \sum_1^3 \frac{1}{\kappa_i\kappa_i'}\ ,$$
$$x = \sum_1^3 \kappa_i\ ,\quad y = \sum_1^3 \kappa_i'\ ,\quad z = \sum_1^3 \kappa_i\kappa_i'\ , \tag{2.30}$$
$$A = \kappa_1\kappa_2\kappa_3\ ,\quad B = \kappa_1'\kappa_2'\kappa_3'\ ,\quad \rho = \sum_1^3\left(\frac{\kappa_i}{\kappa_i'} + \frac{\kappa_i'}{\kappa_i}\right)\ ,$$

$$m_e^2\kappa_1 = p_-\cdot k\ ,\quad m_e^2\kappa_2 = p_-\cdot k_s\ ,\quad m_e^2\kappa_3 = -p_-\cdot\tilde{k}\ ,$$
$$m_e^2\kappa_1' = -q_-\cdot k\ ,\quad m_e^2\kappa_2' = -q_-\cdot k_s\ ,\quad m_e^2\kappa_3' = q_-\cdot\tilde{k}\ .$$

The cross section for double radiative Bhabha scattering,

$$e^+(p_+)\,e^-(p_-)\ \to e^+(q_+)\,e^-(q_-)\,\gamma(k)\,\gamma(k_s)\ , \tag{2.31}$$

is found using the equivalent photon spectrum, eqn. 2.17, to be,

$$d^8\sigma_{e^+e^-\to e^+e^-\gamma\gamma} = \frac{\alpha^4}{\pi^4 s}\frac{X_{\rm MS}}{m_e^2}\frac{1}{-t}\left(\frac{s^2+(s-\tilde{s})^2}{\tilde{s}^2} + \frac{2m_e^2}{t}\right)d^8\Gamma\ ,$$
$$d^8\Gamma = \delta^4(p_+ + p_- - q_+ - q_- - k - k_s)\,\frac{d^3\mathbf{q_+}}{2q_+^0}\,\frac{d^3\mathbf{q_-}}{2q_-^0}\,\frac{d^3\mathbf{k}}{2k^0}\,\frac{d^3\mathbf{k_s}}{2k_s^0}\ , \tag{2.32}$$

where $\sqrt{\tilde{s}}$ is the γe center of mass energy.

3

Monte Carlo event generation

Monte Carlo event generation refers to the simulation of a process by producing sets of four-vectors distributed according to a theoretical cross section. An accurate comparison of a theoretical cross section with experimental data usually requires such a program, due to complicated detector acceptance and resolution functions. By passing the four-vectors through a detector simulation program, the imperfections of the detector can be taken into account. This chapter will discuss some general techniques of Monte Carlo event generation and their application to radiative Bhabha scattering, using the cross section formulae described in chapter 2.

3.1 General techniques

The term, Monte Carlo, implies that random chance is involved in the procedure. In the following sections, this random factor comes in the form of random numbers, denoted by λ, equidistributed in the interval $(0, 1)$. Such numbers produced by a computational algorithm are strictly not random since the sequence can be predicted, and are hence called pseudo-random. The most commonly used algorithm, the multiplicative congruential method, usually suffices for the methods presented below, although it must be used with care[44–46]. The results presented in this chapter, are based on random sequences generated with this method.

The rejection method is the most straight forward procedure of generating a sample of a quantity, x, according to a distribution, $D(x)$. If x is to be in the

interval, $(x_{\min}, x_{\max})$, then a trial element, x_{trial}, is generated at random,

$$x_{\text{trial}} = x_{\min} + \lambda_1 (x_{\max} - x_{\min}) \ , \tag{3.1}$$

and the trial element is accepted if

$$D(x_{\text{trial}}) \geq \lambda_2 D_{\max} \ . \tag{3.2}$$

If $D_{\max} \geq D(x)$ for all x in the interval, then it is clear that x is chosen with a probability proportional to $D(x)$. After n_{accept} values have been generated, the integral of the distribution can be calculated by

$$\int_{x_{\min}}^{x_{\max}} D(x)\, dx \simeq \frac{n_{\text{accept}}}{n_{\text{trial}}} D_{\max}(x_{\max} - x_{\min}) \ . \tag{3.3}$$

This procedure is however not efficient if the distribution has any large peaks. In this case, $D_{\max}$ may need to be very large due to only a small part of the interval, and consequently eqn. 3.2 would seldom be satisfied.

An alternative to the above method, is the inversion procedure. With this approach, the element x is found by solving

$$\lambda = \int_{x_{\min}}^{x} D(\tilde{x})\, d\tilde{x} \Big/ \int_{x_{\min}}^{x_{\max}} D(\tilde{x})\, d\tilde{x} \ , \tag{3.4}$$

and is fully efficient since each random number generates one element, x. For non-trivial distributions such as those defined by QED cross sections, eqn. 3.4 seldom has an analytic solution. The procedure can still be used however, by first replacing the exact cross section, $d\sigma$, by an approximate, $d\sigma^{\text{a}}$, for which eqn. 3.4 can be solved. A trial event generated by this approximate cross section, is accepted with a probability that is proportional to the event weight, $w = d\sigma/d\sigma^{\text{a}}$. This is accomplished by choosing a maximum weight, $w_{\max}$, before the event generation, and accepting the trial event if, $w > \lambda\, w_{\max}$. The maximum weight $w_{\max}$ must be larger than any event weight, but must not be too large, or the efficiency of this procedure will be low. This

procedure then generates an event sample according to the exact cross section, $d\sigma$, and the total cross section is found by,

$$\sigma = \frac{n_{\text{accept}}}{n_{\text{trial}}} w_{\max} \sigma^{\text{a}} \ . \tag{3.5}$$

The relative error of this calculation is simply,

$$\left(\frac{\delta\sigma}{\sigma}\right)^2 = \frac{1}{n_{\text{accept}}} - \frac{1}{n_{\text{trial}}} \ , \tag{3.6}$$

The rejection method, described above, can be considered a special case of this method, where the choice for the approximate distribution is a constant.

The total cross section can be evaluated more efficiently by using the weights of all trial events,

$$\begin{aligned} \sigma &= \int \frac{d^n\sigma}{d^n\sigma^{\text{a}}} d^n\sigma^{\text{a}} \\ &= \int_0^1 \cdots \int_0^1 w(\lambda_1, \lambda_2, \ldots, \lambda_n)\, \sigma^{\text{a}} \prod_{i=1}^{n} d\lambda_i \\ &= \sigma^{\text{a}} \frac{1}{n_{\text{trial}}} \sum_{j=1}^{n_{\text{trial}}} w_j = \sigma^{\text{a}} \langle w \rangle \ , \end{aligned} \tag{3.7}$$

so that the total cross section is identified with the mean of the weight distribution. The error in the mean, is calculated as usual,

$$\left(\frac{\delta\sigma}{\sigma}\right)^2 = \frac{1}{n_{\text{trial}}} \frac{\langle (w - \langle w \rangle)^2 \rangle}{\langle w \rangle^2} = \frac{1}{n_{\text{trial}}} \frac{\langle w^2 \rangle - \langle w \rangle^2}{\langle w \rangle^2} \ . \tag{3.8}$$

Since $\langle w \rangle = \dfrac{n_{\text{accept}}}{n_{\text{trial}}} w_{\max}$,

$$\left(\frac{\delta\sigma}{\sigma}\right)^2 = \frac{\langle w^2 \rangle}{n_{\text{accept}}\, w_{\max} \langle w \rangle} - \frac{1}{n_{\text{trial}}} \ , \tag{3.9}$$

and since $\langle w^2 \rangle \leq w_{\max} \langle w \rangle$, the error in this calculation is smaller than the error given in eqn. 3.6. Similarly, event distributions can be found more efficiently by using the weighted trial events, rather than the unweighted final sample.

The approximate cross section chosen for a particular problem should map all the large variations (peaks) of the exact cross section, if the event generation procedure is to be efficient. This can be simplified by utilizing symmetries of the exact cross section. For example, if the exact cross section is symmetric about interchange of particles 1 and 2, then any peak exhibited by 1 is also present for 2. In this case, the approximate cross section need only contain the peak of particle 1. After the event generation, the sample can then be symmetrized so that both peaks are sampled as explained below. Let,

$$d\sigma(1,2) = d\sigma(2,1) \quad , \quad d\sigma_s^a(1,2) = \tfrac{1}{2}d\sigma^a(1,2) + \tfrac{1}{2}d\sigma^a(2,1) \; , \tag{3.10}$$

then the event generation is described by,

$$\begin{aligned} d\sigma(1,2) = \frac{d\sigma(1,2)}{d\sigma^a(1,2)}d\sigma^a(1,2) &= \frac{d\sigma(1,2)}{d\sigma_s^a(1,2)}d\sigma_s^a(1,2) \\ &= \tfrac{1}{2}w_s d\sigma^a(1,2) + (1 \leftrightarrow 2) \; , \end{aligned} \tag{3.11}$$

where w_s is the symmetrized weight. So after generating according to $d\sigma^a$ and weighting with w_s, half of the events should have 1 and 2 reversed.

3.2 Event generation for the three body final state

This section describes the method of generating events for the lowest order radiative Bhabha scattering process. The event generation according to the cross section corrected for virtual and soft real photon emission is a simple modification of the procedure.

The order α^3 cross section, eqn. 2.2, is too complicated for the simple inversion technique, so an approximate form will be used to generate trial events. Using eqn. 2.5 in place of eqn. 2.2 should be a very good approximation since the t channel contribution dominates the part of the cross section under study. By integrating over

$\mathbf{q}_-$ and k^0, and making the further approximations,

$$\begin{aligned} s^2 + s'^2 + u^2 + u'^2 &\approx 4s^2 \ , \\ 2E_b - q_+^0 + |\mathbf{q}_+| \cos \angle(\mathbf{k}, \mathbf{q}_+) &\approx 2(E_b - q_+^0) \ , \end{aligned} \tag{3.12}$$

I use for an approximate cross section

$$\begin{aligned} d^5\sigma^{\mathrm{a}}_{e^+e^-\to e^+e^-\gamma} &= \frac{\alpha^3}{2\pi^2} \frac{q_+^0}{(1+c+\epsilon)(E_b - q_+^0)^2} \frac{-1}{t} \, d\,|\mathbf{q}_+| \, d\Omega_{q_+} \, d\Omega_k \ , \\ t &= -2E_b q_+^0 \left((1 - \cos\theta_{q_+}) + \epsilon / z_+^{0\,2} \right) \ , \\ c &= \cos\theta_k \ , \qquad \epsilon = \frac{2m_e^2}{s} \ , \qquad z_+^0 = \frac{q_+^0}{E_b - q_+^0} \ , \end{aligned} \tag{3.13}$$

where all angles are measured with respect to $\mathbf{p}_+$. Note that the approximate cross section does not treat positrons and electrons equally, unlike the exact cross section. This asymmetry is corrected in the event generation, as described in eqn. 3.11.

The limits of integration for the five phase space variables, $|\mathbf{q}_+|$, θ_{q_+}, ϕ_{q_+}, θ_k, and ϕ_k, must be determined from information that describes the detector acceptance and veto and the event configuration. The photon and electron acceptances are defined by minimum angles with respect to the beam line, $\theta_{\gamma\,\mathrm{min}}$ and $\theta_{e\,\mathrm{min}}$, and minimum energies, $E_{\gamma\,\mathrm{min}}$ and $E_{e\,\mathrm{min}}$. Veto angles for photons and electrons are given by the angles, $\theta_{\gamma\,\mathrm{veto}}$ and $\theta_{e\,\mathrm{veto}}$. The event configuration specifies the combination of final state particles that are in the acceptance, with the remaining below the veto. Since I am interested in event samples with at least one electron below the veto, the three possible configurations are $e\gamma$, single γ and single e. All veto angles need not be less than the acceptance angles, however the combination of all the parameters must not allow a collinear final state.

Using these parameters, the limits for all the phase space variables are immediately determined, except for $|\mathbf{q}_+|$. The approximate cross section, eqn. 3.13, diverges as $q_+^0 \to E_b$, but this can occur only for a collinear final state, which is excluded.

Hence it is necessary to calculate the maximum value that q_+^0 can take, given the acceptance and veto parameters. Noting that the three final state particles are coplanar with the beam line for the topologies that maximize q_+^0, as shown in fig. 3.1, there are only three parameters required to determine this maximum value of q_+^0. For the single γ configuration, the kinematics of fig. 3.1c are easily solved, giving

$$E_b - q^0_{+\max} = E_b \left(\frac{E_{\gamma\,\min} \sin^2 \frac{1}{2}(\theta_{\gamma\,\min} - \theta_{e\,\mathrm{veto}})}{E_b - E_{\gamma\,\min} \cos^2 \frac{1}{2}(\theta_{\gamma\,\min} - \theta_{e\,\mathrm{veto}})} \right) , \tag{3.14}$$

with a similar equation applying for the single e configuration. The $e\gamma$ configuration has a more complicated boundary defined by the four parameters, $E_{\gamma\,\min}$, $E_{e\,\min}$, $\theta_{\gamma\,\min}$, and $\theta_{e\,\min}$. The kinematics are solved for each of the twelve topologies given by the two diagrams in fig. 3.1a-b and the six pairs of the four parameters. The maximum value for q_+^0 is given by the largest value from those topologies of the twelve that are fully consistent with the criteria.

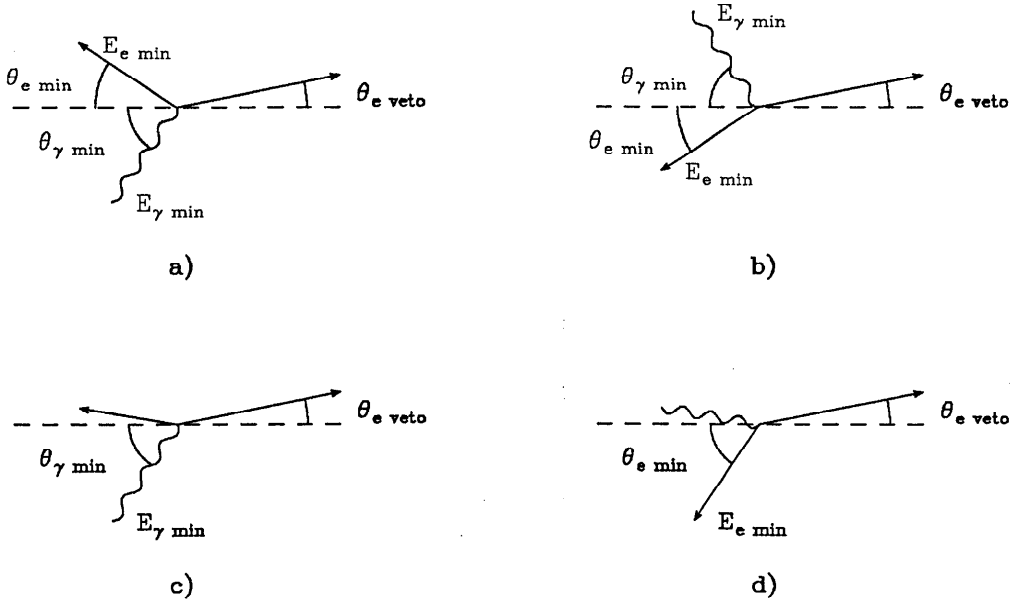

Figure 3.1. Event topologies that maximize q_+^0. The dashed line represents the beam axis. a-b) $e\gamma$ configuration. $\theta_{e\,\mathrm{veto}}$ and pairs of the remaining quantities determine $q^0_{+\max}$; c) single γ configuration. d) single e configuration.

Once the limits of integration are determined, the techniques described in the previous section are used to generate the phase space variables. From eqn. 3.13, the

distribution of q_+^0 and $\cos\theta_{q+}$ is given by

$$D(q_+^0, \cos\theta_{q+})\, d\,|\mathbf{q}_+|\; d\cos\theta_{q+} = \frac{q_+^0}{(E_b - q_+^0)^2}\left(\frac{-1}{t}\right) d\,|\mathbf{q}_+|\; d\cos\theta_{q+}\ . \tag{3.15}$$

The distribution of q_+^0 alone, found by integrating over the positron scattering angle, θ_{q+}, between 0 and the veto angle, $\theta_{e\,\mathrm{veto}}$, is given by

$$D(z_+^0)dz_+^0 = \frac{2}{s}\frac{q_+^0}{|\mathbf{q}_+|}\ln\left[1 + \frac{(1-\cos\theta_{e\,\mathrm{veto}})}{\epsilon}z_+^{0\,2}\right] dz_+^0\ . \tag{3.16}$$

Equation 3.4 cannot be solved for this distribution, so z_+^0 is generated by the rejection procedure and since $D(z_+^0)$ is quite flat, the method is efficient. Once z_+^0 is found, the second degree of freedom, θ_{q+}, has the distribution given by eqn. 3.15 which can be used with the inversion procedure. The solution to eqn. 3.4 is

$$1 - \cos\theta_{q+} = \frac{\epsilon}{z_+^{0\,2}}\left(\left[1 + \frac{(1-\cos\theta_{e\,\mathrm{veto}})}{\epsilon}z_+^{0\,2}\right]^{\lambda_2} - 1\right)\ . \tag{3.17}$$

Similarly, the angle of the photon, θ_k, is generated by

$$1 + \cos\theta_k + \epsilon = (1 + \cos\theta_{\max} + \epsilon)\left(\frac{1 + \cos\theta_{\min} + \epsilon}{1 + \cos\theta_{\max} + \epsilon}\right)^{\lambda_3}\ , \tag{3.18}$$

where $\theta_{\min} = \theta_{\gamma\,\min}$ and $\theta_{\max} = \pi - \theta_{\gamma\,\min}$, for the $e\gamma$ and single γ configurations, and $\theta_{\min} = \pi - \theta_{\gamma\,\mathrm{veto}}$ and $\theta_{\max} = \pi$, for the single e configuration. The final degrees of freedom for the three body final state are simply

$$\phi_k = 2\pi\lambda_4\ , \qquad \text{and} \qquad \phi_{q+} = 2\pi\lambda_5\ . \tag{3.19}$$

Since the approximate cross section is not symmetric about charge conjugation, the event sample is symmetrized as described in the previous section. For one half of the accepted events, the momenta are reversed; $\mathbf{q}_+ \leftrightarrow -\mathbf{q}_-$ and $\mathbf{k} \leftrightarrow -\mathbf{k}$.

To generate an event sample that includes the correction due to virtual and soft real photon emission, requires a modification of the event weight, $w^{\mathrm{vs}} = (1+\delta)w$,

where δ is given in eqn. 2.25. The event sample so produced, is combined with the four body final state sample, which is generated separately as shown below, to produce an event sample correct to order α^4.

3.3 Event generation for the four body final state

Four-vectors for the process, $e^+e^- \to e^+e^-\gamma\gamma$, are generated with methods similar to the three body generation. An approximation of the double radiative Bhabha cross section is found by using an approximate form for the double Compton cross section[37]

$$d^5\sigma_{\gamma e^- \to e^-\gamma\gamma} \approx \frac{\alpha}{4\pi^2}\left(\frac{p_-}{p_-\cdot k_s} - \frac{q_-}{q_-\cdot k_s}\right)^2 \frac{d^3\mathbf{k_s}}{k_s^o}\, d^2\sigma_{\gamma e^- \to \gamma e^-} \ , \tag{3.20}$$

which is valid for $k_s \ll \sqrt{\tilde{s}}$, the γe center of mass energy. This equation is approximated further, and the EPA is used to give,

$$d^8\sigma^{\mathrm{a}}_{e^+e^- \to e^+e^-\gamma\gamma} = d^3\sigma^{\mathrm{a}}_s\, d^5\sigma^{\mathrm{a}}_{e^+e^- \to e^+e^-\gamma} \ ,$$

$$d^3\sigma^{\mathrm{a}}_s = \frac{\alpha}{4\pi^2}\frac{1}{k_s^{o2}}\left(\frac{1}{1-c_{p_-}+\epsilon} + \frac{1}{1-c_{-k}+\epsilon}\right) f(k_s^o,\tilde{s})\,\frac{d^3\mathbf{k_s}}{k_s^o} \ ,$$

$$c_{p_-} = \cos\angle(\mathbf{k_s},\mathbf{p_-}) \ , \quad c_{-k} = \cos\angle(\mathbf{k_s},-\mathbf{k}) \ , \quad f(k_s^o,\tilde{s}) = \left(1 - \frac{k_s^o}{\frac{1}{2}\sqrt{\tilde{s}}} + \epsilon_s\right)^{-1} \ , \tag{3.21}$$

where $d^5\sigma^{\mathrm{a}}_{e^+e^- \to e^+e^-\gamma}$ is given in eqn. 3.13 and $d^3\sigma^{\mathrm{a}}_s$ is evaluated in the γe center of mass system. The function, $f(k_s^o,\tilde{s})$, has been included to approximate better the peaking behavior when $k_s^o \approx \frac{1}{2}\sqrt{\tilde{s}}$ in the γe center of mass system, and ϵ_s is some arbitrary small parameter.

The upper limit of integration of $|\mathbf{q_+}|$ for the $e\gamma$ configuration is affected when a second photon is included. The kinematics are again solved for the two topologies shown in fig. 3.1a-b, this time allowing a second photon to be present. The result is

$$E_b - q^0_{+\max} =$$

$$\frac{E_bE_1\sin^2\frac{1}{2}(\theta_1+\theta_{e\,\mathrm{veto}}) + E_bE_2\sin^2\frac{1}{2}(\theta_2-\theta_{e\,\mathrm{veto}}) - E_1E_2\sin^2\frac{1}{2}(\theta_1+\theta_2)}{E_b - E_1\cos^2\frac{1}{2}(\theta_1+\theta_{e\,\mathrm{veto}}) - E_2\cos^2\frac{1}{2}(\theta_2-\theta_{e\,\mathrm{veto}})} \ , \tag{3.22}$$

where $E_1 = E_{\gamma\,\mathrm{min}}, \theta_1 = \theta_{\gamma\,\mathrm{min}}$ and $E_2 = E_{e\,\mathrm{min}}, \theta_2 = \theta_{e\,\mathrm{min}}$ for fig. 3.1a and reversed for fig. 3.1b. For the single γ and single e configurations, the maximum of q_+^0 occurs for $k_s = 0$, so eqn. 3.14 can still be used.

Since the lowest order approximate cross section factors out in eqn. 3.21, apart from $f(k_s^0, \tilde{s})$ where $\tilde{s}$ depends on q_+^0, algorithms from the lowest order event generation can be used in the double radiative event generation. Of the five degrees of freedom that describe the three body final state, only the energy of the positron, q_+^0, needs to be treated differently. The distribution for q_+^0 is now given by

$$D(z_+^0)dz_+^0 = \frac{2}{s}\frac{q_+^0}{|\mathbf{q}_+|}\ln\left[1 + \frac{(1-\cos\theta_{e\,\mathrm{veto}})}{\epsilon}z_+^{0\,2}\right]\ln r\, dz_+^0 \,,$$
$$r = \frac{\frac{1}{2}\sqrt{\tilde{s}}(1+\epsilon_s) - E_{\mathrm{cut}}}{\epsilon_s E_{\mathrm{cut}}} \,. \tag{3.23}$$

and as before, z_+^0 is generated with the rejection technique. After generating the four remaining degrees of freedom of the three body final state, only the 3 degrees of freedom of the second photon remain to be generated according to $d^3\sigma_s^{\mathrm{a}}$ given in eqn. 3.21. These are generated in a modified γe center of mass system as described below.

The use of the EPA cross section given in eqn. 2.32 to calculate the event weight, requires the photon in the γe scattering process to be real. This is only true, however, when the positron scatters at 0° and hence some approximation as to the definition of the γe center of mass system must be made. The invariant mass of the γe system recoiling against the positron, is a function only of the positron energy,

$$W^2 = 4E_b(E_b - q_+^0) + m_e^2 \,. \tag{3.24}$$

I thus define the center of mass system to be a real photon and electron colliding with a center of mass energy, $\sqrt{\tilde{s}} = W$. The velocity of this system relative to the lab system is,

$$\boldsymbol{\beta} = -\mathbf{q}_+/(2E_b - q_+^0) \,. \tag{3.25}$$

This approximation, used only in the evaluation of the invariant products in $X_{\rm MS}$ of eqn. 2.30, is exact in the limit of 0° positron scattering.

Given the definition of the center of mass system, the energy of the second photon in this system is generated by the following algorithm:

$$k_s^{\rm cm} = \frac{1}{2}\sqrt{\tilde{s}}\,\frac{1+\epsilon_s}{1+\epsilon_s r^{\lambda_6}} \ . \tag{3.26}$$

The approximate cross section peaks when the second photon is nearly collinear with the initial or final state electron. Since the choice of the axis about which θ_{k_s} and ϕ_{k_s} are measured is arbitrary, by choosing the axis to be along the $\mathbf{p}_-$ and $-\mathbf{k}$ alternatively, by another random number, both peaks are handled in accordance with eqn. 3.21. (This simple procedure motivated the form of the approximate cross section.) These angles are generated by

$$1+\cos\theta_{k_s}^{\rm cm}+\epsilon = \epsilon\left(\frac{2+\epsilon}{\epsilon}\right)^{\lambda_7} \ , \qquad \text{and} \qquad \phi_{k_s}^{\rm cm} = 2\pi\lambda_8 \ . \tag{3.27}$$

The $-\mathbf{k}$ axis is chosen to handle the $\mathbf{q}_-$ collinearity pole, instead of the $\mathbf{q}_-$ axis itself, because, the direction of $-\mathbf{k}$ is fixed when the second photon is generated. When k_s^0 is small or $\mathbf{k_s}$ is nearly collinear with $\mathbf{q}_-$, then $\mathbf{q}_-$ and $-\mathbf{k}$ are nearly parallel.

The remainder of this section describes the method of solving the kinematics for the four body final state. The definition of the γe center of mass coordinate system, K'', is indicated in fig. 3.2. In order to simplify the equations, the solution is found for the case, $\phi_{q_+} = 0$, after which a rotation in the lab system is applied to all four vectors. The y coordinate is therefore invariant for the three systems shown in fig. 3.2.

The rotation, θ_r, where

$$\begin{aligned} \sin\theta_r &= \frac{(1+\xi)\sin\theta_{q_+}}{\sqrt{2(1+\xi)(1-cos\theta_{q_+}+\xi^2)}} \\ \xi &= (\gamma-1)(1-\cos\theta_{q_+})-\gamma(1-\beta+\beta\epsilon) \ , \end{aligned} \tag{3.28}$$

brings the $-z''$ axis parallel with $\mathbf{p}'_-$, the initial electron's momentum in the modified γe center of mass frame. Solving the kinematics of the $e\gamma\gamma$ final state in this frame is

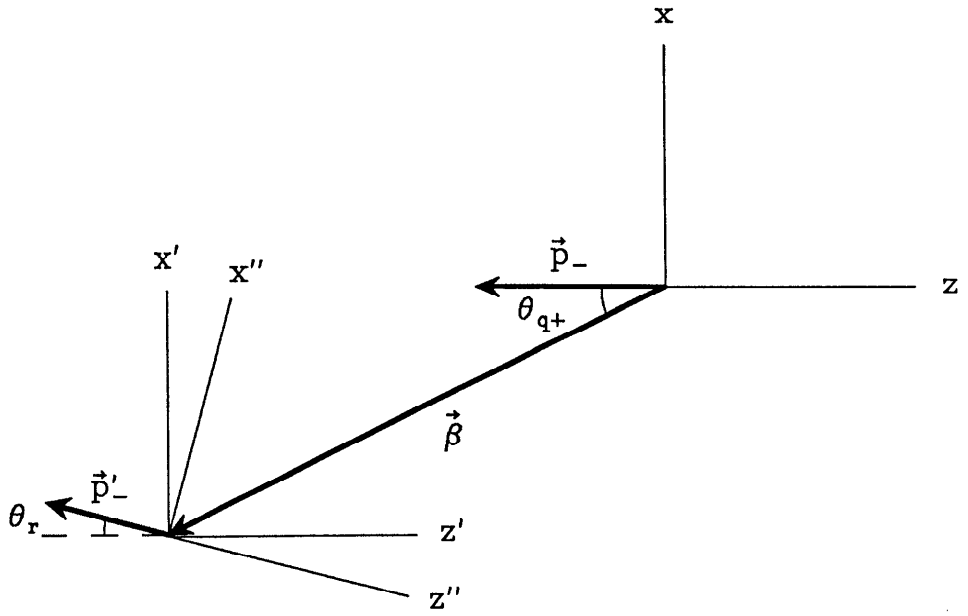

Figure 3.2. Definition of γe center of mass coordinate system, K''. The velocity of the K' system with respect to the K system is β, given by eqn. 3.25. K'' is rotated so that $\mathbf{p}'_-$ is along the $-z''$ axis. All lines are in the same plane, since ϕ_{q+} is taken to be 0.

straight forward and the resulting four-momenta are then boosted back into the lab frame.

3.4 Results from the Monte Carlo program

The methods of the previous sections have been incorporated into a Monte Carlo program. This section presents results of third and fourth order calculations of the $e\gamma$, single γ, and single e configurations. Comparisons of the EPA with exact methods are made wherever possible in order to test the validity of the approximation.

3.4.1 $e\gamma$ configuration

For the event configuration where an electron and photon are observed at large angles, the specific acceptance is motivated by the Mark II/PEP detector. The beam energy is $E_b = 14.5$ GeV, the $e\gamma$ acceptance angles are $\cos\theta_{e\,\mathrm{min}} = \cos\theta_{\gamma\,\mathrm{min}} = 0.72$, and the veto angle for the low angle electron is $\theta_{e\,\mathrm{veto}} = 0.1$ rad. The minimum energies of the observed e and γ are $E_{\gamma\,\mathrm{min}} = E_{e\,\mathrm{min}} = 1$ GeV.

For this simple configuration, the equivalent photon spectrum, eqn. 2.15, can be directly integrated over Q^2, to give an analytic formula for the invariant mass

spectrum*. An implicit approximation, however, is made in this calculation, that the boost to the γe center of mass system is along the beam direction. With the choice of 100 mrad for the veto angle, the range of Q^2 is quite wide,

$$8 \times 10^{-9}\ \text{GeV}^2 < Q^2 < 1.8\ \text{GeV}^2\ ,$$

but still much less than $W^2_{\text{min}} \approx 140\ \text{GeV}^2$. Hence the EPA is expected to be valid and the analytic formula indeed agrees well with the event generator using the exact cross section as shown in fig. 3.3.

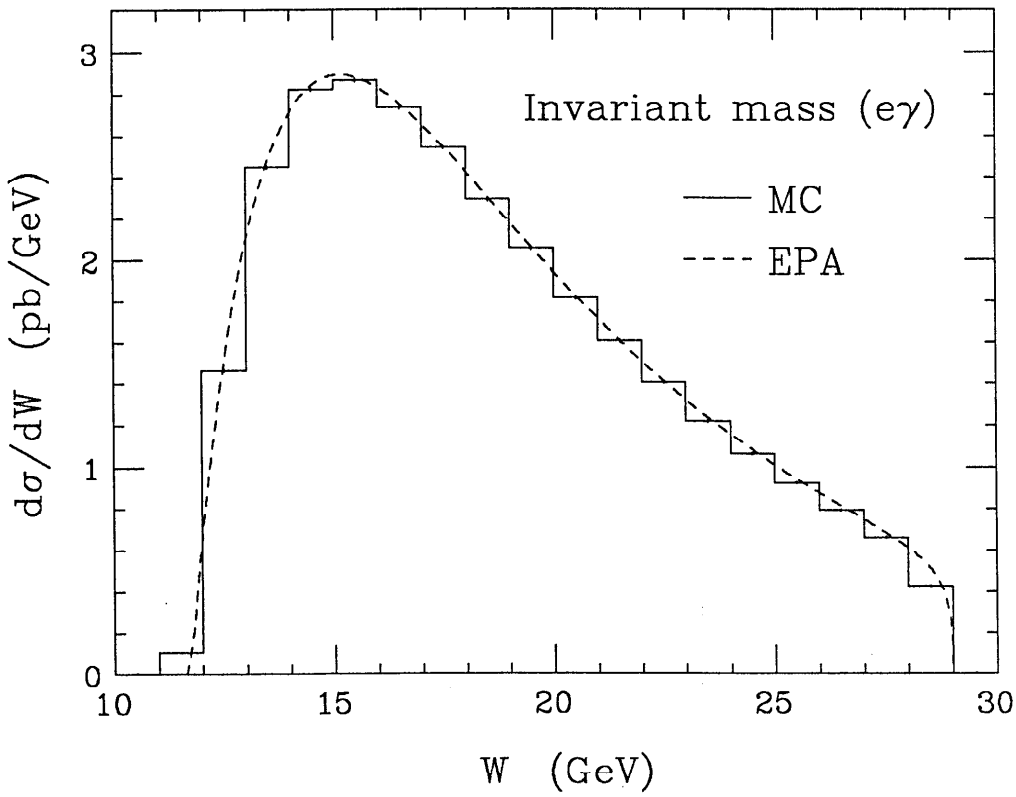

Figure 3.3. $e\gamma$ invariant mass distribution for an acceptance similar to the MarkII/PEP detector. The dashed curve is from an EPA calculation and the histogram is from the Monte Carlo event generator.

* See ref. 15. I replace eqn. (6) by,

$$u_0 = \max\left[\frac{u^\gamma_{\text{min}} - \beta}{1 - \beta u^\gamma_{\text{min}}}, \frac{\beta - u^e_{\text{max}}}{1 - \beta u^e_{\text{max}}}\right] \qquad u_1 = \min\left[\frac{u^\gamma_{\text{max}} - \beta}{1 - \beta u^\gamma_{\text{max}}}, \frac{\beta - u^e_{\text{min}}}{1 - \beta u^e_{\text{min}}}\right]$$

Total third order cross sections for the $e\gamma$ configuration as calculated with various cross section formulae are listed in table 3.1. The same points in phase space were sampled by the Monte Carlo program for each case, so that statistical errors cancel in the comparison. The exact and t channel formulae give the same cross section to within 0.1% which indicates the annihilation channel and the neglected interference terms are indeed small. The EPA cross section also agrees extremely well with the exact result which indicates the approximations used for the calculation of the next order correction are valid for this configuration. When the collinear fermion mass terms are left out, as in the Berends and Kleiss calculation, the total cross section is about 5% larger in this example.

Table 3.1. Lowest order total cross sections for the $e\gamma$ configuration. Exact refers to eqn. 2.10; t channel, eqn. 2.5; EPA, eqn. 2.20; Berends/Kleiss, eqn. 2.2. The same points in phase space were sampled for each calculation.

Calculation	σ (pb)
Exact	29.394 ± 0.023
t channel	29.375 ± 0.023
EPA	29.379 ± 0.023
Berends/Kleiss	30.892 ± 0.023

The total cross section from the analytic integration of the EPA is 29.49 pb in apparent disagreement with the exact result of 29.394 ± 0.023 pb. The discrepancy is not seen in table 3.1, where the EPA formula is integrated using the Monte Carlo program, and hence must be due to the approximation used in the analytic integration. When the veto angle is reduced to 10 mrad to reduce the error in the analytic formula, the integrated EPA result is 20.650 pb and the Monte Carlo result is 20.657 ± 0.016 pb. Such a comparison at the level of 10^{-3} is a sensitive test of the Monte Carlo event generator.

The choice of the cutoff between hard and soft photons, E_{cut}, for the fourth order calculation depends on the detector resolution and analysis criteria. Since this cutoff is specified in the γe center of mass system, it is necessary to first calculate the

maximum boost to the lab system. From eqns. 3.24 and 3.25 the maximum boost is,

$$\gamma_{\max} = \frac{2E_b - q^0_{+\max}}{W_{\min}} = \frac{s + W^2_{\min}}{2\sqrt{s}\, W_{\min}} \,. \tag{3.29}$$

To evaluate this, eqn. 3.22 or some simple approximation can be used. For the example studied here, the minimum invariant mass is about 4 GeV and $\gamma_{\max}$ is less than 4. In this case, $E_{\rm cut}$ does not have to be set much lower than the detector resolution.

An important check of the event generation procedure is that the total cross section and event distributions be independent of the choice of $E_{\rm cut}$. A distribution that separates fourth order events from third order is the total energy of the $e\gamma(\gamma)$ in the detector. The $e\gamma$ in a three body final state is required to have a minimum total energy of about 17 GeV for the Mark II acceptance described above because the $e\gamma$ must balance the longitudinal momentum of the low angle electron. When a second photon is included, this constraint is released, and low energy $e\gamma$ pairs are allowed. The visible energy distribution is shown in fig. 3.4, where the observed e and γ are required to have more than 1 GeV each and be separated by more than 45° in ϕ.

In fig. 3.4a, the contribution from the virtual and soft real photon correction is shown for four choices of $E_{\rm cut}$. When $E_{\rm cut}$ is reduced, the soft contribution decreases as expected. Figure 3.4b shows the corresponding hard photon contribution which has both high and low total energy components. The low total energy part is due to hard photon emission along the beam line, and thus is unaffected by changes in $E_{\rm cut}$, when $E_{\rm cut}$ is sufficiently small. When the soft and hard cross sections are combined, the result is independent of the choice of $E_{\rm cut}$, for $E_{\rm cut} \leq 100$ MeV, as shown in fig. 3.4c. The choice of $E_{\rm cut} = 1$ GeV is seen to be too large, as might be expected since, $W_{\min} \approx 4$ GeV. Larger choices of $E_{\rm cut}$ would further reduce the low visible energy component, which could not be compensated by the three body soft part. Figure 3.4d compares the order α^3 and α^4 distributions, and it is seen that above 17 GeV, the fourth order correction is small and slightly negative, whereas at lower energies, the fourth order contribution is quite large. The size of this contribution is best understood by the fact that if an electron radiates a hard photon in the initial

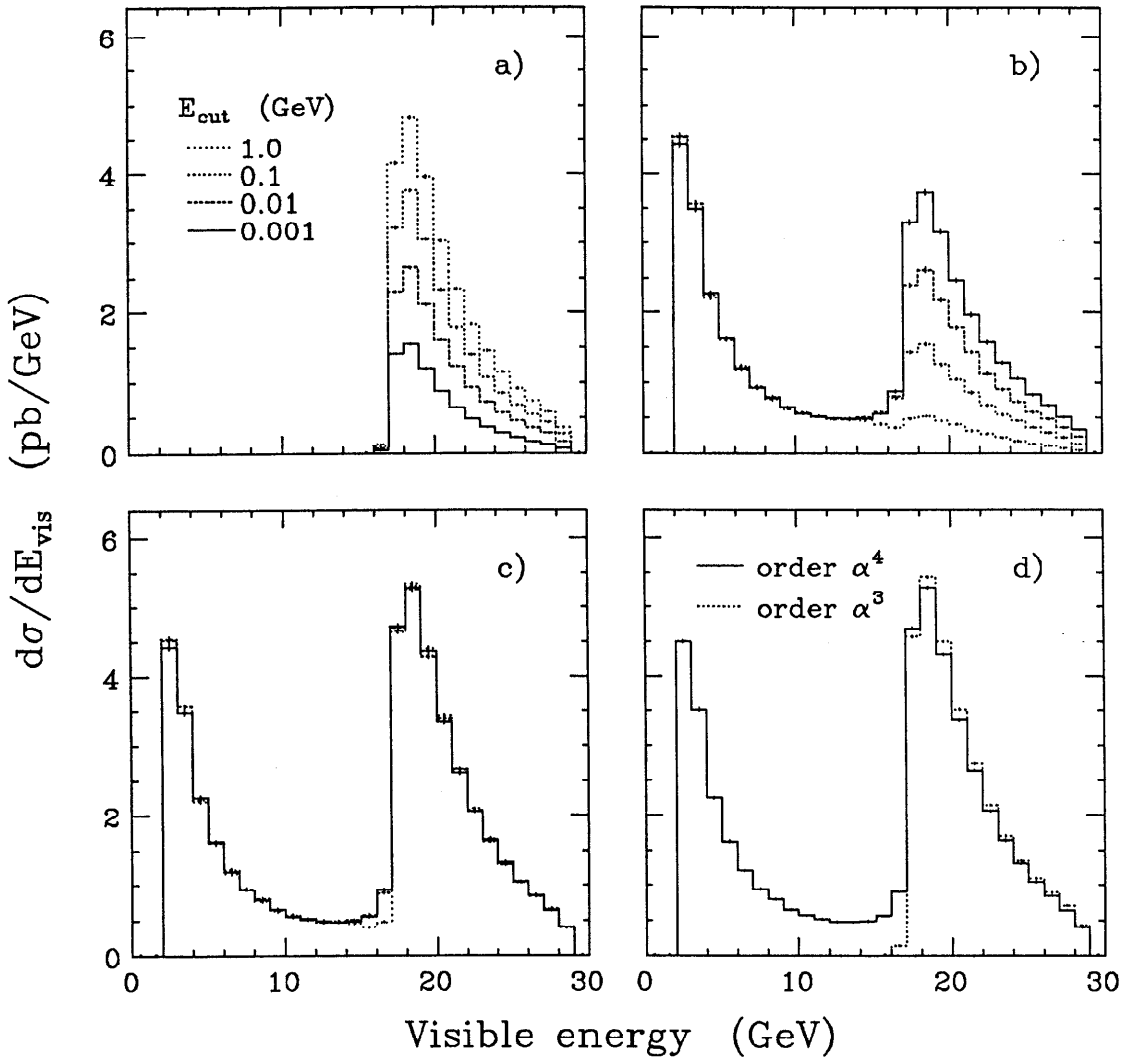

Figure 3.4. Total energy of the $e\gamma(\gamma)$ in the detector. a) virtual and soft real photon correction; b) hard photon contribution; c) total fourth order; d) order α^4 compared to order α^3.

state, the γe scattering process can take place at a much reduced center of mass energy. The process is enhanced in a similar way as two photon processes, as shown in fig. 3.5.

The cross sections for the various choices of $E_{\rm cut} < 100$ MeV agree within a fraction of a percent as shown in table 3.2. When $E_{\rm cut}$ is taken to be 1 GeV, the calculated cross section is about 1% less than the other values, for reasons explained above. In fig. 3.6, the average virtual and soft correction displays the expected logarithmic dependence on $E_{\rm cut}$.

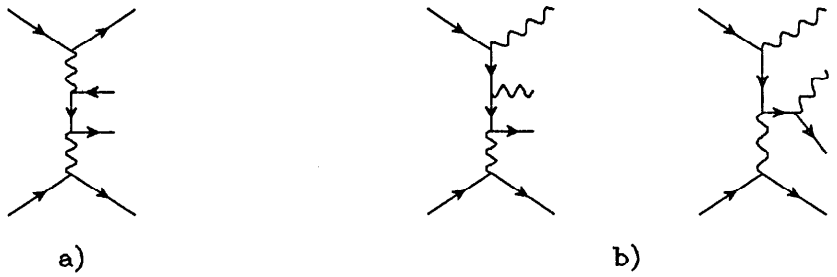

Figure 3.5. Comparison of a two photon diagram with fourth order diagrams that contribute to the low visible energy $e\gamma$ sample. a) Multiperipheral two photon diagram; b) Two $e^+e^- \to e^+e^-\gamma\gamma$ diagrams drawn in similar way to the two photon diagram.

Table 3.2. Order α^4 cross sections for the $e\gamma$ configuration for various cutoff energies.

$E_{\rm cut}$ (GeV)	$\sigma_{\rm soft}$ (pb)	$\sigma_{\rm hard}$ (pb)	$\sigma_{\rm tot}$ (pb)
0.001	7.46 ± 0.01	40.30 ± 0.12	47.76 ± 0.12
0.01	13.51 ± 0.02	34.35 ± 0.10	47.86 ± 0.10
0.1	19.58 ± 0.02	28.21 ± 0.08	47.79 ± 0.09
		average:	$\boxed{47.81 \pm 0.06}$
1.0	25.56 ± 0.03	21.65 ± 0.06	47.21 ± 0.07

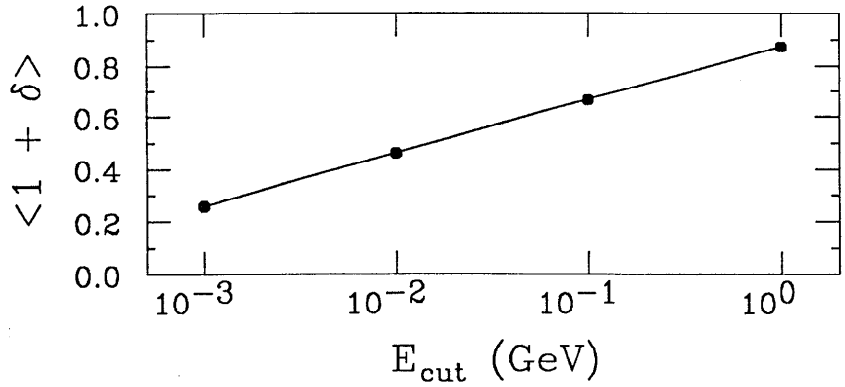

Figure 3.6. The average virtual and soft correction, $\langle 1 + \delta \rangle$, for the $e\gamma$ configuration.

The hard part of the fourth order EPA cross section is compared with other more exact formulae in table 3.3. Again the same points in phase space were sampled for each integration, so that statistical errors do not affect the comparison. The number of points sampled was limited by the evaluation of the Martinez/Miquel matrix element[27]. Their calculation, which includes all t channel diagrams, uses the helicity amplitudes approach[47] and requires three orders of magnitude more computer time than the other methods. The EPA and the Martinez/Miquel results

agree remarkably well, to a fraction of a percent. The Berends *et al.* formula[26], which includes all 40 $e^+e^- \to e^+e^-\gamma\gamma$ diagrams but not the collinear fermion mass terms, predicts a 5% larger cross section, just as in the third order calculation.

Table 3.3. Fourth order hard cross sections for the $e\gamma$ configuration in pb. The same points in phase space were sampled for each calculation. ($E_{\rm cut} = 0.01$ GeV).

Calculation	$\sigma_{\rm hard}$ (pb)
EPA	34.40 ± 0.35
Martinez/Miquel	34.46 ± 0.35
Berends *et al.*	36.15 ± 0.36

No exact calculations of the soft and virtual photon correction to radiative Bhabha scattering exist to compare with the EPA method. However, the independence of the total cross section on the choice of $E_{\rm cut}$, as shown in table 3.2, indicates the integration of the soft photon part is correct.

3.4.2 *Single γ configuration*

The lowest order total cross sections and energy spectra agree with results from a numerical integration of the differential cross section[48,49]* and from another Monte Carlo generator[50] which includes the contribution from the Z^0. As a specific example, I consider an acceptance similar to that of the Mark II detector at SLC, with the beam energy, $E_b = 47$ GeV, the photon acceptance angle, $\theta_{\gamma\,\rm min} = 30°$, and the electron veto angle, $\theta_{e\,\rm veto} = 15$ mrad. Three choices for the minimum energy of the single photon are considered, $E_{\gamma\,\rm min} = 0.5$, 1.0, and 1.5 GeV. For the lower two choices, one electron is kinematically allowed to scatter at 0° and the minimum Q^2 is about 1.4×10^{-13} GeV^2. For $E_{\gamma\,\rm min} = 1.5$ GeV, both electrons must scatter away from 0°, and hence the minimum Q^2 is much larger at 2.2×10^{-3} GeV^2. The maximum Q^2 is about .5 GeV^2, much smaller compared with $W^2_{\rm min} = 6.3$, 13, and 19 GeV^2 for the three choices of $E_{\gamma\,\rm min}$. Hence the EPA is expected to be valid for this configuration. The third order cross sections are listed in table 3.4 as calculated with

* The authors chose to use $\alpha = 1/128.5$, whereas I use $\alpha = 1/137.036$. After correcting for this, agreement is found.

Table 3.4. Lowest order total cross sections for the single γ configuration in pb. The same points in phase space were sampled for each calculation. The equations used for the integrations are listed in the caption of table 3.1.

Calculation	$E_{\gamma\,\mathrm{min}} = 0.5$ GeV	$E_{\gamma\,\mathrm{min}} = 1.0$ GeV	$E_{\gamma\,\mathrm{min}} = 1.5$ GeV
Exact	34.231 ± 0.033	5.049 ± 0.017	0.141 ± 0.004
t channel	33.301 ± 0.032	4.873 ± 0.016	0.119 ± 0.003
EPA	33.334 ± 0.032	4.888 ± 0.016	0.123 ± 0.003
Berends/Kleiss	35.555 ± 0.034	5.232 ± 0.017	0.141 ± 0.004

exact and approximate cross section formulae, using the same points in phase space for each integration.

For the two lower choices of $E_{\gamma\,\mathrm{min}}$ that allow 0° scattering, the t channel calculation predicts a 3% smaller cross section than the exact result. Since this region is still dominated by very low Q^2, the neglected s channel diagrams are not the source of the error. The reason for the discrepancy must be that the interference between the t and t' channels, which is left out of the calculation, is no longer very small. In the case of the $e\gamma$ configuration, the t' channel amplitude is extremely small when the positron scatters at a small angle, since the electron scatters at a large angle. The EPA and t channel results are extremely close, indicating that the additional approximation of evaluating the γe scattering at $Q^2 = 0$ is still accurate. At the level of 3%, the EPA and t channel methods work well for these configurations. When the collinear fermion mass terms are not included, the calculated total cross section is about 4% too large.

For the choice of $E_{\gamma\,\mathrm{min}} = 1.5$ GeV, the t channel result is about 15% too small. In this case, the t and t' channel interference is much more important, since the amplitudes of the two are closer in magnitude when both electrons scatter away from 0°. For this configuration, the approximation used for the fourth order calculation is expected to be less accurate. The collinear fermion mass terms do not significantly affect the cross section, as expected.

To choose an appropriate E_{cut} value for the fourth order generation, the sensitivity of detecting a second photon that could act as a veto must be considered. A

typical detector will not be nearly as sensitive at low angles as at large angles because of solid angle considerations and beam related backgrounds. For the cross sections listed in this section, the detector is considered hermetic above $\theta_{\gamma\,\mathrm{veto}} = 15$ mrad but is unable to detect 1 GeV photons below $\theta_{\gamma\,\mathrm{min}} = 30°$ and 100 MeV photons above $\theta_{\gamma\,\mathrm{min}}$. When $E_{\gamma\,\mathrm{min}} = 0.5$ GeV, the maximum boost is $\gamma_{\mathrm{max}} = 19$. A 1 GeV photon at 15 mrad and a 100 MeV photon at 30° in the detector system correspond to a 30 MeV and 250 MeV photon, respectively, in the γe center of mass system. So a reasonable choice for E_{cut} would be 10 MeV or less.

The total order α^4 cross section for this configuration is constant within about 2% for E_{cut} between 10 KeV and 10 MeV for each choice of $E_{\gamma\,\mathrm{min}}$, as shown in table 3.5. Again the virtual correction behaves logarithmically with the cutoff energy, as shown in fig. 3.7 for the case $E_{\gamma\,\mathrm{min}} = 0.5$ GeV.

The total fourth order cross sections as calculated by the EPA methods are compared with the lowest order results in table 3.6 for the three choices of $E_{\gamma\,\mathrm{min}}$. The correction for the single γ configuration is seen to be very small, unlike the $e\gamma$ configuration.

Figure 3.8 shows that the single photon spectrum does not depend on the choice of E_{cut}, as required, and differs little from the lowest order result. The drop in the cross section for photon energies above 1.4 GeV is due to the fact that both electrons must scatter away from 0° to balance the perpendicular momentum of the observed single photon.

The spectra of extra photons in the detector acceptance are shown in fig. 3.9 for the low angle and central regions and fall as $1/k$ for low photon energies, as expected. The total cross section is not very sensitive to the threshold for vetoing against the second photon. Using the $1/k$ curves, the total cross section for a different choice of $E_{\gamma\,\mathrm{veto}}$ changes by only,

$$\Delta\sigma = 7.0 \times 10^{-2} \ln(\frac{E_{\gamma\,\mathrm{veto}}}{1\ \mathrm{GeV}})\ \mathrm{pb} \quad \text{and} \quad \Delta\sigma = 2.6 \times 10^{-5} \ln(\frac{E_{\gamma\,\mathrm{veto}}}{100\ \mathrm{MeV}})\ \mathrm{pb}$$

for the low angle and central regions, respectively.

Table 3.5. Order α^4 cross sections for the single γ configuration for various cutoff energies.

$E_{\gamma\,\mathrm{min}} = 0.5$ GeV

E_{cut} (MeV)	σ_{soft} (pb)	σ_{hard} (pb)	σ_{tot} (pb)
0.01	12.343 ± 0.014	22.042 ± 0.054	34.385 ± 0.056
0.1	16.955 ± 0.018	17.639 ± 0.044	34.594 ± 0.048
1.	21.520 ± 0.023	13.056 ± 0.033	34.576 ± 0.040
10.	26.174 ± 0.028	8.565 ± 0.025	34.739 ± 0.038

$E_{\gamma\,\mathrm{min}} = 1.0$ GeV

E_{cut} (MeV)	σ_{soft} (pb)	σ_{hard} (pb)	σ_{tot} (pb)
0.01	1.647 ± 0.006	3.132 ± 0.026	4.779 ± 0.027
0.1	2.355 ± 0.009	2.463 ± 0.021	4.818 ± 0.023
1.	3.063 ± 0.011	1.745 ± 0.015	4.808 ± 0.019
10.	3.783 ± 0.014	1.077 ± 0.011	4.860 ± 0.018

$E_{\gamma\,\mathrm{min}} = 1.5$ GeV

E_{cut} (MeV)	σ_{soft} (pb)	σ_{hard} (pb)	σ_{tot} (pb)
0.01	0.046 ± 0.001	0.090 ± 0.006	0.136 ± 0.006
0.1	0.066 ± 0.002	0.068 ± 0.004	0.134 ± 0.004
1.	0.087 ± 0.003	0.045 ± 0.003	0.132 ± 0.004
10.	0.109 ± 0.003	0.030 ± 0.002	0.139 ± 0.004

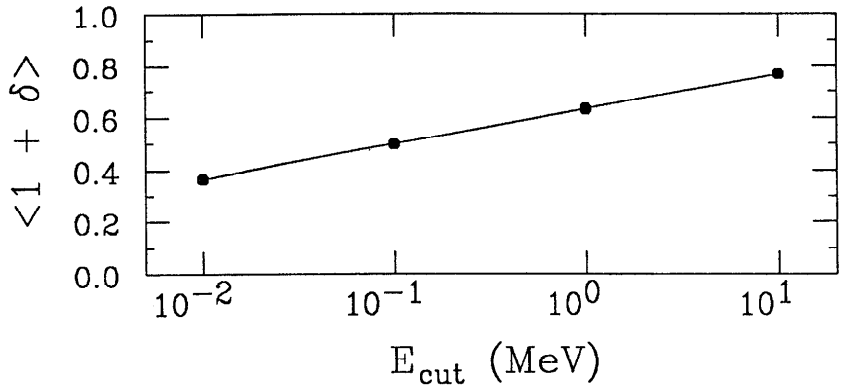

Figure 3.7. The average virtual and soft correction, $\langle 1 + \delta \rangle$, for the single γ configuration.

Table 3.6. Comparison of third and fourth order total cross sections for the single γ configuration. The errors quoted for the order α^4 calculation indicate the 1 σ spread of the values for the various choices of E_{cut}.

	$E_{\gamma\,\text{min}} = 0.5$ GeV	$E_{\gamma\,\text{min}} = 1.0$ GeV	$E_{\gamma\,\text{min}} = 1.5$ GeV
Order α^3	34.231 ± 0.033	5.049 ± 0.017	0.141 ± 0.004
Order α^4	34.574 ± 0.145	4.816 ± 0.034	0.135 ± 0.003

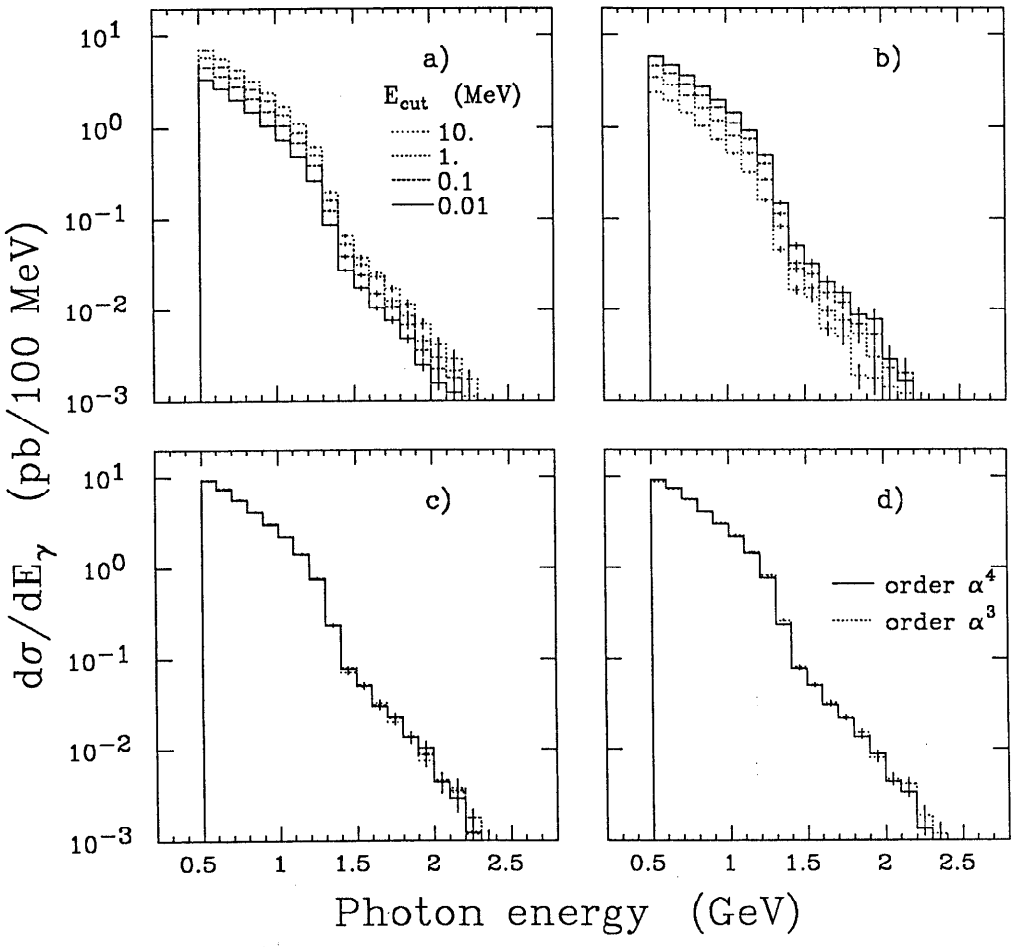

Figure 3.8. Energy of the single γ in the detector. a) virtual and soft real photon correction; b) hard photon contribution; c) total fourth order; d) order α^4 compared to order α^3.

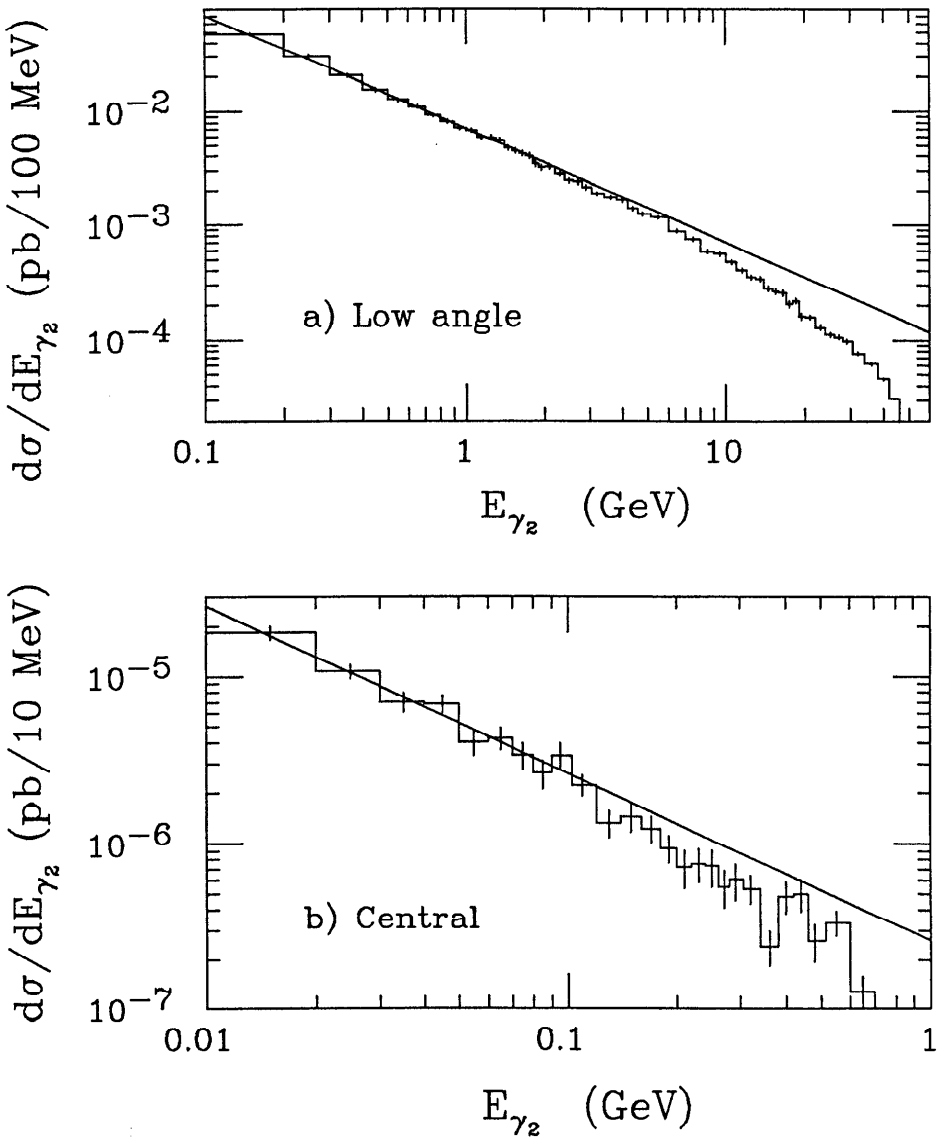

Figure 3.9. Spectrum of second γ in the acceptance. a) Low angle region, 15 mrad $< \theta_\gamma <$ 30°. The curve is $7.0 \times 10^{-2} E_{\gamma_2}^{-1}$ pb/100 MeV. b) Central region, $\theta_\gamma >$ 30°. The curve is $2.6 \times 10^{-5} E_{\gamma_2}^{-1}$ pb/10 MeV.

The hard EPA cross section is compared with the other more exact fourth order formulae in table 3.7. The EPA predicts an 8% lower cross section than the Martinez/Miquel[27] matrix element for the two lowest choices of $E_{\gamma\,\mathrm{min}}$. This is a much greater discrepancy than seen in the lowest order calculation, and is due to certain large Q^2 events with the photons separated by a large angle, such as the event shown in fig. 3.10 a. Diagrams that have an external photon on both the electron and positron lines, such as the one shown in fig. 3.10b, that significantly contribute to

such a configuration, are not included in the EPA calculation. The amplitude is only significant for moderately large Q^2, where the Berends *et al.* formula[26] is also valid. For certain events, at very low Q^2, the Berends *et al.* formula predicts a much larger weight than the other methods, because of neglected collinear fermion mass terms, and so it cannot be reliably used when a large fraction of the total cross section has $t \ll m_e^2$. The Berends *et al.* result is too large and has large errors for $E_{\gamma\,\mathrm{min}} = 0.5$ and 1.0 GeV.

Table 3.7. Fourth order hard cross sections for the single γ configuration. $E_{\mathrm{cut}} = 10$ MeV. The same points in phase space were integrated for each calculation.

Calculation	$E_{\gamma\,\mathrm{min}} = 0.5$ GeV	$E_{\gamma\,\mathrm{min}} = 1.0$ GeV	$E_{\gamma\,\mathrm{min}} = 1.5$ GeV
EPA	8.647 ± 0.174	1.109 ± 0.079	0.032 ± 0.017
Martinez/Miquel	9.304 ± 0.235	1.168 ± 0.084	0.038 ± 0.021
Berends *et al.*	32.47 ± 16.43	1.598 ± 0.173	0.038 ± 0.020

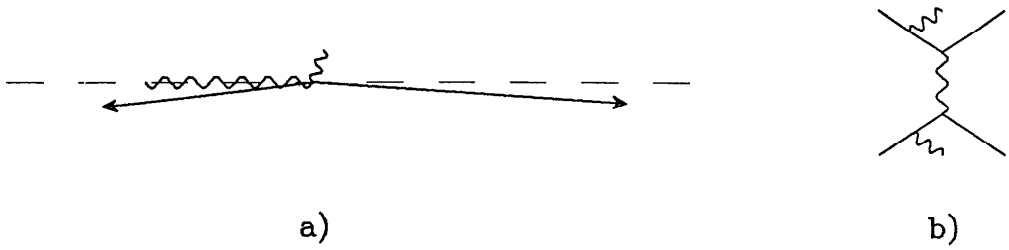

Figure 3.10. An event topology which is underestimated by the EPA method. a) Particle momenta, where the dashed line represents the beam axis; b) A diagram, not included in the EPA method that contributes to the topology.

In a typical study of the radiative correction to a process, only the sensitivity of the experiment to an extra photon needs to be understood, as described above. For the single γ configuration, however, the sensitivity of the detector to low energy electrons must also be considered. In the lowest order, the small angle electrons each have energies near E_b and the detector is presumed to be fully efficient when they are scattered at an angle above $\theta_{e\,\mathrm{veto}}$. When an extra hard photon is present, one of the electrons can be low enough energy that the detector is not able to record it.

In some sense this is not a radiative correction to the process, but rather a distinct process that contributes to the single photon signal.

A study of the effect of allowing low energy electrons in the detector acceptance is made difficult by certain events with large weights. There are poles in the cross section which are not well handled by the Monte Carlo procedure when an electron is nearly collinear with the quasi-real exchanged photon or with the observed photon.

In order to evaluate the contribution from low energy electrons in the detector acceptance, the Monte Carlo program was run in the $e\gamma$ configuration with $E_{e\,\mathrm{min}} = m_e, \theta_{e\,\mathrm{min}} = 15$ mrad, $E_{\gamma\,\mathrm{min}} = 0.5$ GeV, $\theta_{\gamma\,\mathrm{min}} = 30°, \theta_{e\,\mathrm{veto}} = 15$ mrad. The veto threshold against extra photons is taken as before where in the low angle region, $\theta < 30°$, the minimum energy required to veto the event is 1 GeV, while in the central region, $\theta > 30°$, the minimum is 100 MeV. The electron energy spectrum in the low angle acceptance is shown in fig. 3.11 for single photon events with $E_{\gamma\,\mathrm{min}} = 0.5$ GeV, with no extra photon above the veto threshold. The order α^3 process has $E_e > 25$ GeV, far above a typical veto threshold. As with the configuration studied in section 3.4.1, there is a large fourth order cross section at low visible energy. For electron energies between about 2 and 10 GeV, the spectrum follows a power law, falling slightly faster than $1/E_e$, and the sensitivity to the veto threshold of electrons is moderate, at

$$\Delta\sigma \approx 64 \text{ pb } \left(E_1^{-.25} - E_2^{-.25}\right)$$

where the energies are expressed in GeV. For $E_e < 1$ GeV, the presence of the electron has less effect in balancing the single photon $p_\perp$ but occasionally large weights occur as mentioned above. There is a similar large contribution for low energy electrons in the central region. Using the same veto threshold for the electrons as for the photons, the additional contribution to the single photon cross section is large, as shown in table 3.8.

The single photon generation is far more problematical than the $e\gamma$ generation because of low energy electron final states. A modification to the Monte Carlo method is required to evaluate the total correction more precisely.

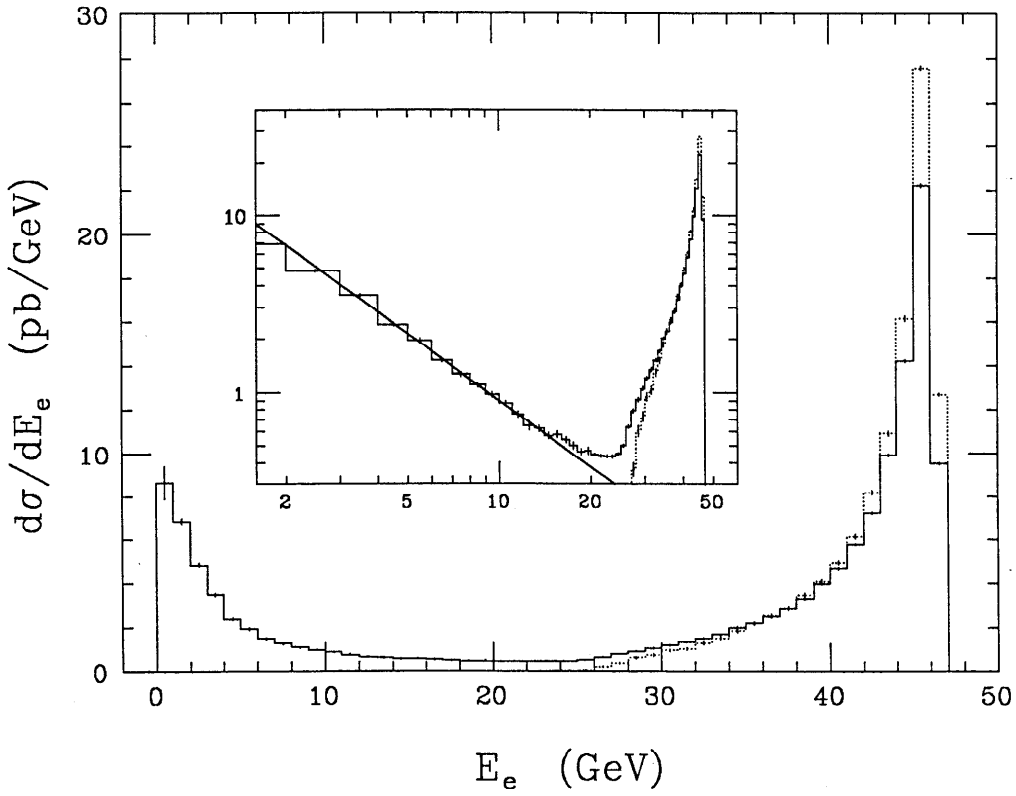

Figure 3.11. Electron spectrum in the low angle acceptance. The dashed histogram is the order α^3 prediction and the solid histogram is order α^4. The log-log inlay shows that spectrum roughly follows the power law, $\frac{d\sigma}{dE_e} = 16\left(\frac{E_e}{GeV}\right)^{-1.25}$ pb/GeV, for 2 GeV< E_e <10 GeV. A large difference between the third and fourth order predicition for electron energies above 40 GeV is due to the unphysical photon veto.

Table 3.8. Cross sections from low energy electrons in the detector acceptance but below the veto threshold (1 GeV for $\theta < 30°$, 100 MeV for $\theta > 30°$) for the single photon configuration, compared to the fourth order cross sections.

	$E_{\gamma\,\mathrm{min}} = 0.5$ GeV	$E_{\gamma\,\mathrm{min}} = 1.0$ GeV	$E_{\gamma\,\mathrm{min}} = 1.5$ GeV
Order α^4	34.574 ± 0.145	4.816 ± 0.034	0.135 ± 0.003
Low E_e	14.3 ± 0.8	0.794 ± 0.061	0.023 ± 0.005

3.4.3 Single e configuration

For this configuration where only one electron is scattered at a large angle, I choose an acceptance similar to that of the ASP/PEP detector[51]. The beam energy is $E_b = 14.5$ GeV and the electron acceptance is $\theta_{e\,\mathrm{min}} = 30°$ and $E_{e\,\mathrm{min}} = 0.5$ GeV. and the ASP detector is hermetic down to $\theta_{e\,\mathrm{veto}} = \theta_{\gamma\,\mathrm{veto}} = 21$ mrad. The EPA should be valid for this configuration, since the maximum Q^2 is about 0.1 GeV^2 whereas W^2_{min} is about 1.9 GeV. In table 3.9, the lowest order cross section formulae are compared for this configuration. The t channel and EPA results are about 0.5% larger than the exact total cross section. This is unlike the two other configurations, where these approximations predicted slightly lower cross sections than the exact formula. When collinear fermion mass terms are not included, the calculated total cross section is less than 2% larger.

Table 3.9. Lowest order total cross sections for the single e configuration. The same points in phase space were sampled for each calculation.

Calculation	σ (pb)
Exact	513.8 ± 2.3
t channel	515.9 ± 2.3
EPA	515.6 ± 2.3
Berends/Kleiss	522.6 ± 2.3

For the single e configuration, the low angle electron can balance the $p_\perp$ of the observed electron while the photon is scattered at a very small angle. Consequently, event topologies with large Q^2 are more prevalent than in the other configurations. This explains the smaller effect of the collinear fermion mass terms.

The same photon energy threshold for vetoing an event is taken as in the single photon generation. However, a photon in the central region must also be more than 30° in ϕ away from the electron in order to veto the event. For E_{cut} between 10 KeV and 10 MeV, the total fourth order total cross section is stable to within 1% as shown in table 3.10, and is about 6% lower than the lowest order result. The energy and $p_\perp$ distributions of the observed electron are relatively unchanged from the order α^3 calculation. The average soft correction increases logarithmically with the cutoff

Table 3.10. Order α^4 cross sections for the single e configuration for various cutoff energies.

$E_{\rm cut}$ (MeV)	$\sigma_{\rm soft}$ (pb)	$\sigma_{\rm hard}$ (pb)	$\sigma_{\rm tot}$ (pb)
0.01	143.4 ± 0.7	344.1 ± 3.9	487.5 ± 3.9
0.1	227.8 ± 1.0	257.1 ± 3.5	484.8 ± 3.7
1.0	311.1 ± 1.4	171.6 ± 2.3	482.7 ± 2.7
10.	392.9 ± 1.8	87.4 ± 1.5	480.3 ± 2.3
		average:	$\boxed{482.7 \pm 1.5}$

energy as in the other configurations.

The various calculations of the 4 body final state are compared for the single e configuration as shown in table 3.11. The EPA again agrees very well with the Martinez/Miquel calculation, whereas the Berends *et al.* result is much larger.

Table 3.11. Fourth order hard cross sections for the single e configuration. The same points in phase space were sampled for each calculation. ($E_{\rm cut} = 10.$ MeV).

Calculation	$\sigma_{\rm hard}$ (pb)
EPA	88.51 ± 4.27
Martinez/Miquel	88.11 ± 4.10
Berends *et al.*	103.86 ± 7.19

The spectra from low energy photons in the detector acceptance are shown in fig. 3.12, for both the low angle and central regions. The distribution is much more complicated than in the single γ configuration, fig. 3.9, where a simple $1/k$ dependance is seen. The difference can be understood by the fact that the topology of an electron and photon balancing $p_\perp$ is enhanced by diagrams such as those shown in fig. 3.5b. The topology of two photons balancing $p_\perp$, however, is not enhanced by any pole in the cross section.

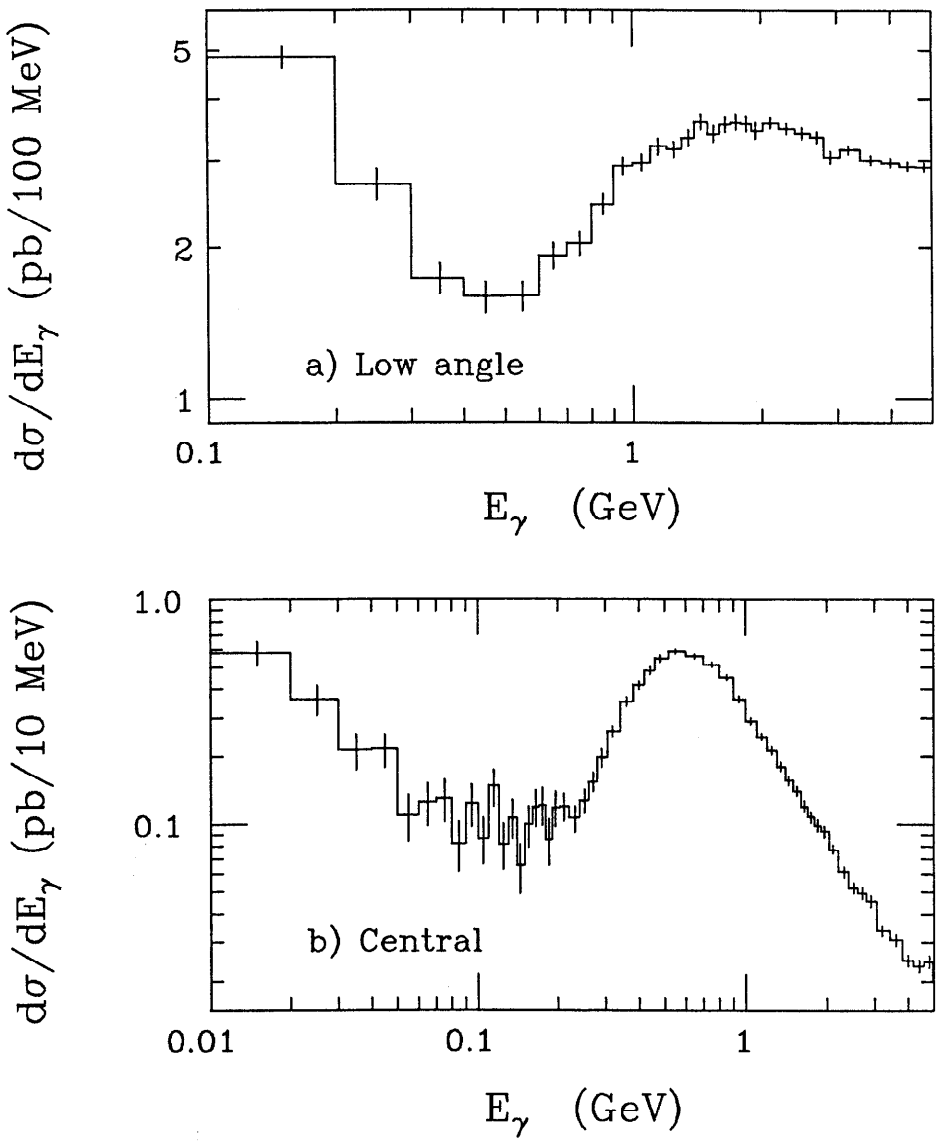

Figure 3.12. Photon spectrum in the detector acceptance for the single e configuration. a) Low angle region, 21 mrad $< \theta_\gamma <$ 30°. b) Central region, $\theta_\gamma >$ 30° and seperated by 30° in ϕ.

4

The Mark II detector at PEP

The Mark II detector, shown in fig. 4.1, is a general purpose device for studying physics at e^+e^- colliding beams. Initially designed for use at the SPEAR storage ring, it began operation there in 1978, where beams were delivered with a center of mass energy between 3 and 7.5 GeV. During the years 1980 through 1985, the detector was stationed at the PEP storage ring, which primarily ran at 29 GeV. Currently, the detector is at the interaction region of the SLC for measurements near the Z^0 resonance. Throughout its history the detector has evolved with improvements made to most of its components.

This chapter briefly describes the elements of the Mark II detector as they existed during the years 1981 through 1984 when data was taken at the PEP storage ring. Detailed descriptions of the detector are found in refs. 52 and 53. An excellent review of the principles of particle detectors can be found in ref. 54. In the following, emphasis is placed on the performance of the detector elements that are used in the analysis of low Q^2 radiative Bhabha scattering, as measured with data from other QED processes. The accuracy of the detector simulation program is also evaluated.

4.1 Vertex and main drift chambers

Charged particle detection is provided by the two central drift chambers. The chambers consist of a large number of drift cells, each containing a single sense wire. As a charged particle passes through a cell, it ionizes molecules of the gas in the cell

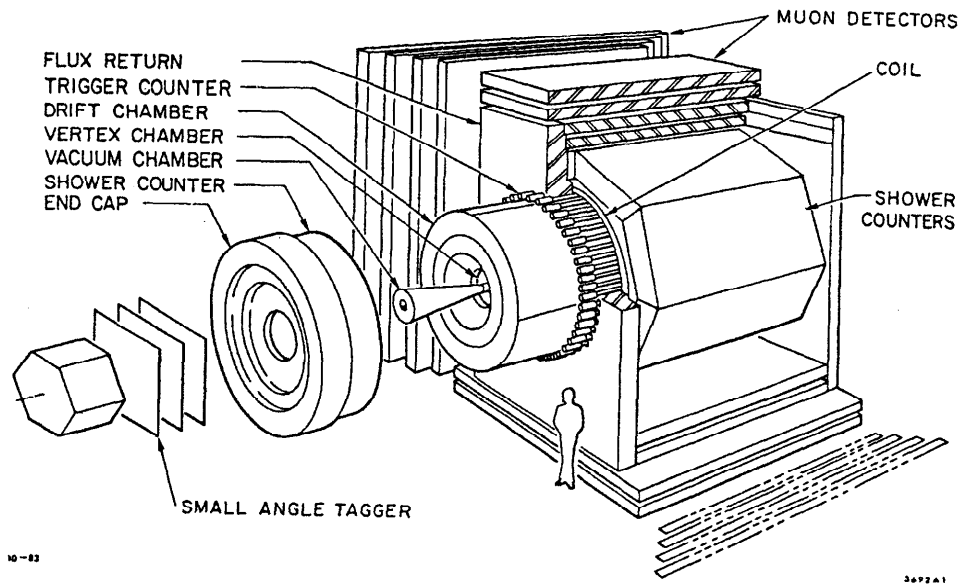

a)

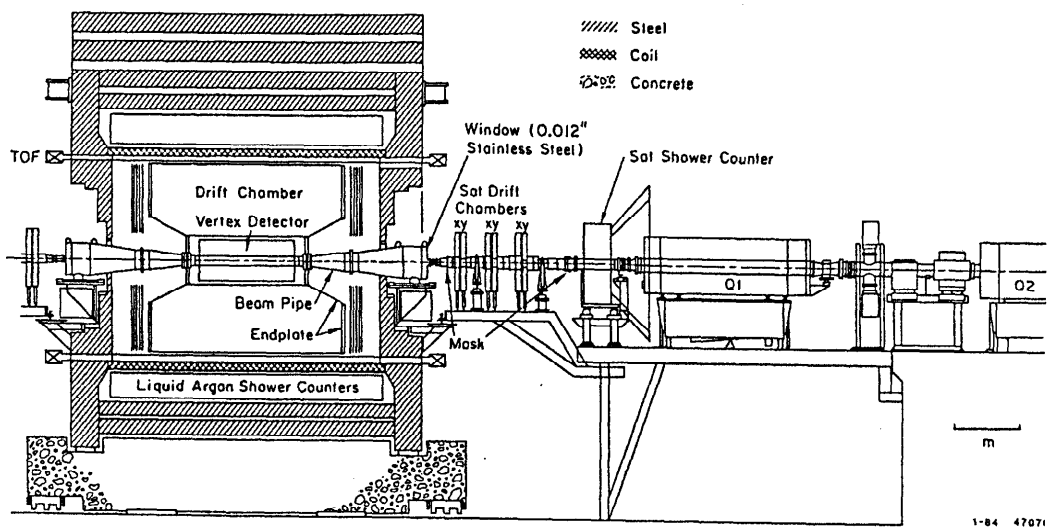

b)

Figure 4.1. The Mark II detector at PEP; a) exploded view; b) side view.

and the freed electrons drift towards the sense wire (since it is at a high potential) and cause an avalanche of more free electrons. The time of arrival of the charge pulse at the sense wire is recorded, providing a measurement of the distance of closest approach of the initial charged particle to the sense wire. If the particle traverses many cells, the path that it follows, commonly known as a track, can be reconstructed.

The innermost element of the Mark II detector, the vertex chamber[55], is a high precision cylindrical drift chamber which surrounds the beam pipe, as shown in fig. 4.2. This chamber consists of four inner layers of drift cells with a mean radius of 11 cm from the beam pipe center, and three outer layers at a mean radius of 31 cm. There are a total of 270 cells in the inner layers and 555 in the outer. All of the cells are oriented parallel to the axis of the detector, and hence measure only the projection of tracks perpendicular to the beam direction.

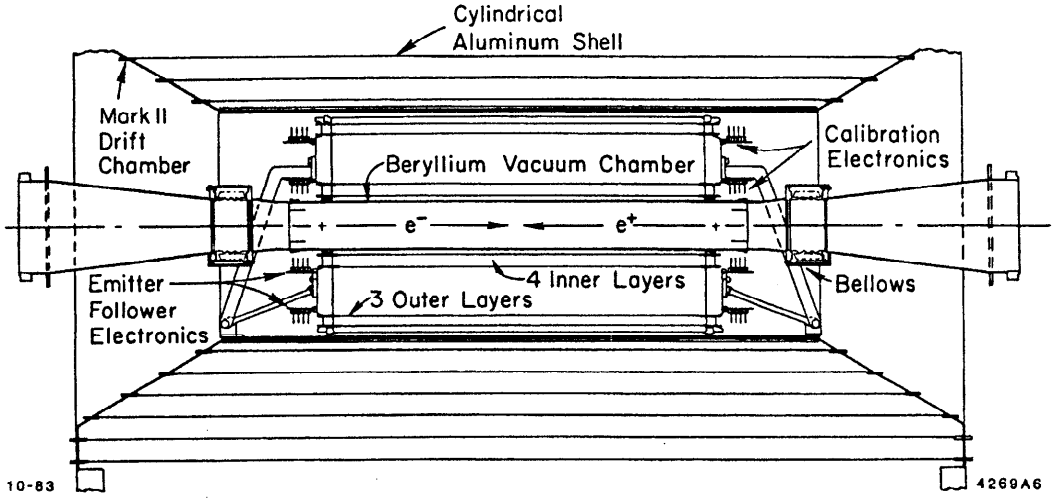

Figure 4.2. The Mark II vertex drift chamber. Shown are the relative positions of the inner and outer layers of drift cells. A few layers of the main drift chamber are also shown.

Surrounding the vertex chamber is the main drift chamber[56], which consists of 16 evenly separated layers of drift cells from 41 cm to 145 cm in radius from the center; a total of 3204 cells. Ten of the layers have the sense wires at an angle of $\pm 3°$ with respect to the axis of the detector, allowing a measurement of the polar angle of the tracks. The length of the chamber is 2.7 m, so that particles with polar angles between 47° and 133° traverse all 16 layers of the main chamber (and all 7 layers of

the vertex chamber).

The two drift chambers are surrounded by a solenoid that provides a 2.3 kG magnetic field along the axis of the detector. A charged particle traversing this field follows a helix with radius of curvature inversely proportional to the charge of the particle and proportional to the momentum transverse to the axis of the detector,

$$r \text{ (m)} = 15 p_{\perp} \text{ (GeV/c)} \; / \; Q \text{ (e)} \; .$$

Hence, electrons can be distinguished from positrons and their momentum vectors can be determined by reconstructing their paths through the chambers.

To simulate the performance of the chambers and the effect of the material on particles that traverse them, a Monte Carlo procedure is used. A particle is taken through each medium (the beam pipe, for example) and may undergo scattering, bremsstrahlung, or conversion (in the case of photons) at any stage according to probabilities which are functions of the momentum of the particle and amount of material it traverses. Timing information is generated for cells which the particle crosses, using the distance to the sense wire, and is smeared to simulate the spatial resolution of the cells. These times are recorded in the same form as real data so that the same reconstruction and analysis programs can be used for both real and Monte Carlo data sets. In the following, real data is compared to simulated data to ensure that the performance of the chambers is well understood.

The resolution of the drift chambers is studied with the large sample of Bhabha events and radiative Bhabha events where both electrons scatter into the drift chamber volumes. For the simple two body final state, the electrons have the beam energy and are back to back. Radiative effects, however, smear the energies and the acollinearity of the electrons, and thus must be taken into account when studying the resolutions. A measurement of Bhabha scattering, that determines the integrated luminosity, is discussed in detail in chapter 5. The distributions shown below come from that analysis.

In fig. 4.3, the measured momentum distribution of electrons from Bhabha events

is compared to a Monte Carlo data set with and without detector simulation. The real data set is divided into 'good' and 'poor'; the 'poor' referring to 40% of the data which was taken when the main drift chamber was operated at a lower voltage to reduce the dark current. Satisfactory agreement is seen for the 'good' data set whereas the 'poor' data set has worse resolution. The mean momentum for electrons is 1.5 GeV lower than for positrons, and is not modeled by the detector simulation. The analyses in this thesis, however, do not depend sensitively on the momentum resolution.

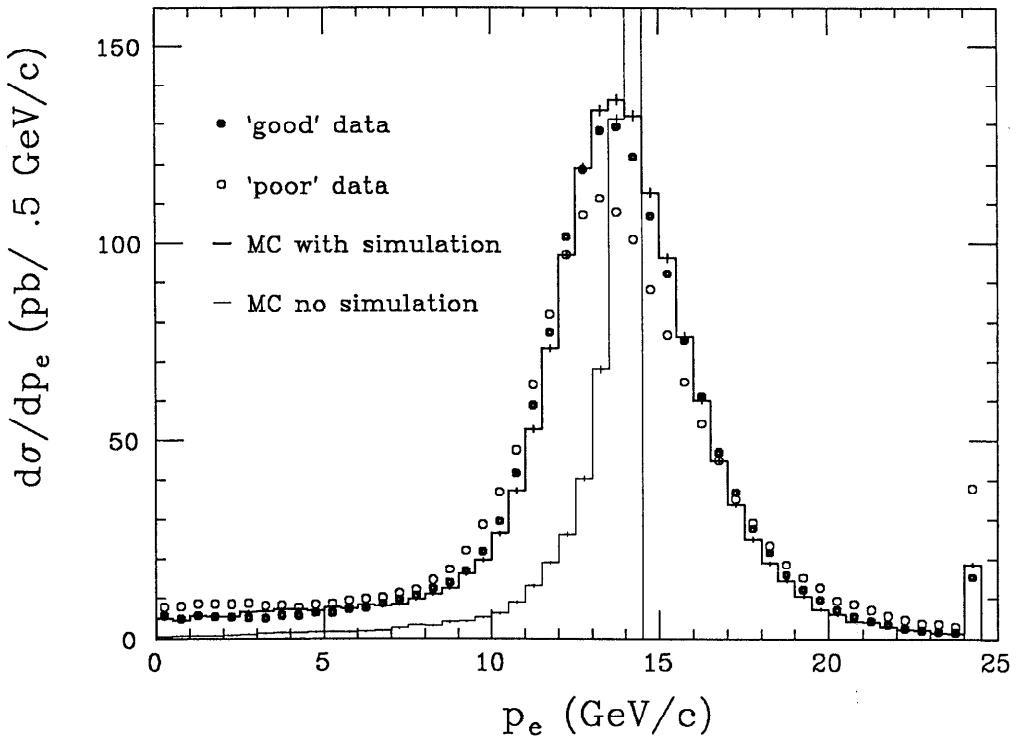

Figure 4.3. Momentum distribution of electrons from Bhabha scattering as measured by the drift chambers. The good and poor data sets are shown by the closed and open circles. The Monte Carlo distribution with and without detector simulation is also shown. The highest momentum bin contains all momenta greater than 24 GeV/c.

The two electrons in a Bhabha event are reconstructed independently, which allows the angular resolutions to be measured. The difference in the azimuthal angles of the two tracks in Bhabha events is shown in fig. 4.4. The Monte Carlo simulation agrees fairly well with the 'good' data set, including a charge asymmetry due to a

reconstruction bias. The azimuthal resolution in the Monte Carlo simulation is found to be 0.5 mrad by comparing the 'true' and 'measured' angles. The sum of the polar angles is shown in fig. 4.5, and the resolution predicted from the detector simulation falls between the 'good' and 'poor' data set resolutions. The distributions are much broader than for the azimuthal angle because of initial state radiation. The unusual shape of the raw distribution near ±10 mrad is due to details of the Monte Carlo event generation in that the events either have no photon, or have a photon with energy greater than 1% of the beam energy. The resolution found with the Monte Carlo residual distribution, is 4.5 mrad. The measurement of the polar angle is much less accurate than for the azimuthal angle, since only the stereo layers in the main drift chamber provide this information.

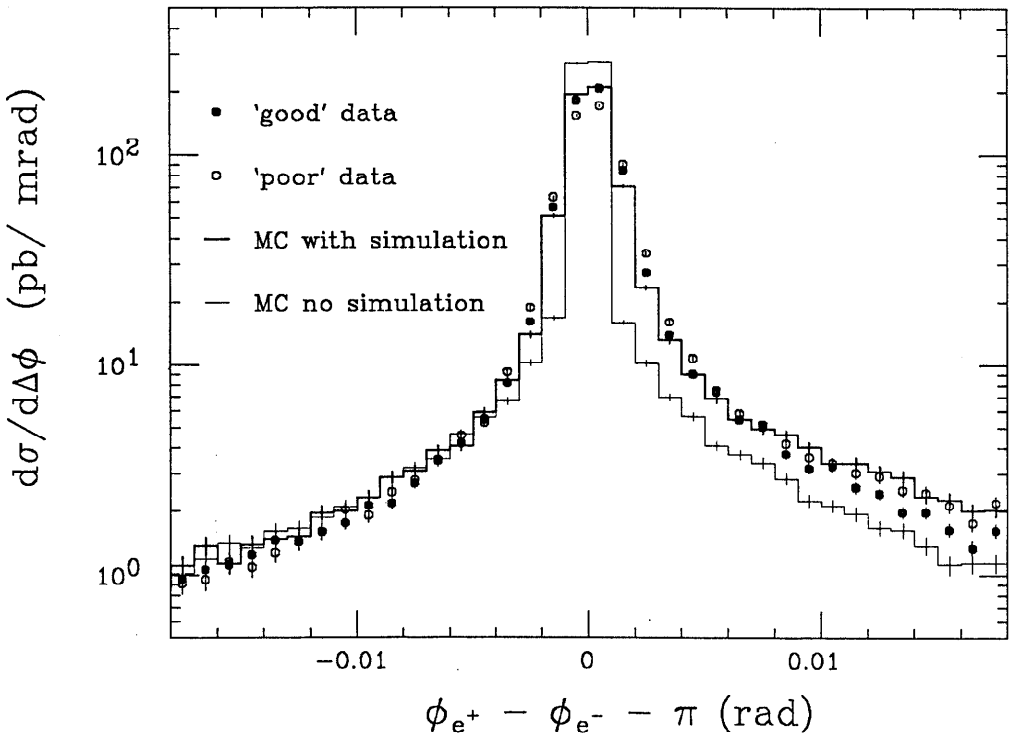

Figure 4.4. Difference of the azimuthal angles of electrons from Bhabha scattering as measured by the drift chambers. The good and poor data sets are shown by the closed and open circles. The Monte Carlo distribution with and without detector simulation is also shown.

The reconstruction efficiency for Bhabha electrons is very high at 99.86% per

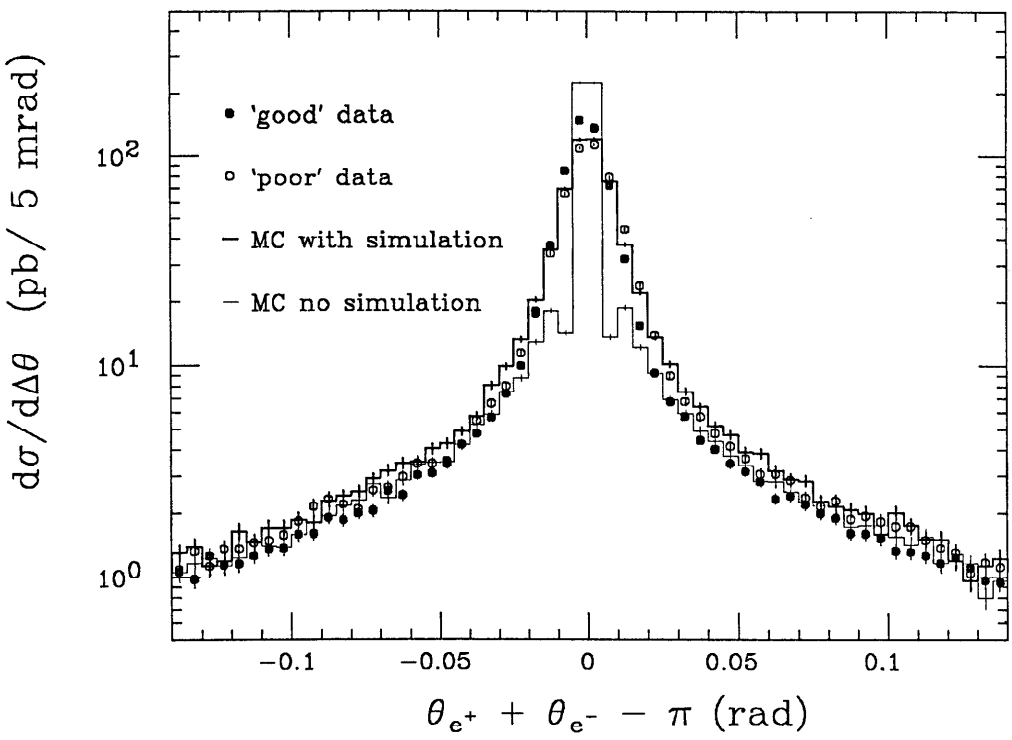

Figure 4.5. Sum of the polar angles of electrons from Bhabha scattering as measured by the drift chambers. The good and poor data sets are shown by the closed and open circles. The Monte Carlo distribution with and without detector simulation is also shown.

track, and agrees with the Monte Carlo expectation of 99.88%. Occasionally the charge of an electron is misidentified because of resolution and scattering effects. The Monte Carlo predicts this to happen for 2.8% of the events whereas for the 'good' and 'poor' data this occurs 1.0% and 3.8%, respectively.

4.2 Time of flight counters

Surrounding the main drift chamber and inside the solenoid magnet is a layer of 48 plastic scintillators, each 20 cm wide and spanning the length of the drift chamber. A charged particle, as it passes through the 2.5 cm thick counter, excites molecules in the plastic which emit visible light. The light travels along the length of the scintillator by internal reflection and is collected at both ends by photomultiplier tubes.

The purpose of this system is to precisely measure the flight times for charged particles to reach the cylindrical radius of 1.5 m. The mass of low momentum particles can be determined using this information. The time of flight counters are used in the

Bhabha analysis to reject cosmic ray backgrounds, and are an important part of the charged particle trigger, as discussed in section 4.7 below. The difference of measured and expected flight times for electrons from the Bhabha analysis is shown in fig. 4.6. A Gaussian fit to the central part of this distribution indicates a resolution of about 370 ps.

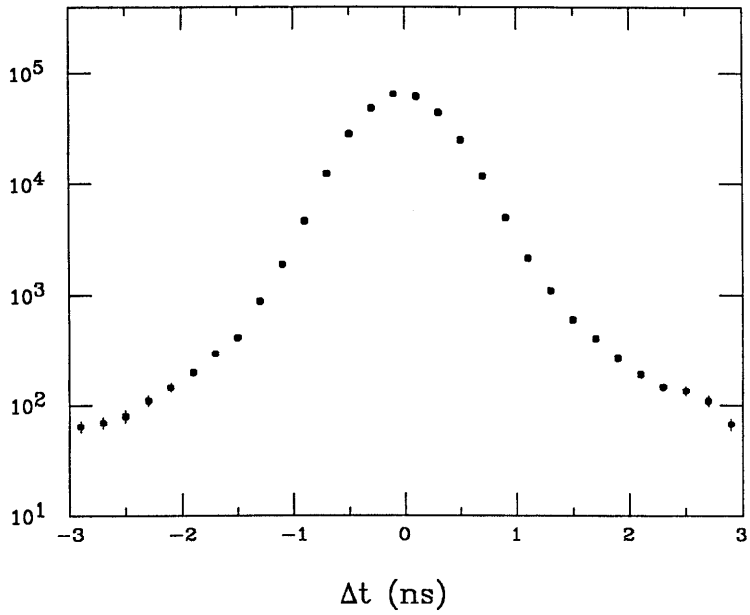

Figure 4.6. The difference between measured and expected flight times for Bhabha electrons.

4.3 Liquid Argon calorimeters

Eight liquid argon modules, surrounding the solenoid magnet as shown in fig. 4.1, provide electromagnetic calorimetry[57]. Each module is a sandwich constructed primarily of lead strips and liquid argon. The lead strips have two functions. Firstly lead is a dense material in which incident high energy photons convert to electron-positron pairs and electrons (and positrons) undergo bremsstrahlung, producing more high energy photons. These two processes of bremsstrahlung and conversion continue to feed each other so that a shower of lower energy photons, electrons, and positrons develops. As the energies of the particles decrease, collision processes dominate, which ionize the detector material.

The second function of the lead is to provide a means of measuring the charge

from the ionization of the argon. Alternate layers of lead are held at ground and 3.5 kV across the 3 mm liquid argon filled gaps, to provide a drift field for the freed electrons. The layers of lead at high potential are segmented into strips along the length, width or diagonal directions (see fig. 4.7) so that the position of the shower can be determined.

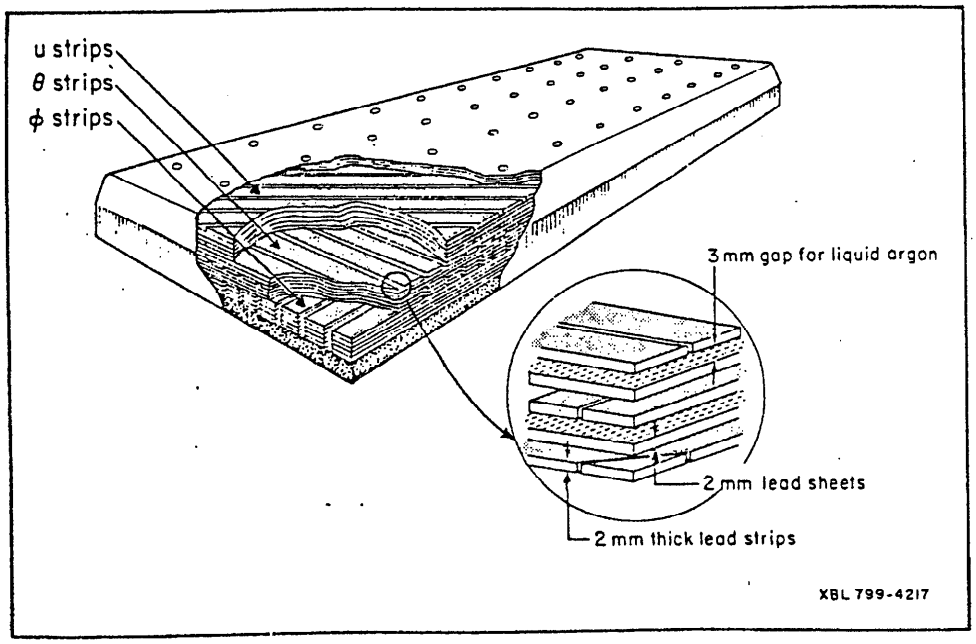

Figure 4.7. Cutaway view of a liquid argon calorimeter module. The insert shows the liquid argon gap and the segmentation of the lead strips. The strips along the length and width of the module are 3.5 cm wide and along the diagonal are 5 cm wide.

The first two layers in each module, known as the trigger gap, are made of aluminum instead of lead, providing a tag for showers that start in the magnet coil. Altogether, there are 37 layers of lead, 18 of which are read out and ganged into six measurements, as shown in fig. 4.8. The complete module is a total of 14.4 radiation lengths thick at normal incidence.

The liquid argon modules are simulated by the electromagnetic shower program, EGS[58]. This program simulates shower development, described above, using a Monte Carlo approach. For high energy showers, the program takes a significant amount of computing time, roughly 0.5 sec per GeV of electromagnetic energy. To generate the number of Monte Carlo Bhabha events equal to the data set sample

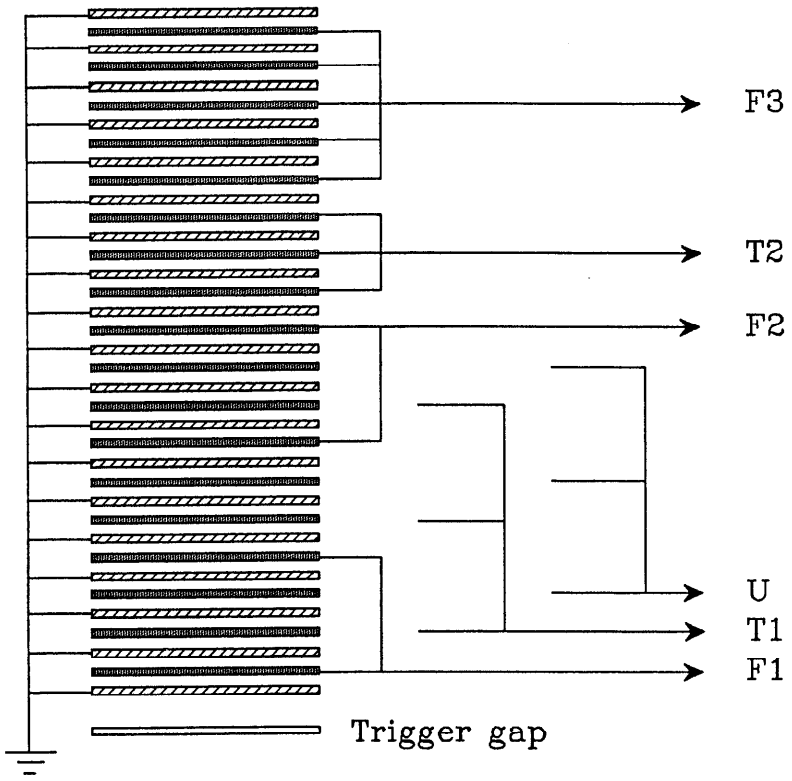

Figure 4.8. Liquid argon calorimeter ganging scheme. Particles enter from the bottom and the ionization is measured along the azimuthal (F), polar (T), and diagonal (U) directions. Measurements are summed in hardware to reduce the total number of channels.

would take over 600 hours of mainframe computing time. Instead, a library of EGS generated showers for various energies and angles of incidence was created which required only 8 hours. The closest energy and angle bin that matches the incident particle is found and a shower from that bin is selected at random. The shower is then overlaid at the position of the entering particle, and the signals are associated with the appropriate strips.

The active region of the liquid argon calorimeter determines the solid angle over which the analyses of this thesis are made. The efficiency for a liquid argon track to be reconstructed with energy greater than 10 GeV for Bhabha events is shown near the edges of the calorimeter in fig. 4.9. The fiducial volume of the liquid argon system is taken to be well inside the physical volume, eliminating any edge effects. Inside this volume, the reconstruction inefficiency for Bhabha electron showers is only 0.02%.

The energy distribution for Bhabha events with acollinearity less than 10 mrad

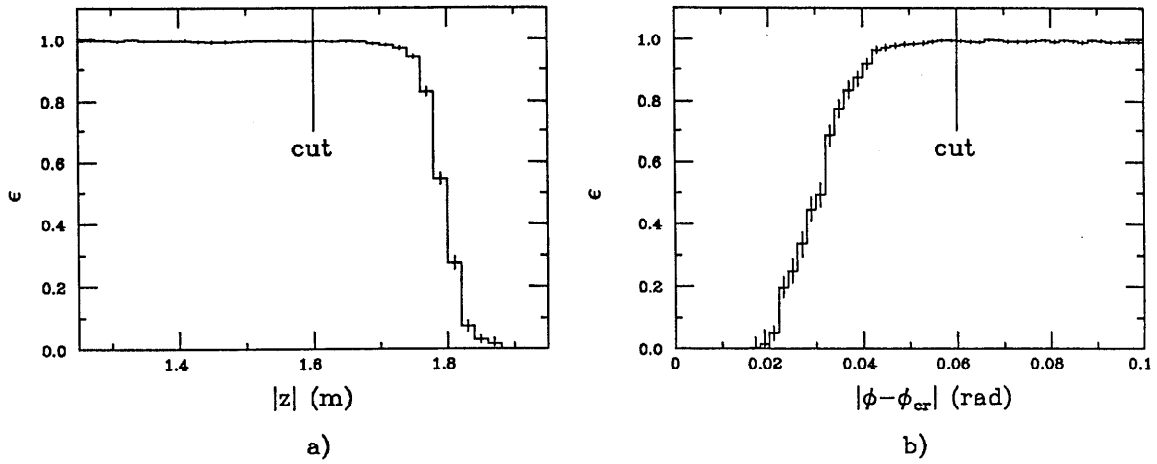

Figure 4.9. Efficiency of the liquid argon calorimeter system to reconstruct a track with energy greater than 10 GeV for Bhabha electrons; a) near the edges along the z coordinate; b) near the edges between modules. The cut lines define the fiducial volume used in this analysis.

and inside the fiducial volume is shown in fig. 4.10, and compared to the EGS simulation. The poor agreement is due to parts of the detector geometry left out of the simulation[59]. Plastic spacers that separate the lead, make up about 4% of the area and along with a few non-active lead strips, are the largest factors. The 5% antimony content of the lead is also not included in the simulation but this does not greatly affect the energy resolution.

In order to improve the simulation of the calorimeter for the analysis of low Q^2 radiative Bhabha scattering, additional smearing of the energy is added to the Monte Carlo events. The Bhabha data set was used to decide on the smearing parameters with the help of the MINUIT program[60]. About 90% of the showers are smeared with an offset exponential, with a 'decay constant' of about 5% of the pre-smeared energy, to match the low energy tail. The remaining 10% are smeared with a Gaussian distribution, with a width of 5% of the energy, to better match the high energy end. The Monte Carlo energy distribution after applying this smearing is shown in fig. 4.11.

The resolution for lower energy photons is studied with radiative Bhabha scattering events where both electrons and the photon are in the liquid argon acceptance. Using the angular measurements, the energies of the three particles can be determined and compared to the measured quantities. The residual distribution for various en-

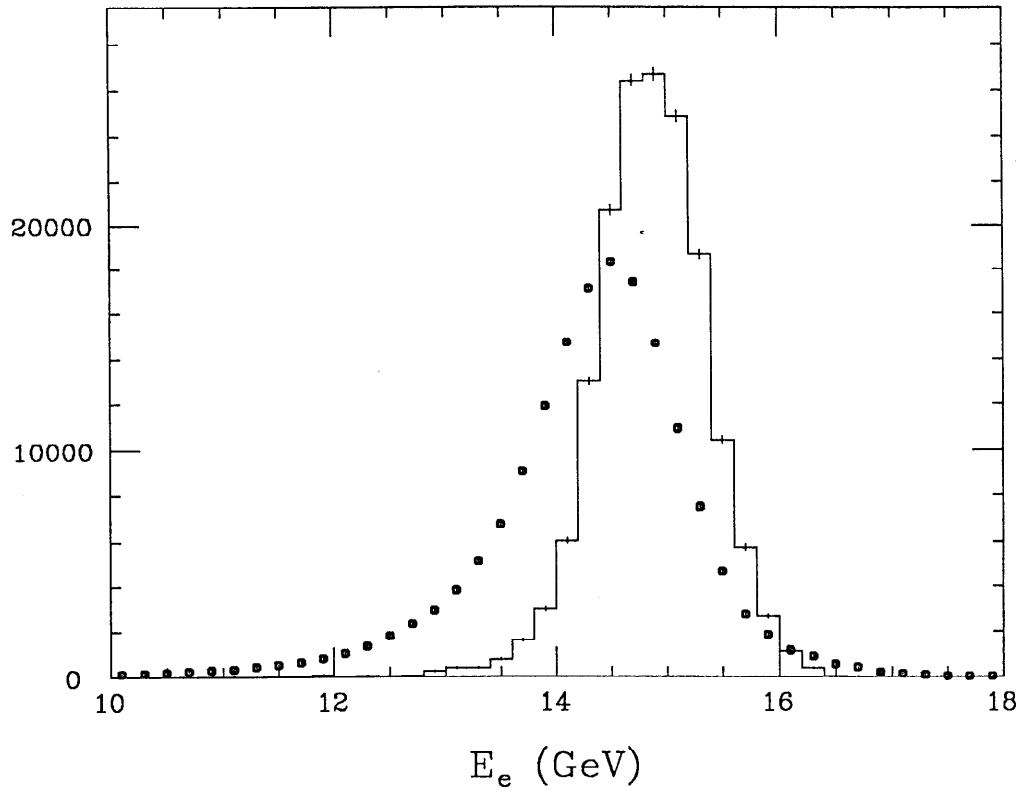

Figure 4.10. Liquid argon energy distribution for Bhabha events, with acollinearity less than 10 mrad. The data is shown by the points. The simulation by EGS, without allowing for inactive regions is given by the histogram.

ergy photons is shown in fig. 4.12, and is matched well by the Monte Carlo simulation with the same smearing as for Bhabha scattering.

The angular resolution of the calorimeter is studied by comparing the measured position of calorimeter showers with the drift chamber tracks projected to the nominal trigger gap* for Bhabha events. The agreement between data and detector simulation is very good for the coordinate along the length of the modules, z, and satisfactory for the azimuthal measurement, as seen in fig. 4.13. The Monte Carlo residuals indicate that the calorimeter position resolution in z is 0.6 cm and in ϕ is 2.6 mrad for high energy photons.

Occasionally, noise in the liquid argon calorimeter is interpreted as real photons. The probability of finding fake photons is determined from small angle Bhabha scat-

* the plane parallel to a calorimeter module at the radius of 1.8 m

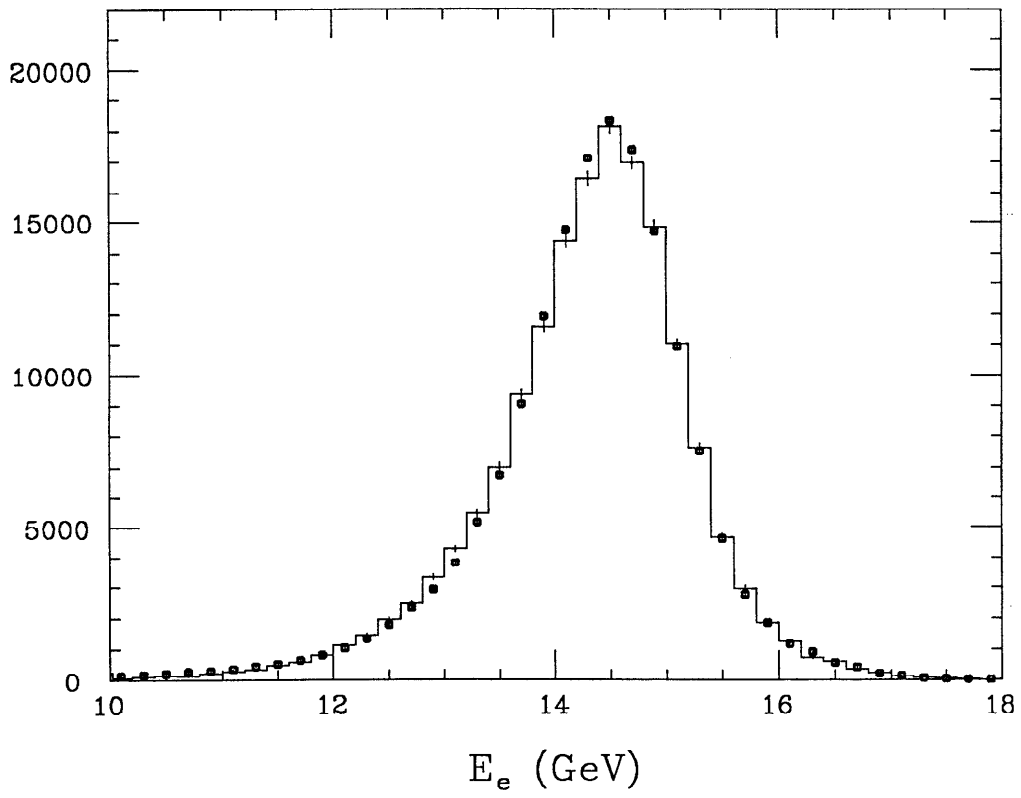

Figure 4.11. Liquid argon energy distribution for collinear Bhabha events. The data is shown by the points. The simulation, including smearing as described in the text, is given by the histogram.

tering events, collinear within 2 mrad. Figure 4.14 shows the distribution of liquid argon track energies for these events. The probability to reconstruct an isolated fake photon, with associated energy more than 300 MeV, is approximately 10^{-3}. Another source of fake photons is from the splitting of one shower into two by the reconstruction program. This effect is discussed further in the analyses of chapter 5.

4.4 Muon chambers

The muon detectors are not used in the analysis, and hence will be only briefly described. Four layers of muon chambers, separated by iron hadron absorber, make up each of the four walls that surround the central Mark II detector, as shown in fig. 4.1. A particle must transverse at least 7.2 interaction lengths of material in order to reach the fourth layer of the system. The complete system, however, covers less than 50% of the solid angle.

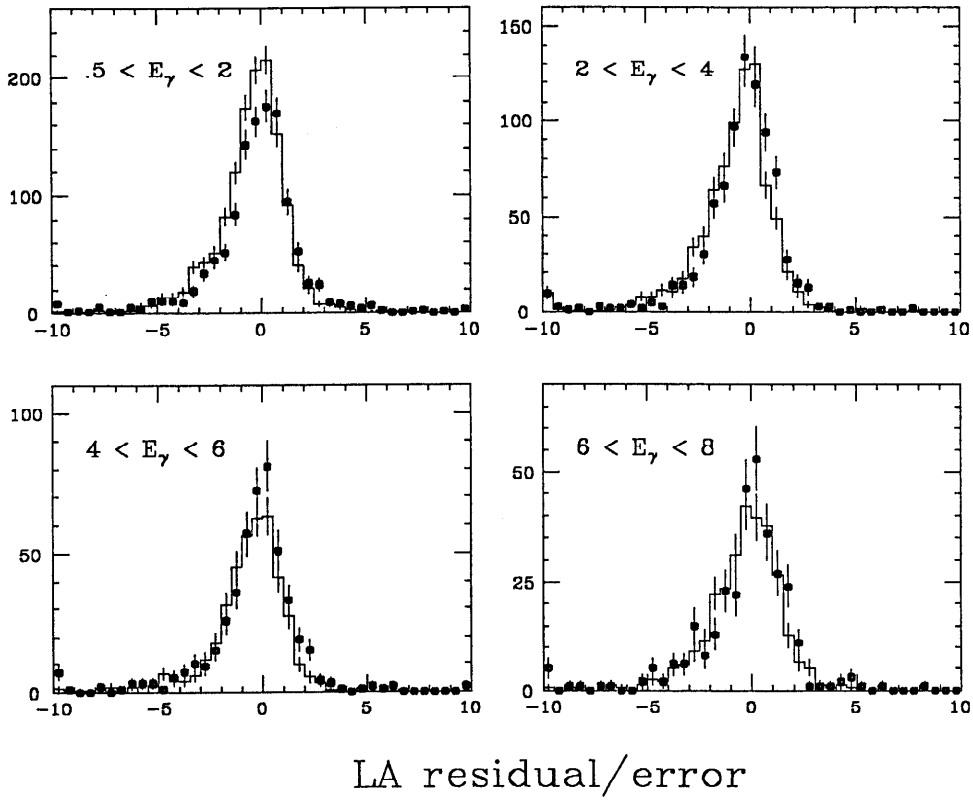

Figure 4.12. Difference of liquid argon measured energy and calculated photon energy divided by the expected standard deviation, $0.145\sqrt{E}$, for various energy photons from radiative Bhabha events. Points are the data; histograms are the simulation.

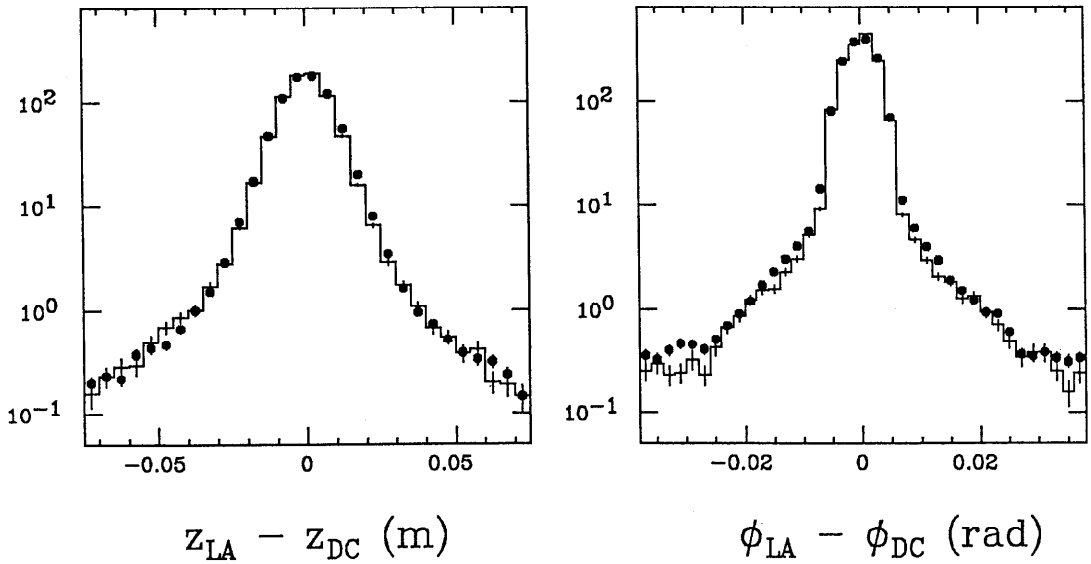

Figure 4.13. Difference of liquid argon measured shower position and drift chamber projected track position at the nominal trigger gap. Points are the data; histograms are the simulation.

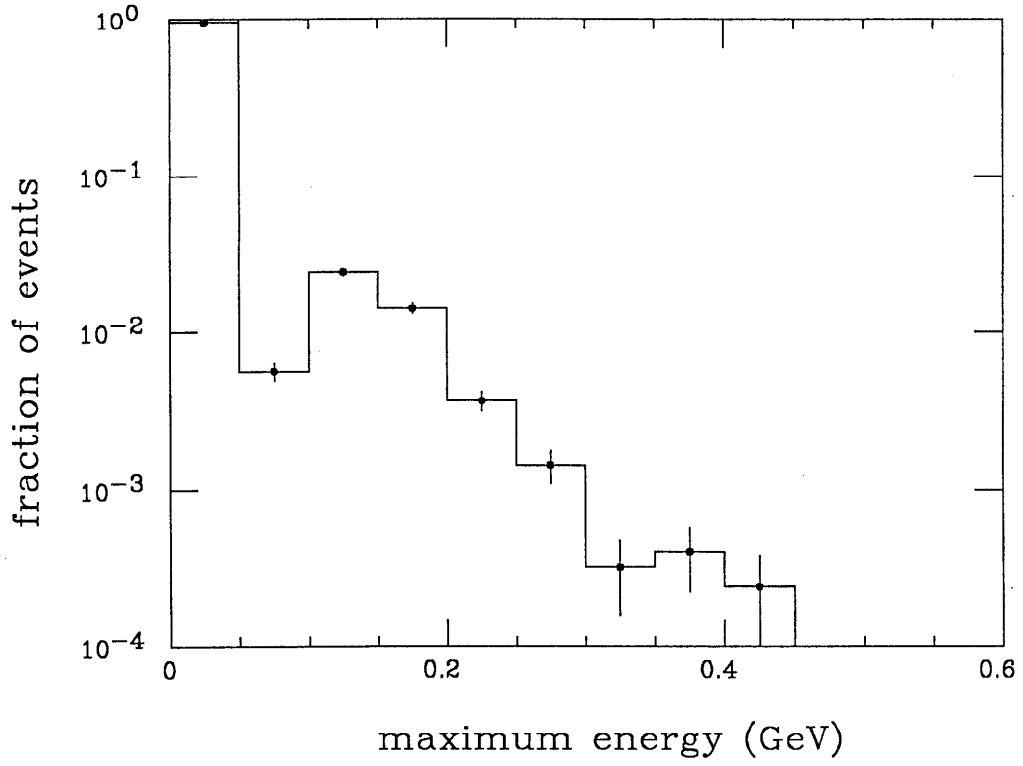

Figure 4.14. The maximum energy photon reconstructed in the liquid argon calorimeter per collinear small angle Bhabha scattering event (data only). The value in each energy bin is a measure of the probability for reconstructing fake photons from noise.

4.5 Endcap calorimeters

The endcap calorimeters, situated near the ends of the drift chamber, measure electromagnetic showers between the polar angles of 15° and 40°. They consist of only 2.3 radiation lengths of lead followed by two layers of proportional wire chambers. The system was not used in this analysis because of the rather poor energy resolution; $\sigma_E = 0.5\sqrt{E}$, high non-conversion probability and non hermetic geometry.

4.6 Small angle tagging system

The small angle tagging system (SAT) was designed to measure small angle Bhabha scattering and to tag the electrons in virtual two photon processes[61]. The system is used in the analysis of low Q^2 radiative Bhabha scattering to detect the small angle electron.

As shown in fig. 4.1, the SAT system consists of three sets of drift chambers and a shower counter that surround the beam pipe on both sides of the main detector and cover the region between 21 and 82 mrad. Each set of drift chambers consists of four planar drift chambers, two of which are shown in fig. 4.15. The principle of operation of the chambers is the same as discussed in section 4.1. In addition to the sense wires, there are inductive delay lines that measure the position along the sense wire, albeit much less accurately. Only in the four corners where the chambers overlap is there an accurate measurement of both coordinates.

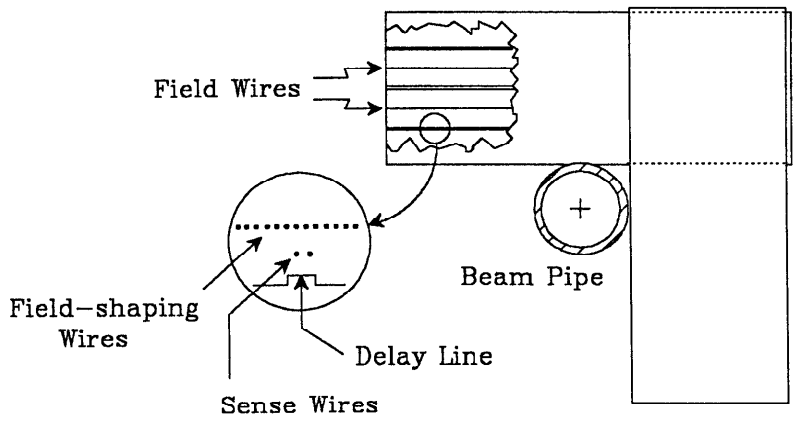

Figure 4.15. Two of the four planar drift chambers that make up one set of chambers for the small angle tagging system. Each chamber has six drift cells aligned along the length of the chamber. Inductive delay lines are placed near the sense wires for a rough measurement of the orthogonal coordinate.

The SAT shower counters, consisting of a sandwich of 18 layers of lead and plastic scintillator, are split into two modules to allow installation around the beam pipe. The modules are not segmented, so the shower counter does not provide information about the shower position within the module, only the total shower energy.

To study the SAT drift chamber performance, low angle Bhabha scattering events are selected on the basis of the shower counter energy. The azimuthal and polar angle differences from these events are shown in fig. 4.16, after a correction for misalignments between the two sets of SAT drift chambers.

The azimuthal angle resolution is 43 mrad in the regions where two drift chambers

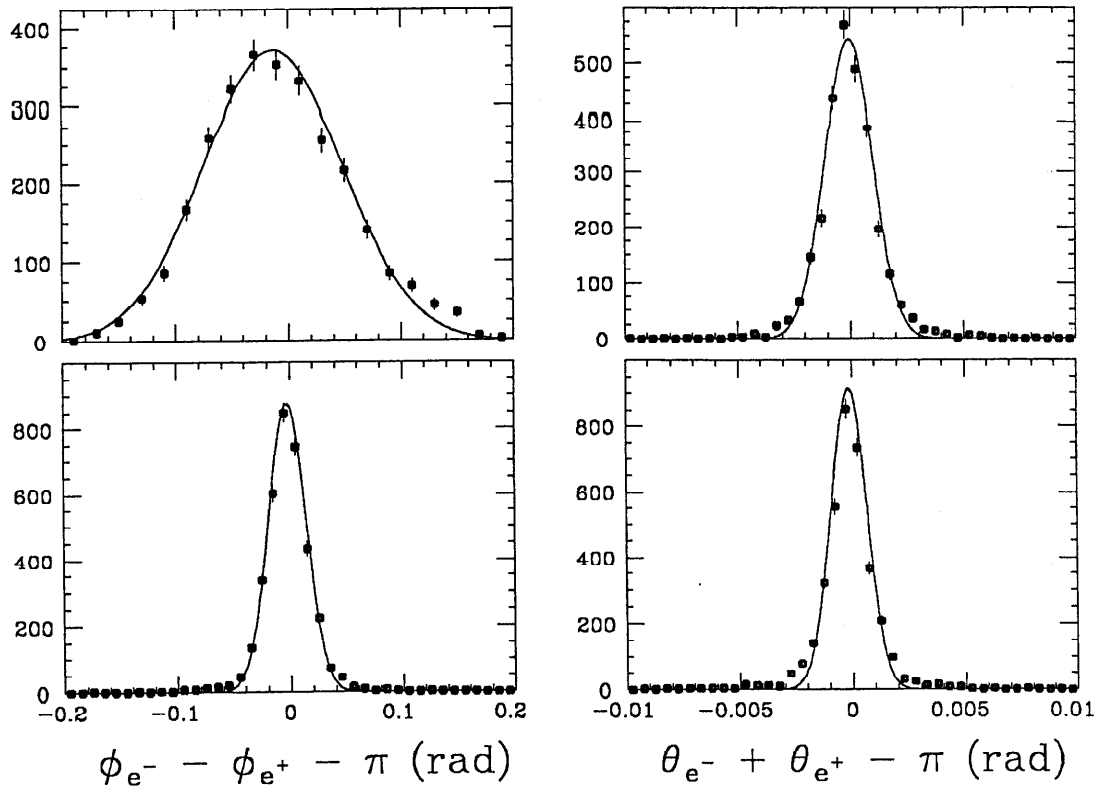

Figure 4.16. The difference of the azimuthal and polar angles for low angle Bhabha events. To improve the resolutions, the tracks are constrained to intersect the interaction point. The upper curves are for tracks that do not pass through the overlap regions. The azimuthal measurement is much more accurate in the four corners where the chambers overlap, as shown in the lower set. Gaussian curves are fit to the data to determine the resolutions.

do not overlap and 12 mrad in the overlap regions. The resolutions of the polar angle are 0.7 mrad and 0.6 mrad in the two regions. The same analysis on a Monte Carlo data set indicates that the detector simulation has 30% better resolution in the drift distance measurement. To compensate, noise is added to angular measurements for Monte Carlo data. To check the azimuthal alignment of the SAT system with respect to the main drift chambers, radiative Bhabha events with an electron in the central detector and in the SAT system (and the photon at 0°), are used. The efficiency of reconstructing SAT tracks that point to the interaction region is well modelled in the detector simulation.

The energy resolution of the SAT shower counters is measured with Bhabha events, selected with the drift chamber information to be collinear and away from the edges of the modules. The energy distribution, shown in fig. 4.17, is fit to a Gaussian curve of width 0.65 GeV.

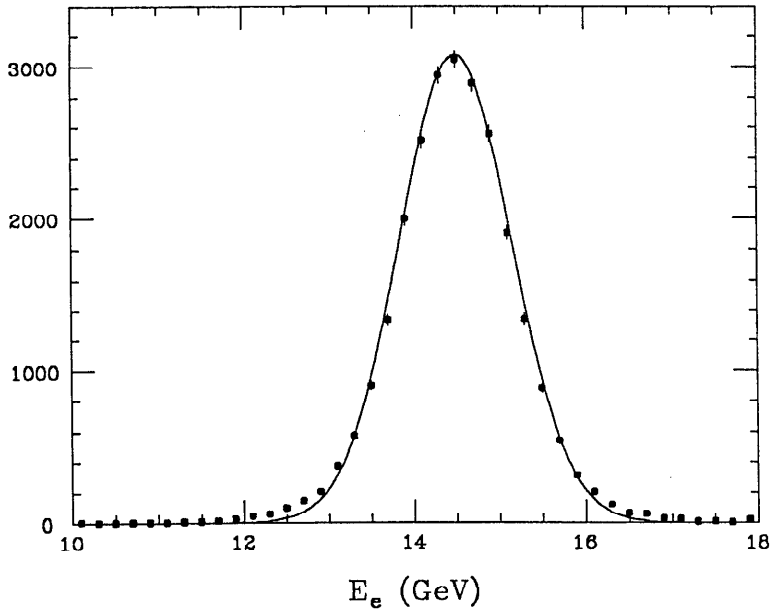

Figure 4.17. The distribution of energies measured by the SAT shower counters for collinear low angle Bhabha events. The Gaussian fit to the data has a width of 0.65 GeV.

Beam related contamination and electronics noise in the SAT system are evaluated with wide angle Bhabha events, collinear to 10 mrad. The distribution of SAT shower energies for these events is shown in fig. 4.18, and indicates that a threshold of 3 GeV is necessary to keep the fake shower rate at less than 10^{-3} per event.

The SAT acceptance is shown in fig. 4.19 a, where small angle Bhabha tracks are projected onto the plane perpendicular to the beam direction at the shower counter, approximately 5 m from the interaction region. The tracks were required to be consistent with originating from the interaction region, and the corresponding shower counter was required to have at least 3 GeV of deposited energy. The shape of the inner edge of the acceptance is square from the geometry of the planar drift chambers, and circular from tungsten masks. The horizontal strip, containing few events, corresponds to an inactive region between the shower counter modules. The edges of

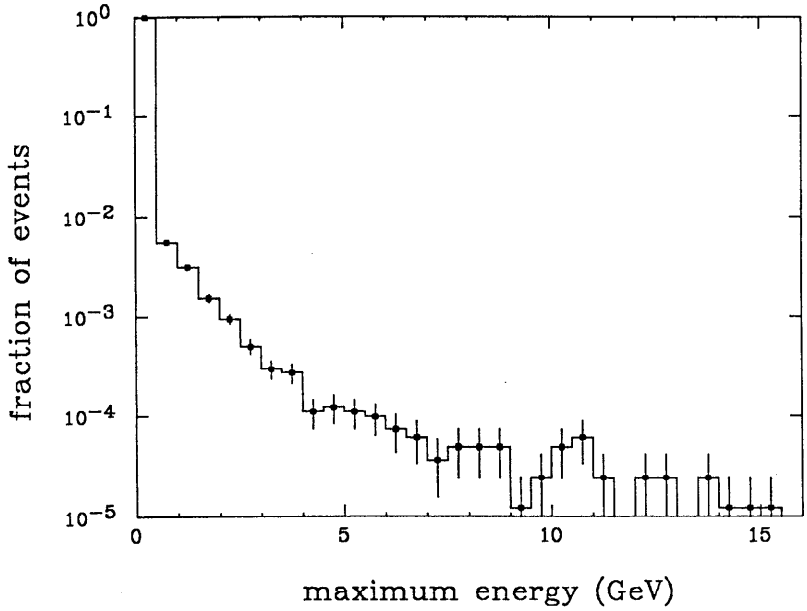

Figure 4.18. The maximum SAT shower per collinear wide angle Bhabha event.

the SAT system are not well modeled in the detector simulation, so a fiducial volume is defined well inside the active volume, as is done with the liquid argon system. The fiducial volume of the SAT is taken to be above 30 mrad in the polar angle and at least 3 cm from the crack between modules, as shown in fig. 4.19b.

4.7 Trigger

The relatively short time between electron and positron bunch crossings at PEP of 2.4 μs, makes it impossible to record every event. The detector electronics require about 40 ms for the signals to be read out and the recording of events to magnetic tape limits the rate to about 3 Hz. A factor of 10^5 reduction in events is accomplished by a two level programmable trigger. The primary trigger uses simple occupancy requirements in the drift chambers, liquid argon and SAT shower counters to reduce the number of events by a factor of 300. Events passing the primary trigger criteria are processed further by the more sophisticated secondary trigger, which searches for patterns in the drift chambers and time of flight system that could indicate charged tracks.

For the majority of the data, the secondary trigger track definition is a signal in two of the inner four vertex chamber layers, four inner and two outer main drift

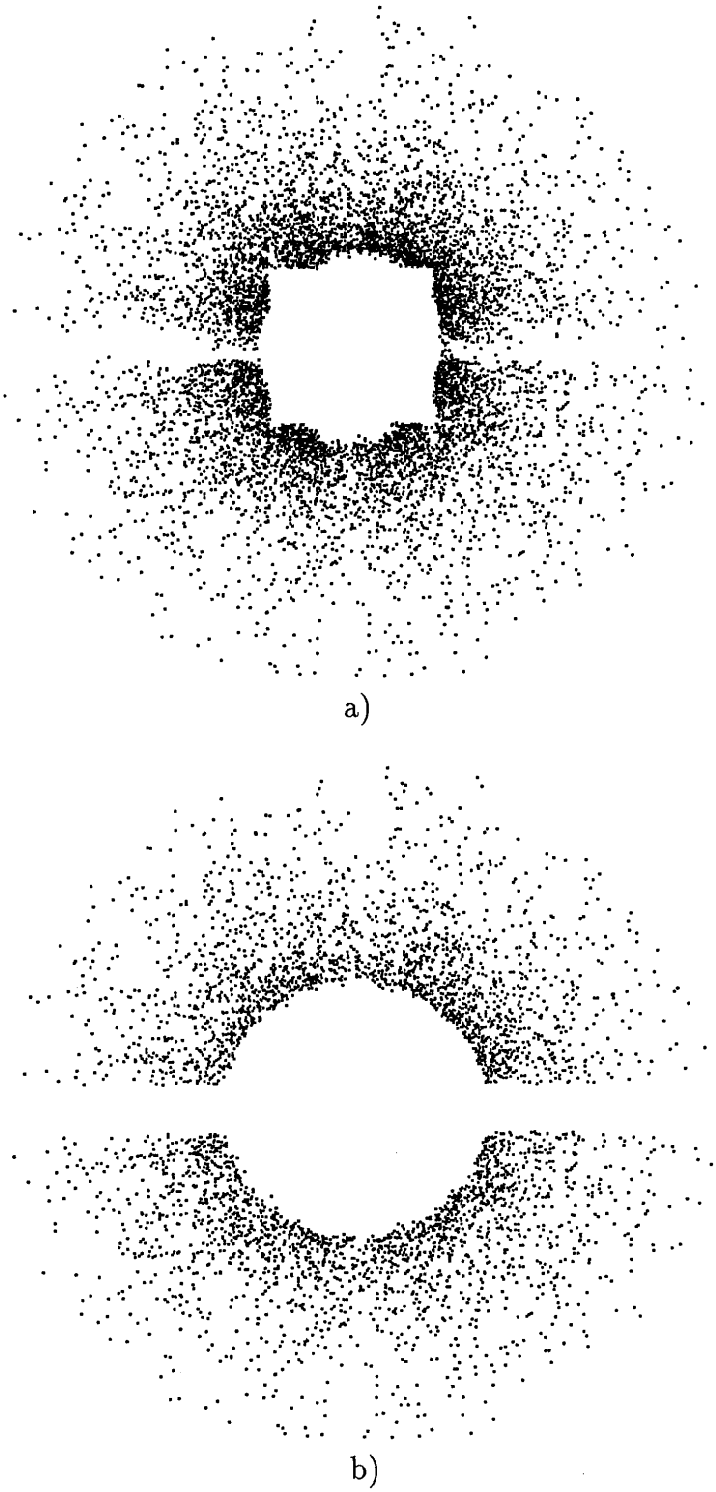

Figure 4.19. A map of the SAT acceptance. a) Electron tracks from small angle Bhabha events projected onto the plane perpendicular to the beam direction at the position of the shower counter, a distance of 5 m from the interaction point. b) The fiducial volume of the SAT system, avoiding the regions that are not well modeled by the detector simulation.

chamber layers, and a time of flight counter aligned in a 'road'. There are 22 roads defined of various curvatures, with corresponding momenta 130 MeV and above, used to recognize tracks. The secondary trigger requirement relevant to this analysis is that the number of charged tracks plus the number of liquid argon shower modules with total energy above a threshold of about 1 GeV is two or more.

The efficiency of secondary trigger track finding is 98.5%, as measured with Bhabha events, using the sample that pass the trigger on the basis of the liquid argon shower energy alone. The major contribution to the inefficiency is the time of flight counter requirement, since particles that pass near the edges and between counters are not detected.

The efficiency of the liquid argon module energy trigger is determine from radiative Bhabha events with isolated photons in the modules. The photon energies are calculated by the event kinematics and the efficiency of trigger versus this energy is shown in fig. 4.20. The efficiency of the total energy trigger for the sample of Bhabha events that pass the charged trigger requirement is greater than 99.6%.

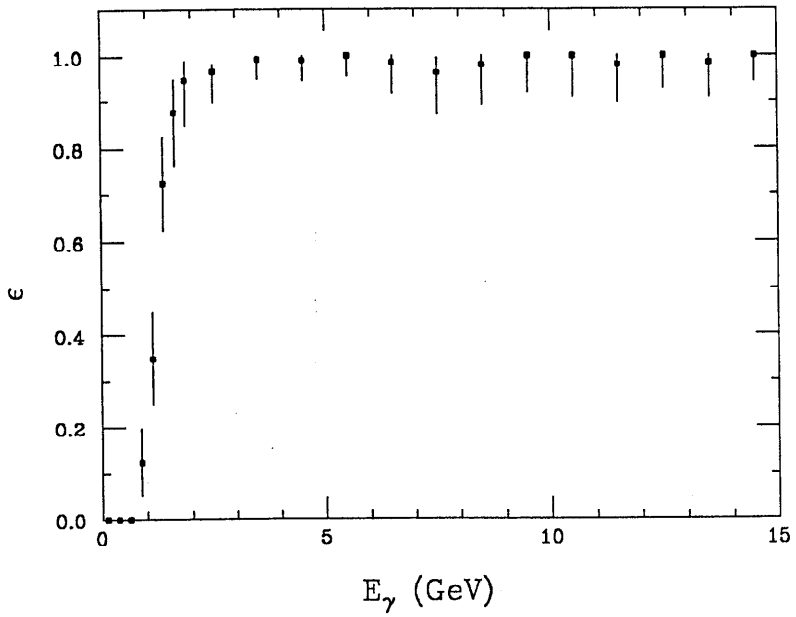

Figure 4.20. The efficiency of the liquid argon module energy trigger versus incident photon energy. Radiative Bhabha events are used with the photon energy determined by kinematics.

5

Experimental analysis and results

In this chapter, the experimental data from the Mark II detector are compared with the QED calculations from chapters 2 and 3. The first section presents the measurement of wide angle Bhabha scattering, which precisely determines the overall normalization. A description of the event selection and the analysis of low Q^2 radiative Bhabha scattering follows. Effects from electron compositeness are considered and a lower limit on the substructure energy scale is found. Finally, a study of exclusive double radiative Bhabha scattering is presented.

5.1 Normalization with Bhabha scattering

The conditions of the colliding e^+e^- beams are not sufficiently well known to calculate the integrated luminosity. Hence, some process must be measured with which all other reaction rates can be compared. Wide angle Bhabha scattering is chosen for this purpose for the following reasons. The lowest order process and the first order radiative correction are well understood, and a Monte Carlo event generator exists[23]. It has the largest cross section of all the QED processes, thus it will suffer the least from statistical errors. Also, the topology of Bhabha scattering events observed in the central part of the Mark II detector is very distinctive so that the analysis is highly efficient and nearly background free. Finally, the Bhabha analysis is very useful for studying detector performance as discussed in chapter 4.

5.1.1 Selection criteria

For a typical Bhabha scattering event, shown in fig. 5.1, the Mark II detector makes four independent measurements: the two electron tracks reconstructed in the drift chambers, and the two electromagnetic showers in the liquid argon calorimeters. Events are selected with very loose criteria so that the efficiency of accepting a Bhabha event in the fiducial volume is greater than 99%. In order to achieve such high efficiency, events with an unreconstructed or poorly measured track or shower are accepted. As well, events with extra tracks or showers, arising from radiative effects or errors in event reconstruction, are also allowed.

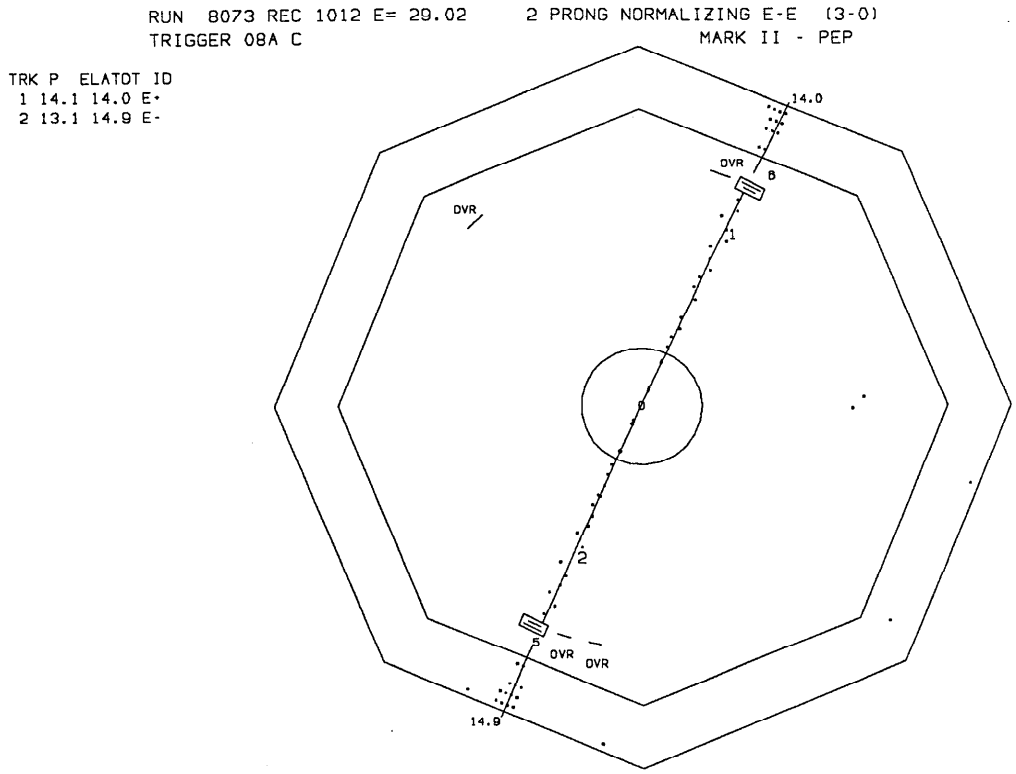

Figure 5.1. An event display of a typical Bhabha event in the Mark II detector. Shown is the projection of the event onto the plane perpendicular to the beam axis. The dots indicate cells in the drift chambers and strips in the liquid argon system with a signal. The lines through the points are the reconstructed tracks and showers.

Only the two largest momentum drift chamber tracks and the two largest energy liquid argon showers are considered in the event selection. All other tracks and showers are ignored. At least three of the maximum four tracks and showers must be acceptable. A drift chamber track (calorimeter shower) is acceptable if the reconstructed momentum (energy) is above 5 GeV/c (5 GeV) and it projects into the fiducial volume of the liquid argon system, as defined in fig. 4.9. Events with only a single acceptable shower are often cosmic rays, so that for these events, a time of flight counter must be associated for each of the two drift chamber tracks with a time measurement within 2 ns of the expected value. Since a cosmic ray takes about 10 ns to traverse the drift chamber, this background is reduced to a negligible level.

The events are required to have either two acceptable drift chamber tracks or an acceptable track-shower pair back to back within 400 mrad. Events with only a track-shower pair back to back can come from other sources, such as two photon annihilation, $e^+e^- \rightarrow \gamma\gamma$, where one photon converts into an e^+e^- pair. To reduce this background, such events are required to have cells hit in at least two vertex chamber and six main drift chamber layers within 45° in azimuth of the showers. This is a very loose requirement as shown in fig. 5.2.

Events from $e^+e^- \rightarrow \tau^+\tau^-$ would contribute about 1% of the signal because of the very low energy thresholds in this analysis. By requiring one liquid argon shower to have an energy greater than 10 GeV, the background is reduced to less than 0.2% with a very small loss in efficiency. Figure 5.3 shows the maximum liquid argon energy for Monte Carlo generated $e^+e^- \rightarrow \tau^+\tau^-$ and $e^+e^- \rightarrow e^+e^-$ events.

5.1.2 Comparison with Monte Carlo

The Berends and Kleiss Monte Carlo program[23] is used to evaluate the acceptance described above. The cross section for Bhabha scattering where the two electrons are in the region, $40° < \theta < 140°$, is calculated to be 1.676 ± 0.001 nb, approximately 5% larger than the lowest order result of 1.591 nb, given by[62],

$$\frac{d\sigma}{d\Omega} = \frac{\alpha^2}{4s}\left(\frac{3+\cos^2\theta}{1-\cos\theta}\right)^2 . \qquad (5.1)$$

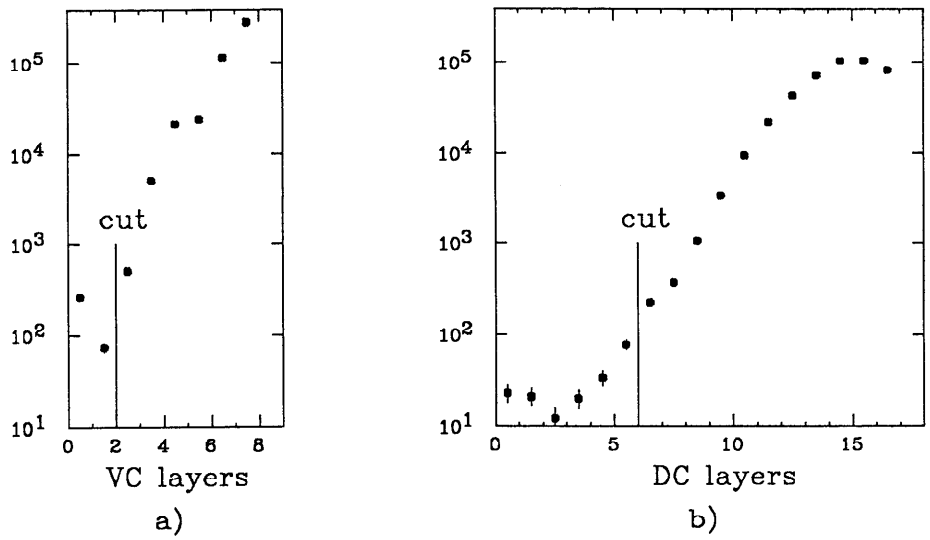

Figure 5.2. The number of layers with cells hit within 45° in azimuth from shower directions in Bhabha events; a) vertex chamber; b) main drift chamber. The cut lines indicate the minimum number of layers required to have cells hit for events without an acceptable back-to-back pair of drift chamber tracks. The events are selected by requiring two showers with measured energy above 10 GeV and more than 5 and 10 layers hit along the other vertex and main chamber track segments, respectively.

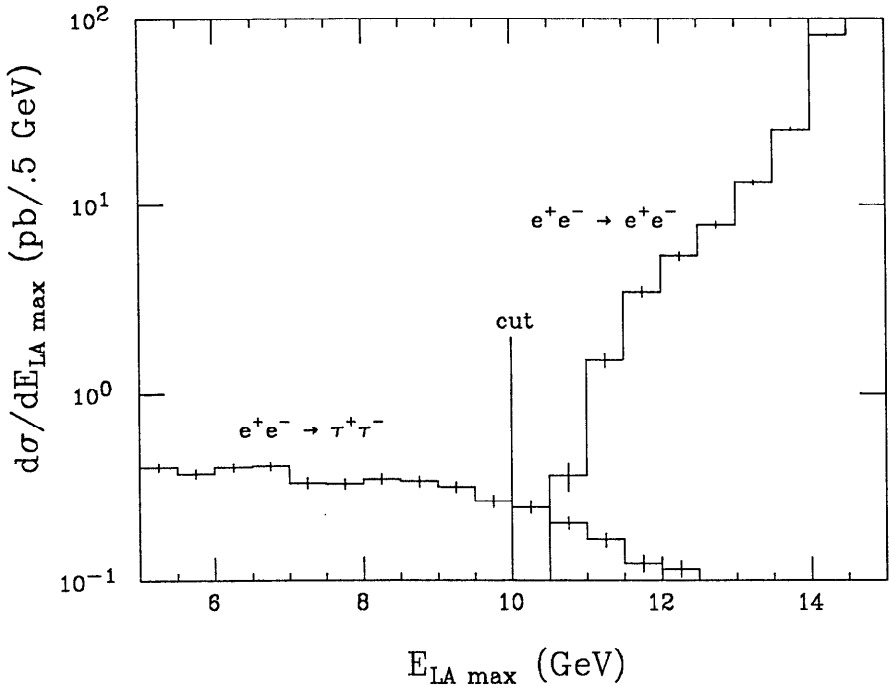

Figure 5.3. The maximum liquid argon shower energy from Monte Carlo data sets, without the additional smearing. To suppress the τ production background, all events are required to have one liquid argon shower with energy greater than 10 GeV.

A total of 151,346 events were generated, corresponding to an integrated luminosity of 90.3 pb^{-1}, and were passed through the detector simulation and event reconstruction programs. After applying the event selection criteria as described above, 68,968 events remain, so that the cross section for the acceptance of this analysis is 764 pb. In the data sample, 160,081 events are accepted which corresponds to an uncorrected integrated luminosity of 209.6 pb^{-1}. Figure 5.4 compares the angular distributions, as measured by the z coordinate at the nominal trigger gap, of the electrons with the Monte Carlo expectations. In fig. 5.5, the acollinearity distribution is shown and follows the Monte Carlo prediction well.

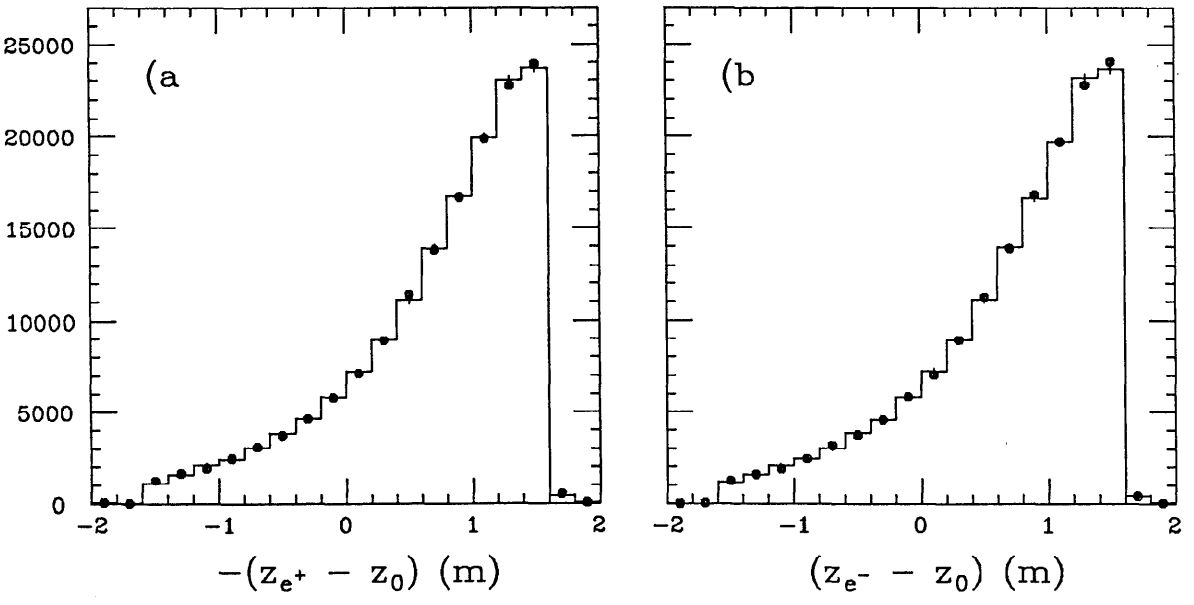

Figure 5.4. Comparison of data (points) with Monte Carlo (histogram) Bhabha events: a) $-z$ projection at the nominal trigger gap of positrons relative to the beam center; b) z projection at the nominal trigger gap of electrons relative to the beam center.

5.1.3 Background measurements and calculations

To calculate the background from τ pair production, Monte Carlo events generated from a program of Berends and Kleiss[63] are used. Of the 111,100 events, which correspond to 817 pb^{-1}, only 709 are accepted; a background of 0.11%. The contribution from μ pair production is similarly evaluated using another Monte Carlo

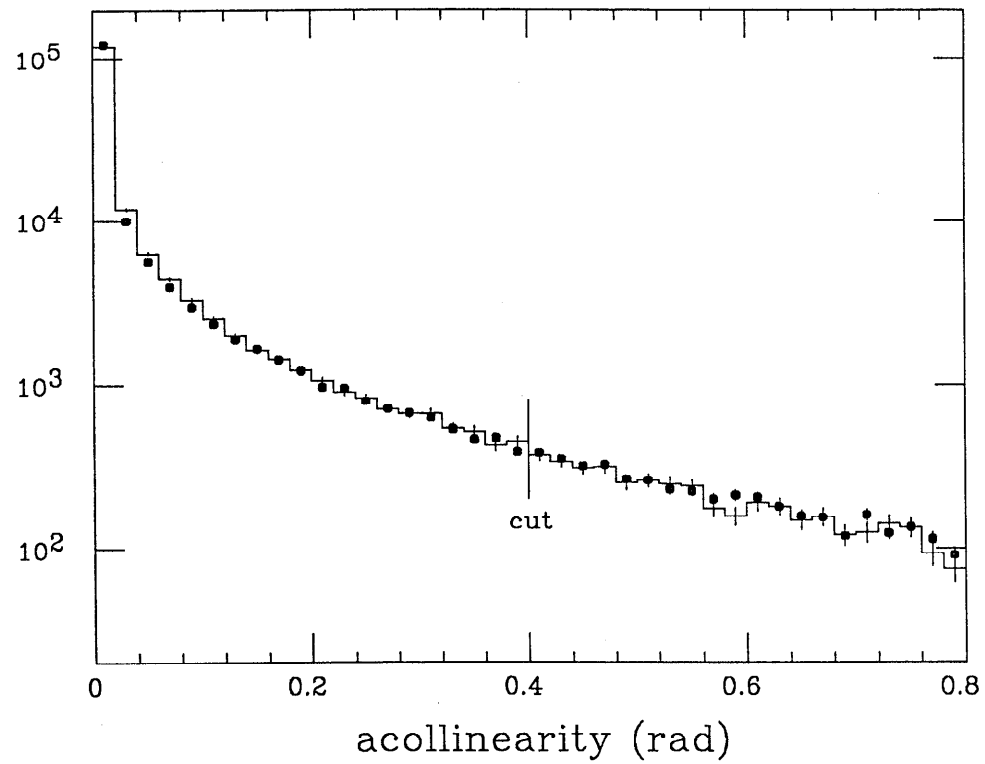

Figure 5.5. Acollinearity distribution of the data (points) and Monte Carlo (histogram) Bhabha events.

event generator[64] modified so that only radiative events are generated. In a sample corresponding to an integrated luminosity of 565 pb^{-1}, only 10 events pass the selection criteria, and so this is an insignificant background.

Since the muon chambers have not been used in the rejection criteria, they can be used to check the level of background from τ production, μ production and cosmic rays. Table 5.1 shows that the number of events with tracks through the four layers of the muon system is fairly consistent with Monte Carlo expectations from τ and μ production alone. Hence the cosmic background can be neglected.

The background from two photon annihilation, $e^+e^- \rightarrow \gamma\gamma$, in which photons convert in the detector, is evaluated with another Monte Carlo program[65]. Only 9 events in a sample of 234 pb^{-1} pass the Bhabha analysis. The background from radiative Bhabha scattering where one electron scatters below 40° is evaluated using the Monte Carlo program described in this thesis. Again the contribution is small; only 18 events pass from a sample corresponding to 268 pb^{-1}.

Table 5.1. Expected event rates with one or two tracks through four layers of the muon system compared to the measured number.

	1 track	2 tracks
τ production	14.1	0.0
μ production	1.5	1.5
total expected	15.6	1.5
Data	24	2

Other sources of background considered are two photon production of leptons and general hadronic production. Both of these sources are also found to be negligible.

5.1.4 Efficiency measurements

For the data set used in this thesis, the trigger is redundant for Bhabha events. If either more than one drift chamber track or more than one liquid argon module is found above threshold, the event is recorded. Of the 155,105 Bhabha events accepted by the track requirement, only 519 fail the liquid argon module threshold. And 4,960 of the 159,546 events that pass the liquid argon threshold fail the trigger track requirement. Hence the combined inefficiency of the two methods of triggering is 0.01%. The trigger is even more efficient because for the majority of data, events were also accepted if only one drift chamber track is found along with one liquid argon module above threshold. The combined trigger inefficiency for Bhabha events is extremely small, less than 0.002%.

The event reconstruction program contains a hardware filter program to reduce the amount of computing time spent processing uninteresting events. The efficiency of this filter for Bhabha events, estimated using data not subjected to this filter, is 99.92%.

The Bhabha selection criteria are designed to be redundant to ensure high efficiency and to allow measurement of the inefficiency to first order using the data. The inefficiency, $\bar{\epsilon}$, of the union of two uncorrelated sets, $\{A\}$ and $\{B\}$, is simply,

$$\bar{\epsilon}\{A \cup B\} = \bar{\epsilon}\{A\}\,\bar{\epsilon}\{B\} = \frac{n\{B\} - n\{A \cap B\}}{n\{B\}} \frac{n\{A\} - n\{A \cap B\}}{n\{A\}} . \qquad (5.2)$$

The full calculation is shown in table 5.2 where special notation is used to describe the Bhabha selection criteria. The total inefficiency from the Bhabha analysis program is only 0.15%.

5.1.5 Systematic errors

The largest systematic uncertainty comes from a possible discrepancy in the angular acceptance between the data and Monte Carlo. I first consider the systematic uncertainty on the scale and offsets of the z measurement.

The z measurements by the drift chambers and liquid argon calorimeter referred to in this analysis are projections along planes parallel to the faces of the LA modules at a radius of closest approach of 1.802 m, known as the nominal trigger gap. The radial offsets of the real liquid argon modules with respect to this nominal radius are found by matching drift chamber tracks with liquid argon showers. In order to find a possible scale error in the drift chamber z projection, I compare the measured z distribution with the expected shape. In fig. 5.6, the ratio of the data and Monte Carlo drift chamber z distributions for the positron (from fig. 5.4a) is shown, and is consistent with 1 ($\chi^2 = 17.8$ for 15 degrees of freedom). Also shown are curves expected if a systematic error that scales the z measurement was present, calculated using the lowest order formula, eqn. 5.1. This error is parametrized in terms of an offset, ΔR, in the radius at which the z is projected. By minimizing the χ^2, the most likely value for ΔR is found to be -0.25 ± 1.35 cm. This corresponds to a systematic error in the Bhabha acceptance of $0.23 \pm 1.24\%$.

An offset in the drift chamber measured z with respect to the beam position, is unlikely since Bhabha events are used to calculate the beam position. To check the sensitivity to a z offset, the analysis program was run with the beam center taken to be at the drift chamber center, and the acceptance was reduced by only 0.06%. A possible misalignment of the beam and the drift chamber z axis would only change the acceptance by less than 0.01%.

Small offsets between the liquid argon shower and drift chamber track measurements exist in the Monte Carlo generated data such that $z_{\mathrm{LA}} - z_{\mathrm{DC}} \approx 5$ mm and

Table 5.2. Calculation of the Bhabha analysis inefficiency. Set notation is used, along with a number of special symbols to describe the selection criteria in a concise way. n refers to the number of events in a set, and $\bar{\epsilon}$ refers to the inefficiency. In the calculation of $\bar{\epsilon}\{\not\tau\}$, a and b refer to the two largest energy liquid argon showers.

Set	Meaning
$\not\emptyset$	2 acceptable DC tracks and ≥ 1 acceptable LA shower
$\not\emptyset_{\diamond}$	2 acceptable LA showers and ≥ 1 acceptable DC track
$\swarrow\!\!\!\nearrow$	2 acceptable DC tracks back-to-back
$\swarrow\!\!\!\nearrow^{\diamond}$	≥ 1 back to back acceptable track-shower pair
$\not\phi$	not a cosmic; both DC tracks have a good time of flight
$\not\gamma$	not a gamma; enough drift chamber layers hit
$\not\tau$	not a tau; at least one LA shower above 10 GeV

Bhabha selection criteria:

$$\left[(\{\not\emptyset\} \cap \{\not\phi\}) \cup \{\not\emptyset_{\diamond}\}\right] \cap \left[\{\swarrow\!\!\!\nearrow\} \cup (\{\swarrow\!\!\!\nearrow^{\diamond}\} \cap \{\not\gamma\})\right] \cap \{\not\tau\}$$

Bhabha inefficiency calculation:

	Data	Monte Carlo
$n\{\text{accepted}\}$	160081	68968
$n\{\not\emptyset \cap \not\phi\}$	139684	62555
$n\{\not\emptyset_{\diamond}\}$	158863	68612
$n\{\not\emptyset \cap \not\phi \cap \not\emptyset_{\diamond}\}$	138466	62199
$\bar{\epsilon}\{\not\emptyset \cap \not\phi\}$	12.8%	9.35%
$\bar{\epsilon}\{\not\emptyset_{\diamond}\}$	0.87%	0.57%
$\bar{\epsilon}\{(\not\emptyset \cap \not\phi) \cup \not\emptyset_{\diamond}\}$	0.11%	.053%
$n\{\swarrow\!\!\!\nearrow\}$	144477	62776
$n\{\swarrow\!\!\!\nearrow^{\diamond} \cap \not\gamma\}$	159886	68934
$n\{\swarrow\!\!\!\nearrow \cap \swarrow\!\!\!\nearrow^{\diamond} \cap \not\gamma\}$	144282	62742
$\bar{\epsilon}\{\swarrow\!\!\!\nearrow\}$	9.76%	8.94%
$\bar{\epsilon}\{\swarrow\!\!\!\nearrow^{\diamond} \cap \not\gamma\}$	0.14%	0.05%
$\bar{\epsilon}\{\swarrow\!\!\!\nearrow \cup (\swarrow\!\!\!\nearrow^{\diamond} \cap \not\gamma)\}$	.013%	.005%
$n\{\not\tau_a\}$	157679	68389
$n\{\not\tau_b\}$	157749	68327
$n\{\not\tau_a \cap \not\tau_b\}$	155347	67748
$\bar{\epsilon}\{\not\tau\}$	.023%	.008%
$\bar{\epsilon}\{\text{Bhabha Analysis}\}$	0.15%	0.07%

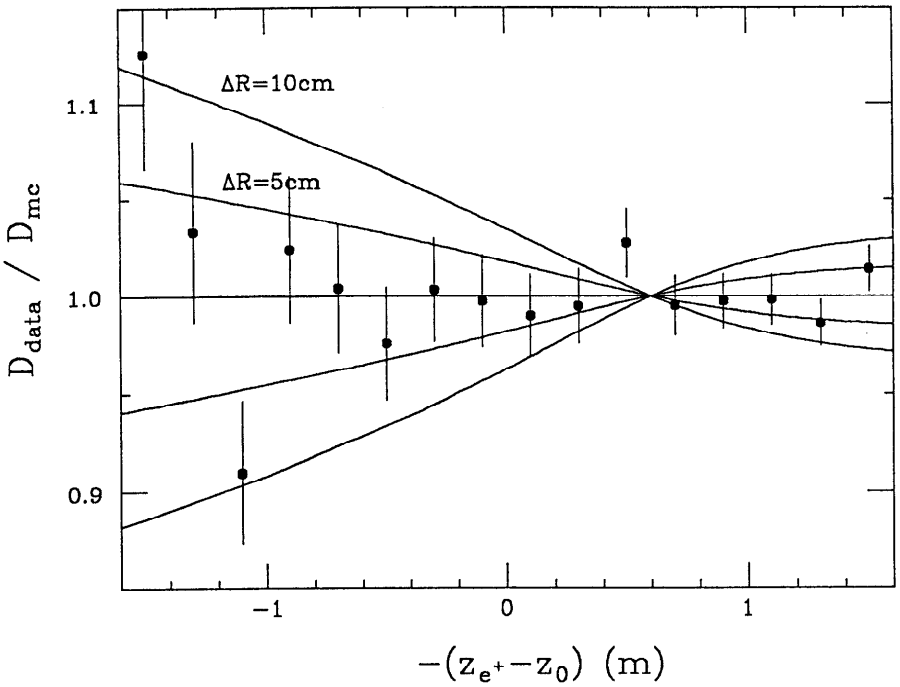

Figure 5.6. Ratio of the z distributions for data and Monte Carlo (points). The curves indicate the shape expected if the z measurement for data was made at the radius $R_{\rm data} = R_{\rm MC} + \Delta R$, for $\Delta R = 10, 5, 0, -5$ and -10 cm.

$\phi_{\rm LA} - \phi_{\rm DC} \approx 1$ mrad. After correcting for these offsets, the Monte Carlo acceptance changed by only 0.03%.

The systematic uncertainties in the efficiency calculations are presumed small since the redundant cuts are roughly uncorrelated and the total inefficiency is small. An exception to this is the filter against τ pair production (one liquid argon shower in the event must have more than 10 GeV). The two liquid argon shower measurements can be correlated (ie. both poor) because the Bhabha events are back-to-back and the detector is symmetric. If one track passes through a dead space in a liquid argon module (for example a support rod) there is a correlation for the other track to pass through a dead space as well. As mentioned before, the energy resolution of the liquid argon calorimeter is modeled poorly in the detector simulation (to improve this, random smearing is added as described in section 4.3), and dead spaces are not included. To check for a systematic error in this cut, the maximum liquid argon shower energy for events satisfying all the other analysis criteria is compared to the expected background in fig. 5.7.

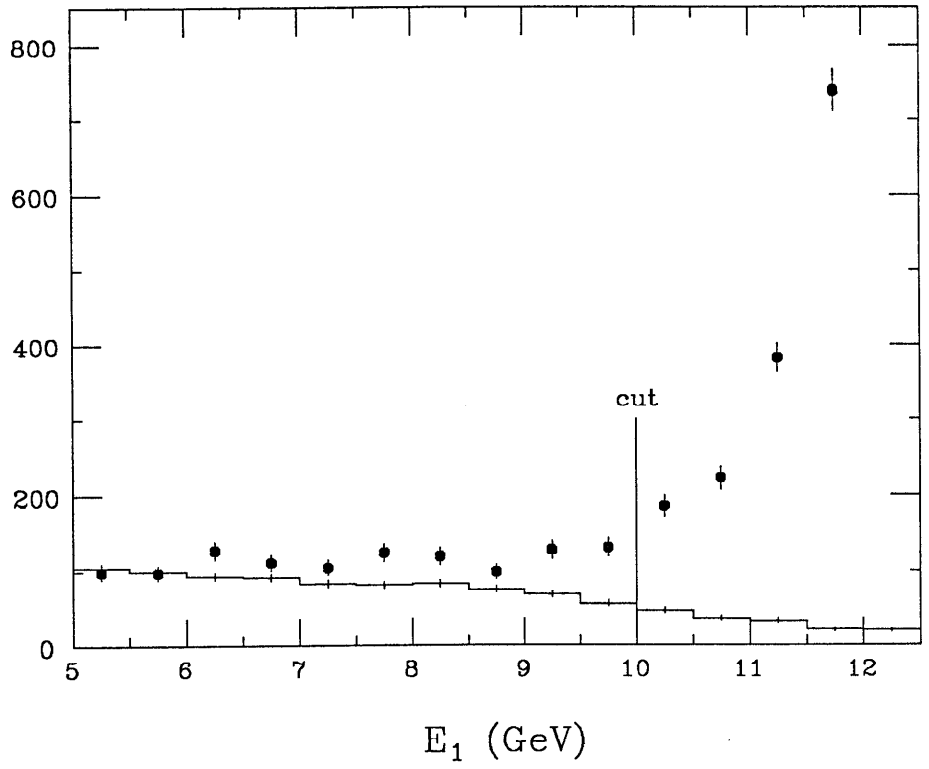

Figure 5.7. Maximum liquid argon energy measurement for the data (points) compared to the expected background from τ and μ pair production (histogram).

There are 1145 events in the region below 10 GeV, which is 313 ± 37 more than the expected background. The inefficiency of the $\not{f}$ cut, from table 5.2, is 0.02%, so that only 32 Bhabha events are expected to have the maximum liquid argon shower energy below 10 GeV. The number of events in this region with a track through four layers of the muon system is 169 compared to 184 ± 15 expected from backgrounds. Hence the extra events are not likely due to τ and μ production or cosmic rays. Since it is not known whether the extra events are signal or background, a systematic uncertainty of 0.2% is assigned to the $\not{f}$ cut.

The uncertainty in the calculation of the Bhabha cross section also contributes to the total systematic uncertainty. As mentioned in section 5.1.2, the calculated cross section, including the first order radiative correction, is only 5% larger than the lowest order result. Naively, one might expect that the next order correction would change the result by about 5% of 5% or 0.25%. I assign a systematic uncertainty of 0.5% to include effects from higher order corrections.

5.1.6 Summary of luminosity measurement

Table 5.3 summarizes the results of the luminosity measurement. The integrated luminosity of the data set used in this thesis is $209.2 \pm 0.5 \pm 2.9$ pb^{-1}, where the first error is statistical and the second is systematic. The systematic uncertainty is much larger than the statistical uncertainty and is dominated by the uncertainty of the scale of the z measurements.

Table 5.3. Summary of the luminosity measurement including the final corrected results.

	Data	Monte Carlo
Number of events	160081±400	68968±263
Background		
$e^+e^- \to \tau^+\tau^-$	181±7	-
$e^+e^- \to \mu^+\mu^-$	4±1	-
$e^+e^- \to \gamma\gamma$	8±3	-
$e^+e^- \to (e)e\gamma$	14±3	-
$e^+e^- \to e^+e^-e^+e^-$	8±4	-
$e^+e^- \to q\bar{q}$	2±1	-
Total Background	217±9	-
Inefficiency		
trigger	0.002%	-
reconstruction	0.08%	-
analysis	0.15%	0.07%
Total Inefficiency	0.23%	0.07%
Systematic error		
z scale	0.23±1.24%	-
z offset	0±0.06%	-
LA-DC offsets	0±0.03%	-
$\not{t}$ cut	0±0.2%	-
calculation of σ	-	0±0.5%
Total Systematic error	0.23±1.26%	0±0.5%
Corrected no. of events	159864±400±2014	69016±263±345
Luminosity (pb^{-1})	209.2±0.5±2.9	

5.2 Analysis of radiative Bhabha scattering

A typical low Q^2 radiative Bhabha scattering event, an $(e)e\gamma$ event, is shown in fig. 5.8. The low angle electron, not detected in this event, likely scattered below the small angle tagging system acceptance. If an electron scatters at 0°, the observed electron and photon balance momentum in the plane perpendicular to the beam direction, and hence are back to back in azimuth.

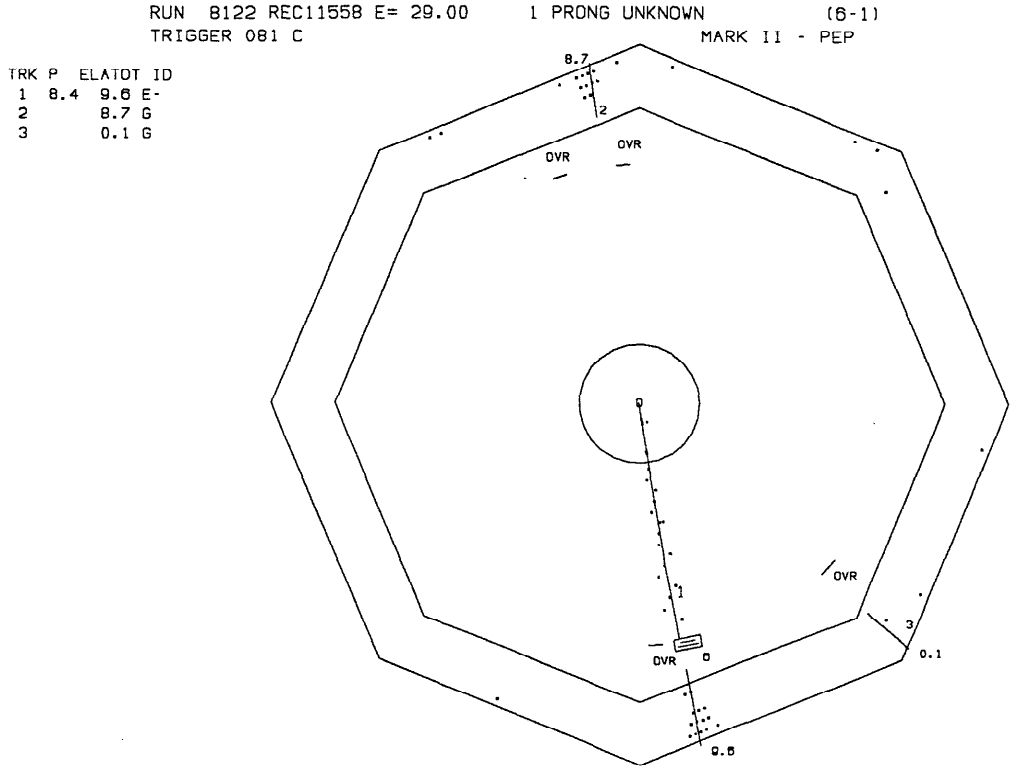

Figure 5.8. An event display of a typical $(e)e\gamma$ event in the Mark II detector.

5.2.1 Selection criteria

For the analysis of $(e)e\gamma$ events, a charged track and neutral shower are required to be inside the liquid argon system fiducial volume, each with more than 2 GeV of energy. This ensures that the liquid argon module energy trigger is fully efficient, as shown in fig. 4.20. The momentum of the charged track is required to be above 1 GeV/c.

Events with a second neutral shower in the liquid argon acceptance are treated separately in section 5.4. These events are excluded from this analysis if the extra shower is above 300 MeV and at least 30 cm away from the two primary showers. Figure 4.14, shows that a false 300 MeV shower due to random noise in the liquid argon system occurs in less than one event per 1000.

The largest backgrounds to the $(e)e\gamma$ process are from annihilation into two photons, $e^+e^- \rightarrow \gamma\gamma$, where one of the photons converts in the beam pipe or drift chambers and from Bhabha scattering, where one of the tracks is not reconstructed. Events from these sources are primarily back to back, and so to reduce this background, the electron and photon are required to have an acollinearity greater than 50 mrad. These backgrounds are further reduced by requiring a minimum number drift chamber layers hit for the electron (at least 2 of 7 vertex and at least 6 of 16 main), and few enough layers hit for the photon (less than 5 vertex and less than 7 main); all within 22.5° in azimuth of their liquid argon showers.

The Q^2 of the reaction must be limited to the region of validity of the equivalent photon approximation as discussed in chapter 2. A Monte Carlo data sample generated with the low angle electron below 100 mrad, is well within the limits of validity, as described in section 3.4.1. Since the central detector is better understood than the small angle tagging system, the central system information is used to select low Q^2 scattering. The observed electron and photon directions accurately define the event plane, on which the low angle electron lies. By requiring this plane to be within 50 mrad of the beam direction, most large Q^2 events are rejected. Figure 5.9 compares the z component of the normal to the event plane for Monte Carlo events with the low angle electron below and above 100 mrad.

5.2.2 Comparison to Monte Carlo

Before real events are reconstructed, some trigger information, such as liquid argon module energy sums and hardware track momenta, is used in a 'hardware filter' program. Monte Carlo events do not have this trigger information, so a different program is used to simulate the effect of the hardware filter. One of the requirements

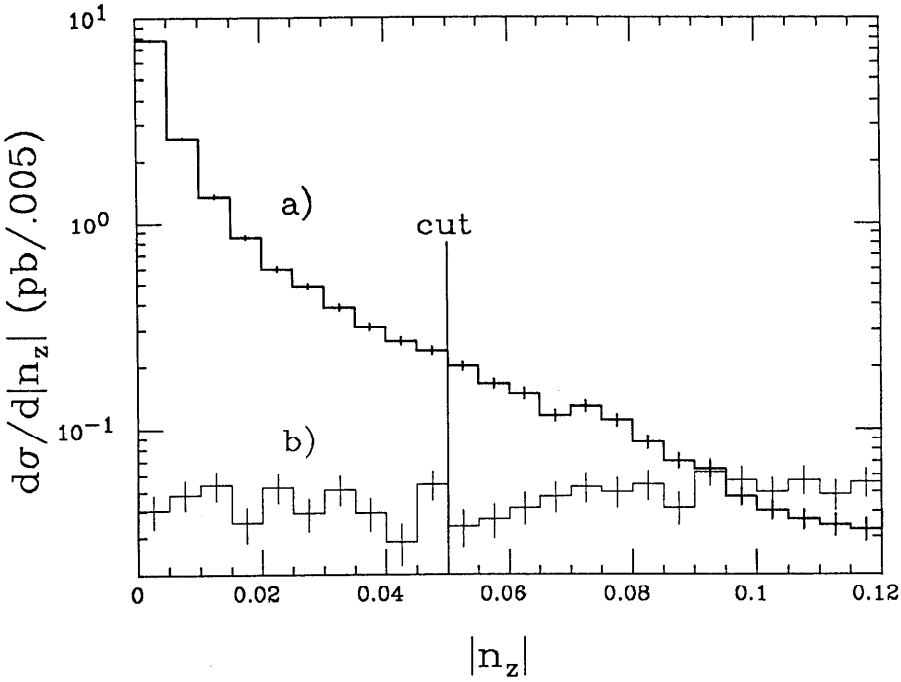

Figure 5.9. The absolute value of the z component of the normal to the event plane (ie. the sine of the angle of the plane with respect to the beam direction) for Monte Carlo $(e)e\gamma$ events with a) low angle electron below 100 mrad; b) low angle electron between 100 mrad and 300 mrad.

imposed is that the hardware liquid argon module energy sum is above 4 GeV. This is not efficient for events with energy near 4 GeV because the hardware sum only included the front halves of all the modules and hence is a poor measure of the total energy. The efficiency is measured as a function of energy, using a sample of data not subject to the hardware filter.

The other requirement of the hardware filter is much more complex and deals with the track finding electronics. As discussed in section 4.7, tracks are found at the trigger level by looking for alignments of drift cells along roads of various curvatures. The hardware filter uses the average curvature of all roads that the track lies along as a measure of the momentum, and filters against events with only a single low momentum track. For much of the data, however, a problem in the vertex detector electronics caused extra hits in neighbouring cells to appear which occasionally resulted in the average curvature being much larger than it should. The inefficiency of the curvature requirement, studied using Bhabha events which are not subject to this cut, is a

strong function of the azimuthal and polar angles. The filter simulation program, rejects Monte Carlo events with a probability according to this inefficiency function. The total inefficiency of this requirement for $(e)e\gamma$ events is about 1.5%.

In the following, the data is compared to an event sample generated by the Monte Carlo described in chapter 3. A total of 105,380 events, generated according to the configuration described in section 3.4.1 with a cutoff energy of 10 MeV, were passed through the detector and hardware filter simulation programs. Of these, 32,805 are accepted by the criteria described above, so that the cross section for the acceptance of this analysis is 14.88 ± 0.07 pb. For comparison, 30,000 events were generated according to the lowest order calculation, of which 13,884 are accepted, corresponding to a cross section of 13.60 ± 0.08 pb.

The sine of the angle of the event plane with respect to the beam axis is shown in fig. 5.10. For the region below the cut, the data and Monte Carlo agree well. Above the cut, there are fewer Monte Carlo events because the sample includes only events with the low angle electron below 100 mrad.

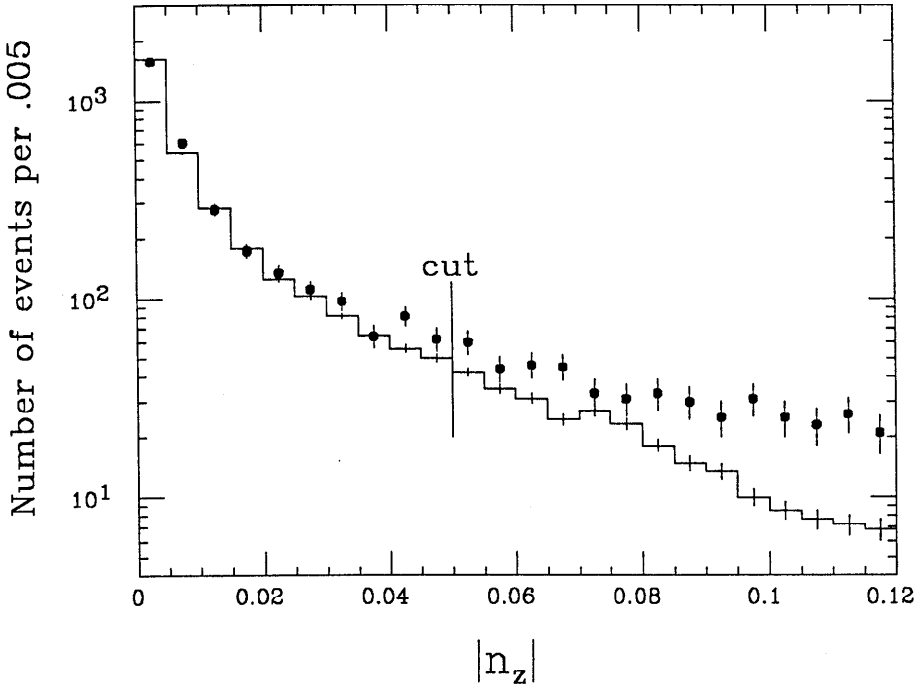

Figure 5.10. The sine of the event plane angle for $(e)e\gamma$ events for Monte Carlo (histogram) and data (points). The Monte Carlo curve is normalized to the luminosity as measured in section 5.1. Events to the left of the cut line are accepted by the analysis.

The angular distributions of the electrons and photons, as measured by the z coordinate at the nominal trigger gap, agree well with the Monte Carlo predictions, as shown in fig. 5.11. The shapes of the distributions for electrons and photons are different; the electrons tend to scatter at larger angles more often than the photons.

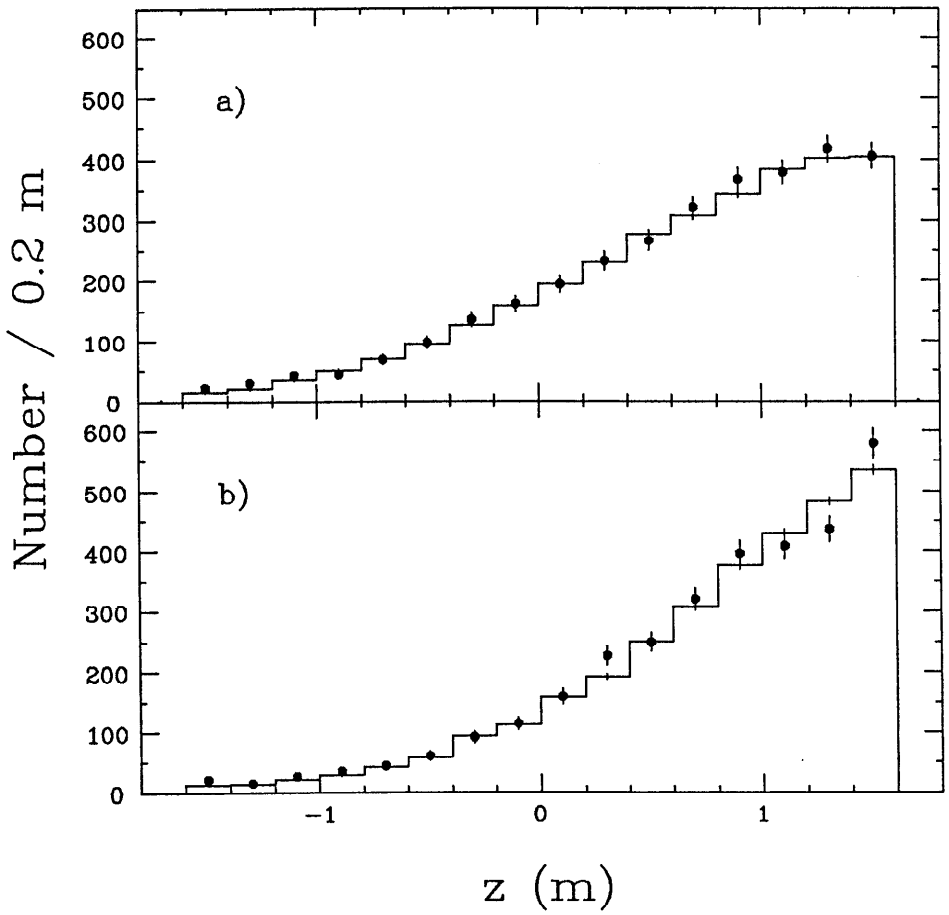

Figure 5.11. The z projection at the nominal trigger gap of the liquid argon system relative to the beam center (roughly proportional to the cosine of the polar angle). The measurements are multiplied by (-1) for events with a wide angle positron. a) electrons and positrons; b) photons.

The angular distribution and energy spectrum of the low angle electrons as measured by the small angle tagging system are shown in fig. 5.12. The tracks are required to be consistent with originating from the interaction point, be inside the fiducial volume of the SAT system, and have at least 3 GeV energy as measured by the shower counters. The distributions agree well with the Monte Carlo expectation. The fraction of events with a track in the fiducial volume of the SAT is $7.0 \pm 0.5\%$, compared

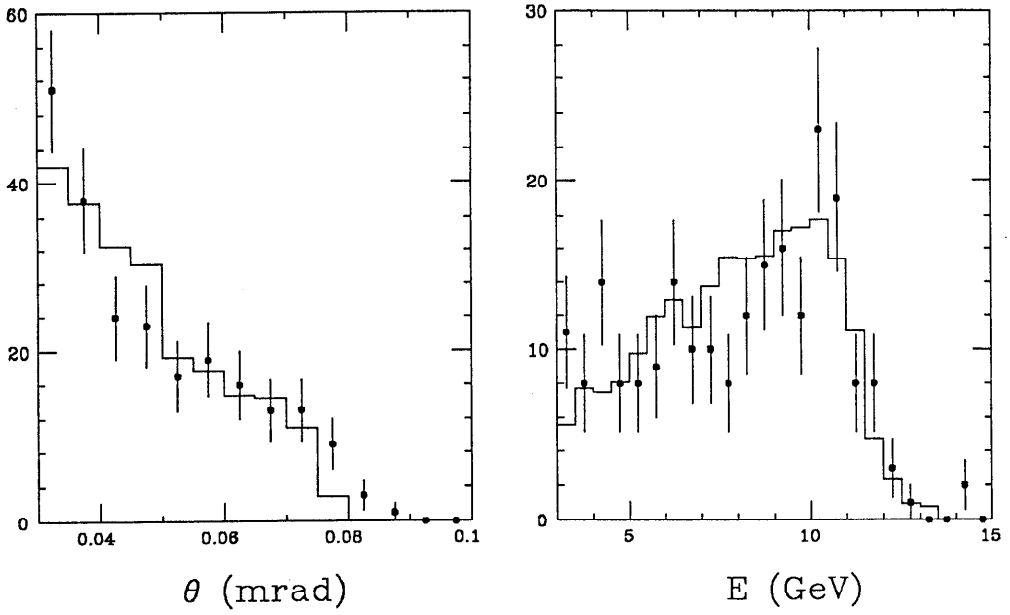

Figure 5.12. Distributions measured by the small angle tagging system: a) the polar angle ; b) the energy of the low angle electron.

to the Monte Carlo prediction of 7.1%.

The sum of the electron and photon energies in the central detector, the 'visible energy', is shown in fig. 5.13. The electron energy is determined by a weighted average of the liquid argon energy and the drift chamber momentum. Since the drift chamber momentum resolution has large tails, as shown in fig. 4.3, only the liquid argon energy is used if the two measurements disagree by more than 3 standard deviations. The visible energy distribution agrees very well with the order α^4 Monte Carlo prediction, but not with order α^3. As described in section 3.4.1, the low visible energy region is inaccessible to a 3 body final state, because of momentum conservation. The difference between the order α^3 and α^4 distributions shown here is not as dramatic as in fig. 3.4, because of the energy threshold in the trigger and hardware filter program, and the event plane angle requirement.

The low visible energy events must have a second photon to help balance the longitudinal momentum of the low angle electron. To better separate this event topology from the 3 body topology, and thus better test the fourth order correction,

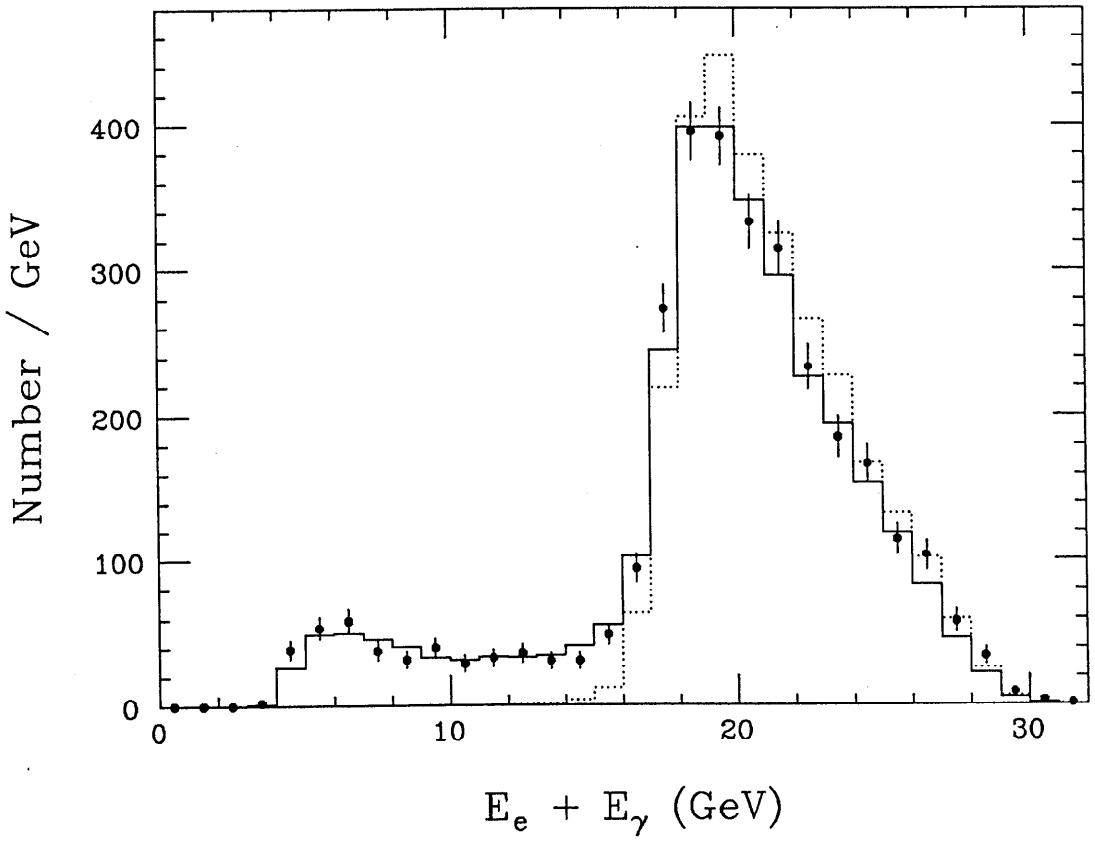

Figure 5.13. The sum of the electron and photon energies in the central detector. The points show the data, and the solid (dotted) histogram shows the order α^4 (α^3) prediction.

the mass of the missing particles,

$$m^2_{\rm miss} = E^2_{\rm miss} - |\mathbf{p}_{\rm miss}|^2 \ , \tag{5.3}$$

can be considered. This, however, is not convenient to use; so instead a related quantity[66] Δ is used,

$$\begin{aligned} \Delta &= E_{\rm miss} - |\mathbf{p}_{\rm miss}| \\ &= m^2_{\rm miss} / \left(E_{\rm miss} + |\mathbf{p}_{\rm miss}|\right) \ . \end{aligned} \tag{5.4}$$

The distribution of this quantity is shown in fig. 5.14, and is in excellent agreement with the order α^4 calculation. Three body final states have $m_{\rm miss} = \Delta = 0$, and hence the width of the distribution for the order α^3 prediction is due only to resolution effects.

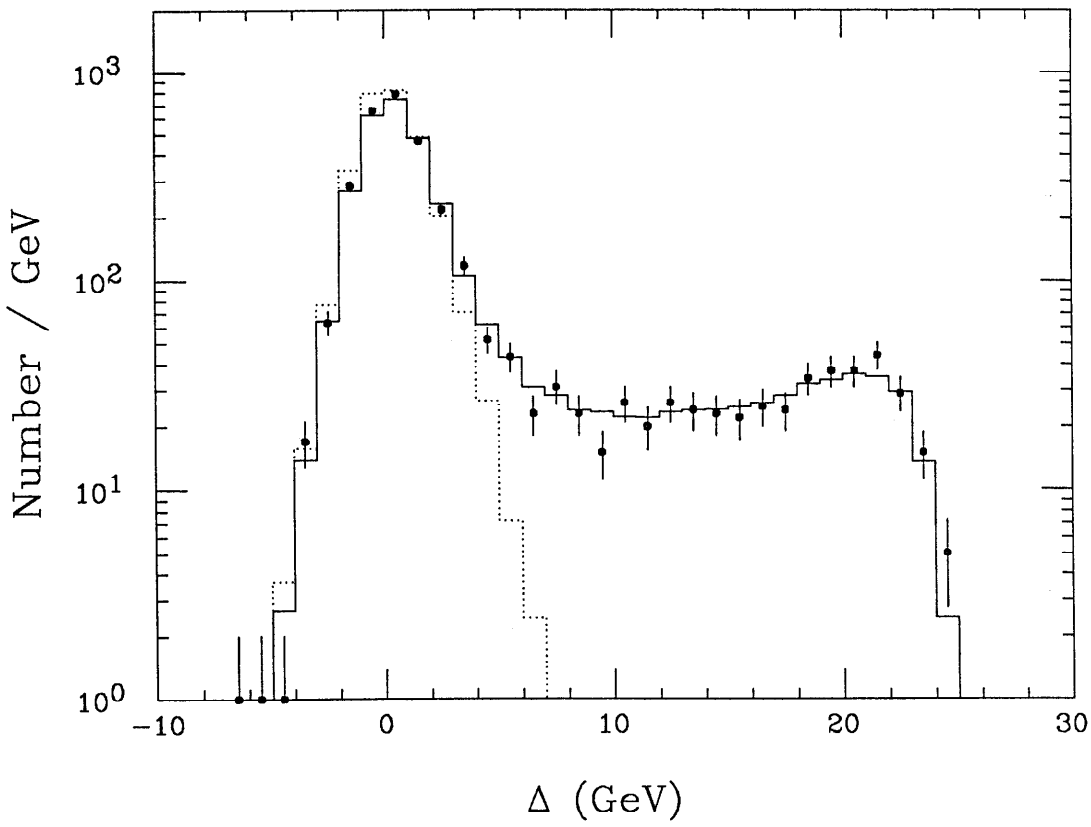

Figure 5.14. The distribution for the Δ function, defined in the text. The points show the data, and the solid (dotted) histogram shows the order α^4 (α^3) prediction.

A total of 3182 events in the data sample pass the selection criteria. Before comparison of this with the cross section calculated by the Monte Carlo, small backgrounds and inefficiencies not treated in the detector simulation need to be considered.

5.2.3 *Background calculations*

To estimate the number of accepted events in which both electrons scatter above 100 mrad, Monte Carlo events generated according to the lowest order cross section are used. In a sample of 268 pb^{-1}, 103 events pass the selection criteria. The enhancement from the next order correction is estimated to be $10 \pm 5\%$ using the comparison of order α^3 and α^4 cross sections when one electron scatters below 100 mrad. Hence, 88 ± 10 events from this source are expected to contribute to the accepted data sample. Curve b) in fig. 5.9, is from a Monte Carlo calculation to order α^4 in which the

low angle electron was allowed to scatter between 100 and 300 mrad. The equations used in calculating the radiative correction may not be accurate for such large Q^2, but indicate that 93 ± 5 events would contribute to the sample, consistent with the lowest order calculation.

The background from two photon annihilation, $e^+e^- \rightarrow \gamma\gamma$, where one photon converts in the detector material is evaluated using another Monte Carlo program[65]. In a sample of 234 pb^{-1}, only 35 events pass the $(e)e\gamma$ selection criteria, which corresponds to 31 ± 5 events in the data sample. The calculation of this background is very sensitive to the simulation of conversion probability and of two track separation by the drift chambers. To check the calculation, a measurement of such events is made. The material between the vertex and main chambers, 2.9% of a radiation length thick at normal incidence, is used as a convertor in this study. The $(e)e\gamma$ analysis is modified so that instead of requiring at least 2 cells hit in the vertex chamber along the electron track, less than 2 are required. Also, the acollinearity and event plane angle requirements are removed. A total of 544 events are accepted by the new criteria, whereas the Monte Carlo predicts 707 events. Hence the background from two photon annihilation is overestimated by 30%. The background from two photon annihilation hence is taken to be 24 ± 5 events.

5.2.4 *Efficiency calculations*

The liquid argon system trigger, which requires two modules to be above a threshold, is very efficient for $(e)e\gamma$ events. For 90% of the data, the trigger also accepts events with one module above threshold and one charged track, so that a single failure would not cause the event to be lost. The total efficiency of the liquid argon trigger for $(e)e\gamma$ events is estimated with a sample of data not subjected to the hardware filter, to avoid a bias. In this sample, 9 of 477 $(e)e\gamma$ events fail the liquid argon trigger, corresponding to an inefficiency of 1.9%. With the trigger track finding inefficiency of 1.5%, the overall trigger inefficiency is 0.25%.

During an initial filtering to select the $(e)e\gamma$ events, the total number of drift cells hit in an event is required to be less than 100. The inefficiency of this requirement is

found to be 0.15%, using the Bhabha event sample.

In the analysis, the wide angle electron is required to have momentum above 1 GeV/c, and have a shower greater than 2 GeV within 30 cm of its projection to the liquid argon system. The track finding and shower finding inefficiencies are found to be very small and well matched in the data and Monte Carlo using the Bhabha event sample.

The total inefficiency of requiring at least 2 of 7 vertex drift cells to be hit along the electron track and fewer than 5 hit along the photon direction is estimated to be 0.2% again using the Bhabha event sample.

Events with a second photon, of at least 300 MeV and isolated from the electron and photon by at least 30 cm at the nominal trigger plane, are treated separately in section 5.4, and are excluded from the $(e)e\gamma$ analysis. Occasionally a shower from a single incident particle will be split into two or more by the reconstruction program, thus causing an inefficiency in this analysis. When the energy and isolation thresholds are set to 600 MeV and 60 cm, 31 additional events are accepted, whereas the Monte Carlo predicts only 14. No additional Monte Carlo events from the background process, $e^+e^- \rightarrow \gamma\gamma(\gamma)$ with conversion, are accepted. False separated showers arising from reconstruction errors, tend to line up along the strip directions of the liquid argon system. The azimuthal angle of extra showers about the primary electron and photon showers in the plane parallel to the liquid argon module faces is shown in fig. 5.15. The lead strips lie along $\pm 90°$ (T strips), $0°$ (F strips), and $-45°$ (U strips) in the figure. A number of extra false showers are found by the reconstruction program along the U direction. These tend to be assigned within 30 cm of the primary shower, and hence do not cause events to be rejected. False showers assigned beyond 30 cm from the primary, tend to line up along the F strips. To estimate the number of events rejected because of false isolated showers, the seven events with extra showers in the same module as the primary photon are used. Of these, one event is determined to be a background event by hand scanning. Assuming the same likelihood of reconstructing extra false showers in the module of the electron, a total of 12 events are presumed lost, corresponding to an inefficiency of 0.4%.

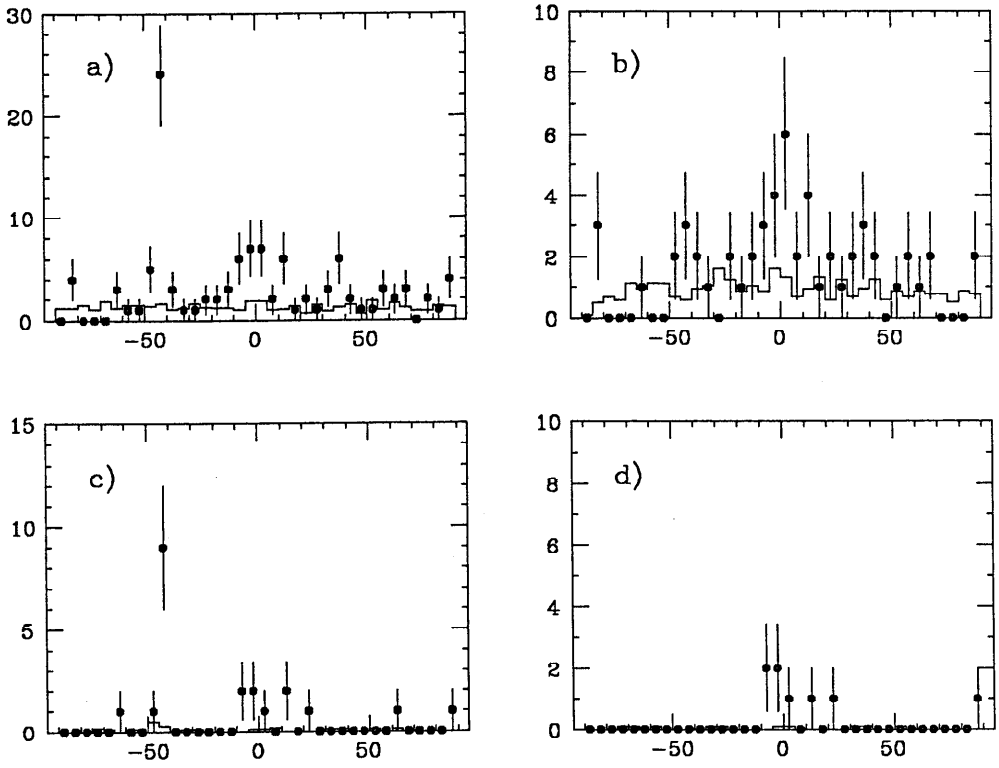

Figure 5.15. The azimuthal angle of extra showers about the primary electron and photon showers in the plane parallel to the liquid argon module faces (in degrees) for data (points) and Monte Carlo (histograms). The lead strips lie along the directions, $-90°, -45°, 0°$, and $90°$. a) extra showers relative to either primary electron or photon showers; b) extra showers relative to either primary electron or photon showers separated by 30 cm or more; c) extra showers relative to primary photon showers; d) extra showers relative to primary photon showers separated by 30 cm or more.

5.2.5 *Systematic errors*

The hardware filter simulator for Monte Carlo data, which removes 2.7% of otherwise acceptable $(e)e\gamma$ events, is a possible source of error. The measurement of the inefficiency of the liquid argon energy sum requirement is inaccurate, since only 16% of the data is used. However, the inefficiency is only important for low visible energy events, of which there are few. By varying the inefficiency within its uncertainty, the total number of accepted Monte Carlo events changes by 0.4%.

The measurement of the inefficiency of the hardware track momentum requirement does not suffer from statistical uncertainties since the Bhabha event sample is used. The cause of the extra vertex chamber hits, which creates the inefficiency,

however, is not fully understood, and so the use of the Bhabha events for the measurement may be incorrect. Only 8% of the data was not subjected to this cut and this data was taken at a time when the inefficiency was small. In this sample, 5 events are seen not to pass the track requirement, where only 2.8 events are expected. The total inefficiency for the complete data set is approximately 1.5%, and the uncertainty is taken to be 0.5%.

As described in section 4.1, the drift chamber momentum resolution is not accurately reproduced in the detector simulation. The $(e)e\gamma$ analysis requires the momentum of the wide angle electron to be above 1 GeV/c, and in order to check for a possible systematic error, the cut is raised to 2 GeV/c. After this change, 30 fewer events pass the selection criteria, in agreement with the Monte Carlo prediction of 27, so this systematic uncertainty can be ignored.

The electron is required to have an associated shower of at least 2 GeV in the liquid argon system. The track reconstruction program includes an algorithm for associating drift chamber tracks with liquid argon showers, but since it is also used in the study of high multiplicity events, it is somewhat inefficient. In the $(e)e\gamma$ analysis, the inefficiency is reduced by associating the closest shower of 2 GeV or more within 30 cm of the projected drift chamber track when the reconstruction program has not made an association. This additional association adds 64 events to the accepted sample, whereas the Monte Carlo predicts 34 $(e)e\gamma$ events and 12 ± 4 background events from $e^+e^- \rightarrow \gamma\gamma$ with conversion. If the radius of association is increased from 30 cm to 60 cm, an additional 36 events are accepted, compared to the Monte Carlo prediction of 7 signal and 12 ± 4 background events. The background from two photon annihilation with a conversion does not completely account for the additional events seen in the data relative to the Monte Carlo. The systematic uncertainty due to the association of drift chamber tracks and liquid argon tracks is taken to be 0.5%.

The systematic uncertainty of the measurement due to a possible scale error in the measurement of z is evaluated with an analytic integration of the lowest order cross section, referenced in section 3.4.1. The scale error is parameterized in terms of an offset, ΔR, in the radius at which the z measurement is projected, as discussed in

section 5.1.5. The relative effect on the total cross section, summarized in table 5.4, leads to a systematic error of $0.4 \pm 2.1\%$. This systematic uncertainty will be partially cancelled in the ratio with the measured integrated luminosity.

Table 5.4. Summary of the calculation of the systematic error in the $(e)e\gamma$ cross section due to a possible scale error in z. The lowest order cross section is integrated over the acceptances given by the allowed range of the error parameter, ΔR. The relative change in the cross section is a measure of the systematic uncertainty.

ΔR (cm)	$\cos(\theta_{\min})$	σ (pb)	$\Delta\sigma$ (%)
0	0.66395	19.460	-
-0.25	0.66447	19.532	$+0.37$
-1.60	0.66726	19.962	$+2.58$
$+1.10$	0.66169	19.147	-1.61

The beam center is measured using Bhabha events, in terms of an offset from the center of the drift chambers. The systematic uncertainty due to a possible error in the determination of z offset is evaluated by setting this parameter to zero. Eight fewer events are accepted, corresponding to a systematic uncertainty of 0.3%.

5.2.6 Summary of the cross section measurement

Table 5.5 summarizes the results of the cross section measurement of low Q^2 radiative Bhabha scattering in the Mark II detector. The total cross section is $14.77 \pm 0.26 \pm 0.21$ pb, where the first error is statistical and the second systematic, and is in excellent agreement with the calculated value of 14.88 ± 0.07 pb. The ratio of measured to calculated cross sections is $R = 0.993 \pm 0.017 \pm 0.015$.

The measured charge asymmetry,

$$\frac{N_+ - N_-}{N_+ + N_-} ,$$

where N_+ (N_-) is the number of events with a wide angle e^+ (e^-), is $3.0 \pm 1.8\%$. The hardware filter track requirement is less efficient for tracks pointing in the $+z$ half of the detector than in the $-z$ half. The asymmetry due to this effect is expected to be $0.8 \pm 0.6 \pm 0.3\%$. The corrected charge asymmetry is hence, $2.2 \pm 1.9\%$, consistent with 0.

Table 5.5. Summary of the measurement of the $(e)e\gamma$ cross section. The inefficiencies listed are those not included in the detector simulation. The uncertainty in the background and inefficiency calculations are included in the total systematic error. The z scale uncertainty, separated from the total systematic uncertainty, is partially cancelled in the ratio with the measured luminosity. Listed with the measured cross section are, in order, the statistical, systematic, and z scale uncertainties.

Number of events	3182±56
Background	
wide angle $e^+e^- \to e^+e^-\gamma$	88±10
converting $e^+e^- \to \gamma\gamma$	24±5
Total Background	112±11
Inefficiency	
trigger	0.25%
drift cell occupancy	0.15%
vertex layer occupancy	0.2%
extra false showers	0.4±0.2%
Total Inefficiency	1.0±0.2%
Systematic error	
hardware filter: energy sum	0.0±0.4%
hardware filter: track cuts	0.0±0.5%
track - shower association	0.0±0.5%
z scale	0.4±2.1%
z offset	0.0±0.3%
background and inefficiency	0.0±0.4%
Total Systematic error	0.4±1.0±2.1%

Corrected no. of events	3089	±	56	±	31	±	65
Luminosity (pb^{-1})	209.2	±	0.5	±	1.3	±	2.6
Cross section (pb)	14.77	±	0.26	±	0.17	±	0.13

5.3 Test of electron compositeness

The results of section 5.2 indicate that QED describes the high energy interactions of electrons and photons very well. A deviation from the QED predictions is expected if electrons are not point particles, but rather composites of some other more fundamental particles. No evidence for electron substructure is seen in this or any other experiment to date, but there are still many reasons for believing that the electron and the other leptons and quarks may not be fundamental.

Throughout the history of the study of matter, all things were thought to be made of a common set of basic elements. As the number of basic elements increased, it became clear that these basic elements themselves were made of yet more fundamental elements. This process went through several iterations from atoms to nuclei to nucleons and finally to quarks. The current list of fundamental particles, containing 5 flavours of quarks (each with 3 colours) and 6 flavours of leptons, is no longer short, suggesting that the next level of substructure may soon become apparent.

The reason why leptons and quarks are organized into families and why there are (at least) three such families of different masses may be understood in terms of the spectroscopy of more fundamental particles. Substructure may also explain the various simple charge relations and the electro-weak universality amongst the quarks and leptons. With compositeness, the number of free parameters may be reduced to a very small number. Various attempts to develop a consistent theory of composite quarks and leptons are reviewed in refs. 67 and 68.

Effects of electron compositeness might be observed through a new four electron coupling. Reference 69 shows that such a coupling significantly alters the Bhabha cross section and finds that the energy scale of electron compositeness must be above 750 GeV to be consistent with experimental data.

Electron compositeness may also become apparent because of the existence of new excited states which couple to electrons and photons. The simplest gauge invariant coupling is of the form[70],

$$\frac{e}{2}\left(\frac{\lambda}{M_{e^*}}\right)\bar{\psi}_{e^*}\,\sigma_{\mu\nu}\,\psi_e\,F^{\mu\nu}+\text{h.c.}\,, \tag{5.5}$$

and although non-renormalizable, may describe the effective low energy coupling. Experimental results from precision low energy tests of QED put strong constraints on such excited states[71]. The most precise low energy measurement is that of the anomalous magnetic moment $(g_e - 2)$ of the electron[72]. Renard[73] has shown that the coupling constant, λ/M_{e^*}, in eqn. 5.5, must be less than 1/22 TeV to be consistent with the $(g_e - 2)$ measurement. If the excited electron couples only to one helicity, as in

$$\frac{e}{2}\left(\frac{\lambda}{M_{e^*}}\right)\bar{\psi}_{e^*}\,\sigma_{\mu\nu}\left(\frac{1-\gamma_5}{2}\right)\psi_e\,F^{\mu\nu} + \text{h.c.}\,, \tag{5.6}$$

then the limit from $g_e - 2$ experiments is much weaker; $\lambda/M_{e^*} < 1/3$ GeV.

The clearest indication of electron substructure would be the direct observation of an excited state. Such a state could be produced in e^+e^- collisions as shown in fig. 5.16, provided the mass of the state is less than the center of mass energy. The cross section for this process is calculated using the coupling given in eqn. 5.5, to be[74]

$$\frac{d\sigma}{dt} = -\frac{2\pi\alpha^2\lambda^2}{M_{e^*}^2 s^2}\left(\frac{t^2+(t-M_{e^*}^2)^2}{s} + \frac{s^2+(s-M_{e^*}^2)^2}{t} + \frac{2m_e^2 M_{e^*}^4}{t^2}\right)\,. \tag{5.7}$$

Note that the insertion of $(1-\gamma_5)/2$ as in eqn. 5.6, simply reduces the cross section by a factor of 2. The corresponding lifetime of the excited state is given by,

$$\tau = \frac{2}{\alpha\lambda^2 M_{e^*}}\,, \tag{5.8}$$

assuming that the only decay mode is $e^* \rightarrow e\gamma$. Excited states accessible by this experiment have lifetimes of the order 10^{-20} s.

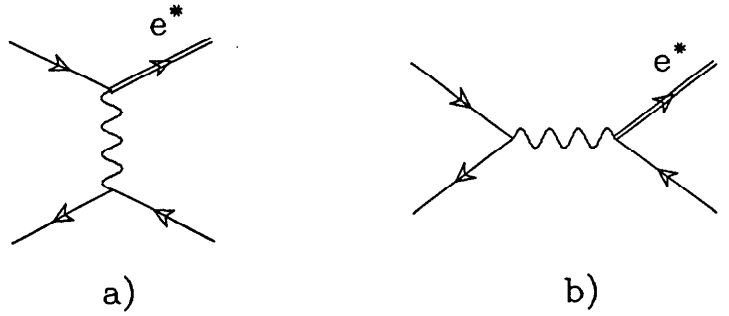

Figure 5.16. Diagrams responsible for single excited electron production. a) t-channel b) s-channel.

5.3.1 Excited electron analysis

The presence of an excited state of the electron with a mass below twice the beam energy, would cause an enhancement in the $e\gamma$ invariant mass distribution at the mass of the excited state. Radiative Bhabha events are selected using the criteria described in section 5.2.1, and the invariant mass of the wide angle $e\gamma$ is calculated using the angular measurements alone. The procedure assumes a three body final state, with the direction of the missing electron taken to be in the event plane (determined by the $e\gamma$) along the closest line to the beam direction. This gives a resolution in invariant mass of about 100 MeV/c^2, much smaller than the 700 MeV/c^2 resolution obtained with the calculation using the measured energies. Events inconsistent with the three body hypothesis, either because the visible energy is less than 16 GeV or because the calculated invariant mass is greater than the beam energy, are excluded from this analysis.

The $e\gamma$ invariant mass distribution of the QED Monte Carlo event sample is shown in fig. 5.17a, and is fit with a sixth order polynomial, to define the background to a possible excited electron signal. In fig. 5.17b, the invariant mass distribution for the data is shown, and follows the background curve well. No clear evidence is seen for an excited state of an electron with mass between 14 and 28 GeV.

A Monte Carlo program, written to generate single excited electron production events according to the cross section formula eqn. 5.7, is used to determine the sensitivity of the analysis. For various masses between 14 and 28 GeV, 2000 excited electron Monte Carlo events are generated, with a low angle electron below 100 mrad. The excited electron is taken to decay immediately into an $e\gamma$ pair, with an isotropic angular distribution in its rest frame. The invariant mass distributions of these events, are shown in fig. 5.18.

The efficiency and resolution are shown in fig. 5.19, as a function of the excited electron mass. The efficiency is low for low mass excited electron production because of the angular acceptance. The drop in the efficiency above 27 GeV, is due to the acollinearity requirement used to filter against converting two photon annihilation events.

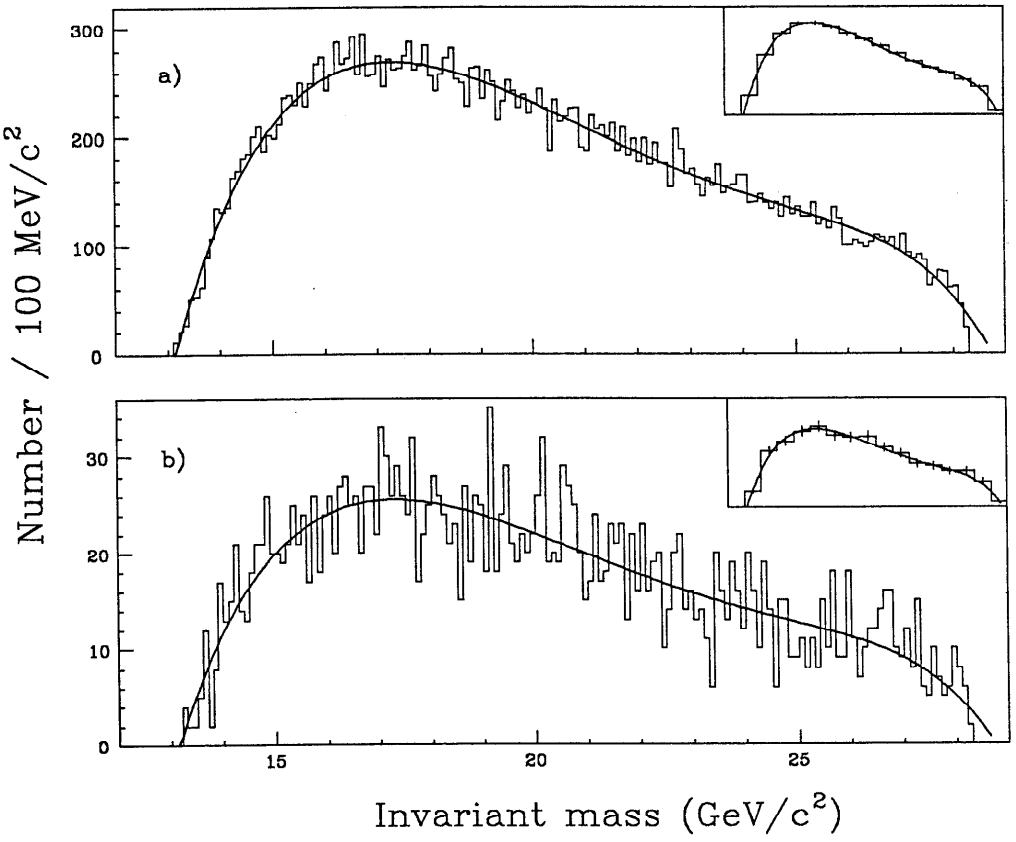

Figure 5.17. The invariant mass of the wide angle electron-photon pair. a) From the order α^4 Monte Carlo sample. A 6^{th} order polynomial is fit to this distribution to define the QED background. b) From the data sample with the QED background curve overlaid. The inserts show the same data with 1 GeV binning.

Limits on the coupling of an excited electron to an electron and photon, are determined from a likelihood analysis. A probability density function for the invariant mass distribution is defined as,

$$p(W) = (1-x)\, p_{\text{QED}}(W) + x\, p_{e^*}(W, M_{e^*}) \ , \tag{5.9}$$

where, W is the invariant mass, p_{QED} is the normalized curve shown in fig. 5.17a, p_{e^*} is a normalized Gaussian distribution centered at M_{e^*} with the width given by the curve in fig. 5.19b, and x is the fraction of all events attributed to excited electron production. For each choice of M_{e^*}, the parameter x is found by maximizing the log

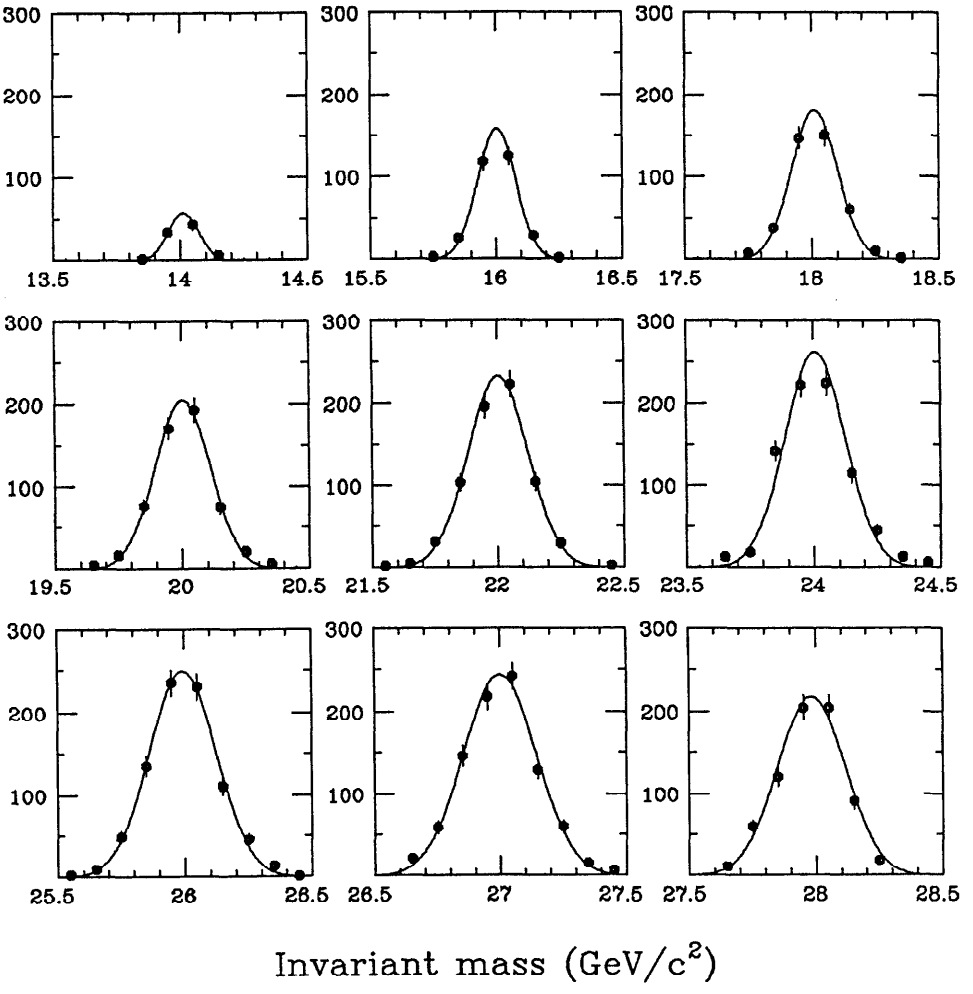

Figure 5.18. The invariant mass of the wide angle electron-photon pair for excited electron Monte Carlo events for various values of M_{e^*}. The curves are fit by Gaussian distributions to determine the resolutions.

likelihood,

$$\log L = \log \left[\prod_{i=1}^{n} p(W_i) \right] = \sum_{i=1}^{n} \log p(W_i) \ , \tag{5.10}$$

and the 95% confidence level corresponds to a change in the value by 1.35. The constraint, $x > 0$, is imposed during the maximization process.

The limits on the number of excited electron events are translated to limits on the coupling constant using the efficiency function, given by the curve in fig. 5.19a, and the total e^* production cross section. The 95% confidence level on the coupling constant for excited electron masses between 14 and 28 GeV is shown in fig. 5.20. For almost the entire region, the coupling constant, $(\lambda/M_{e^*})^2$, is below 10^{-7}, at the 95%

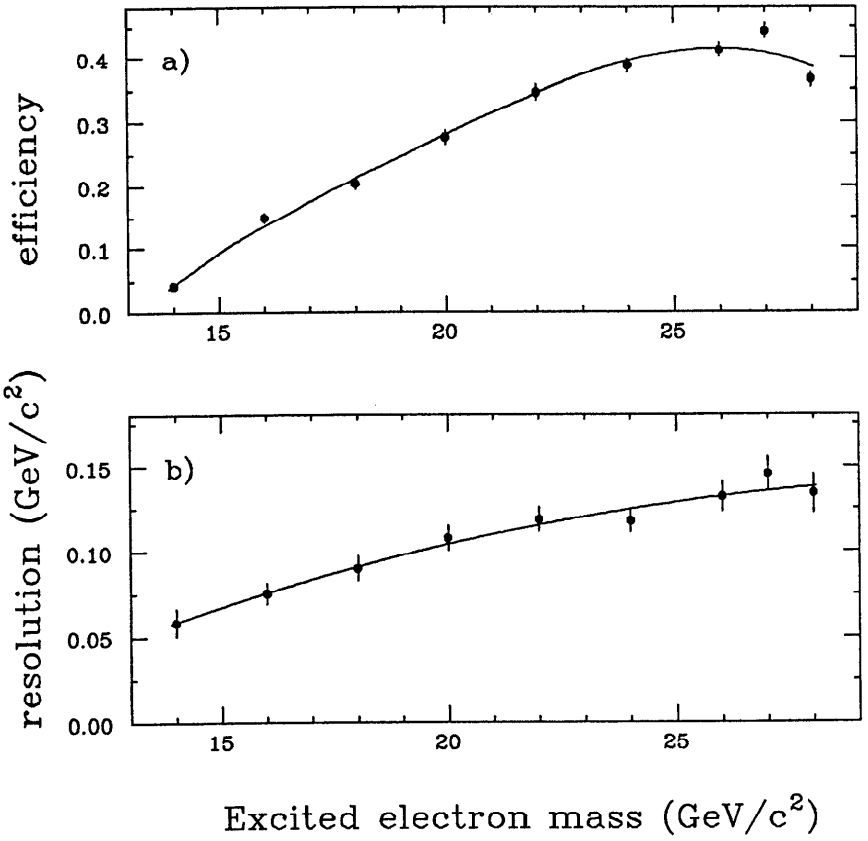

Figure 5.19. a) The efficiency of the excited electron analysis as a function of excited electron mass. The points are fit to a fourth order polynomial. b) The invariant mass resolution versus mass of the excited electron, fitted to a quadratic.

confidence level. Similar limits have been obtained by other experiments[75,76].

A limit on the substructure scale, Λ_{sub}, is ambiguous since the parameterization of the coupling constant is not unique. If the coupling constant, λ/M_{e^*}, is instead written as $1/\Lambda_{sub}$, then $\Lambda_{sub} \geq 3$ TeV. If, however, it is written as M_{e^*}/Λ^2_{sub}, as can be argued from chiral symmetry[77], then the limit is much weaker, $\Lambda_{sub} \geq 300$ GeV. These limits are only valid for the region $14 < M_{e^*} < 28$ GeV.

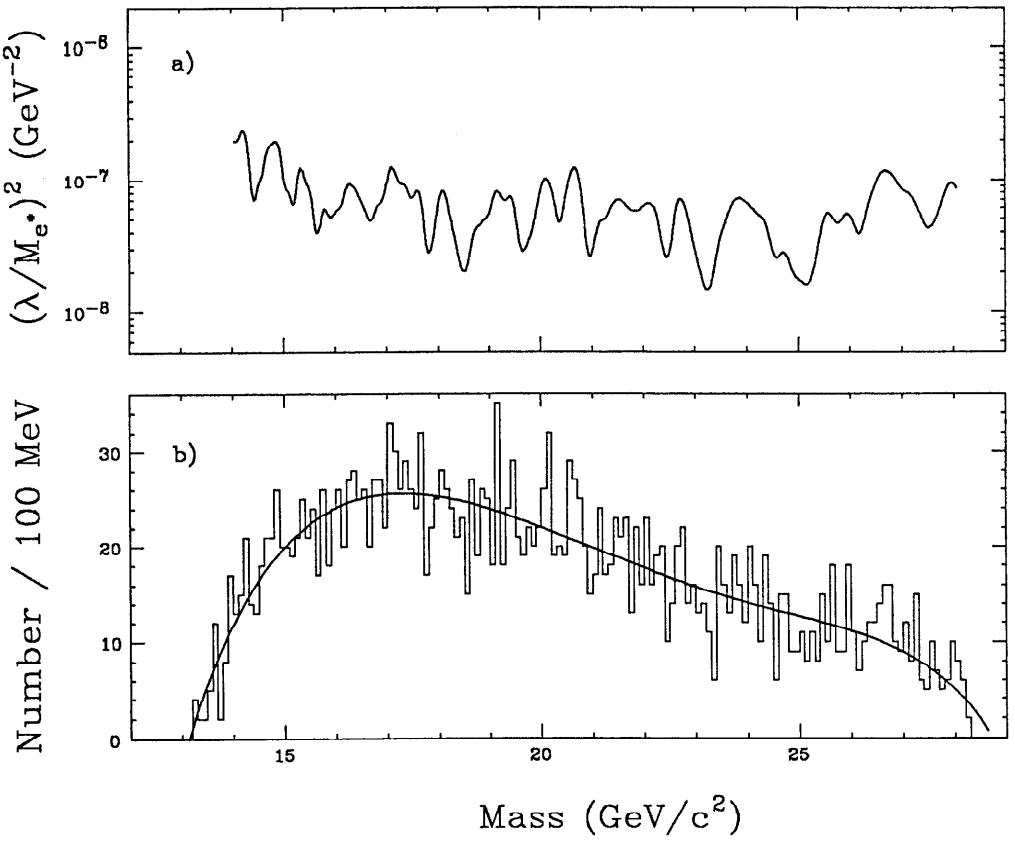

Figure 5.20. a) The 95% confidence level limits on the coupling constant between an electron and photon with an excited electron with mass between 14 and 28 GeV/c^2. b) The invariant mass distribution from the data with the QED background curve overlaid.

5.4 Analysis of double radiative Bhabha scattering

An analysis of low Q^2 double radiative Bhabha scattering is done to further test the tree level fourth order calculation. One such $(e)e\gamma\gamma$ event is shown in fig. 5.21. Typically, the second photon is much closer to the electron than shown here.

5.4.1 Selection criteria

In addition to satisfying the selection criteria described in section 5.2.1 for the general analysis, $(e)e\gamma\gamma$ candidate events must have a second neutral shower in the liquid argon acceptance of at least 300 MeV, which is separated from any other shower by more than 30 cm at the nominal trigger plane. The acollinearity and event plane angle cuts are not applied.

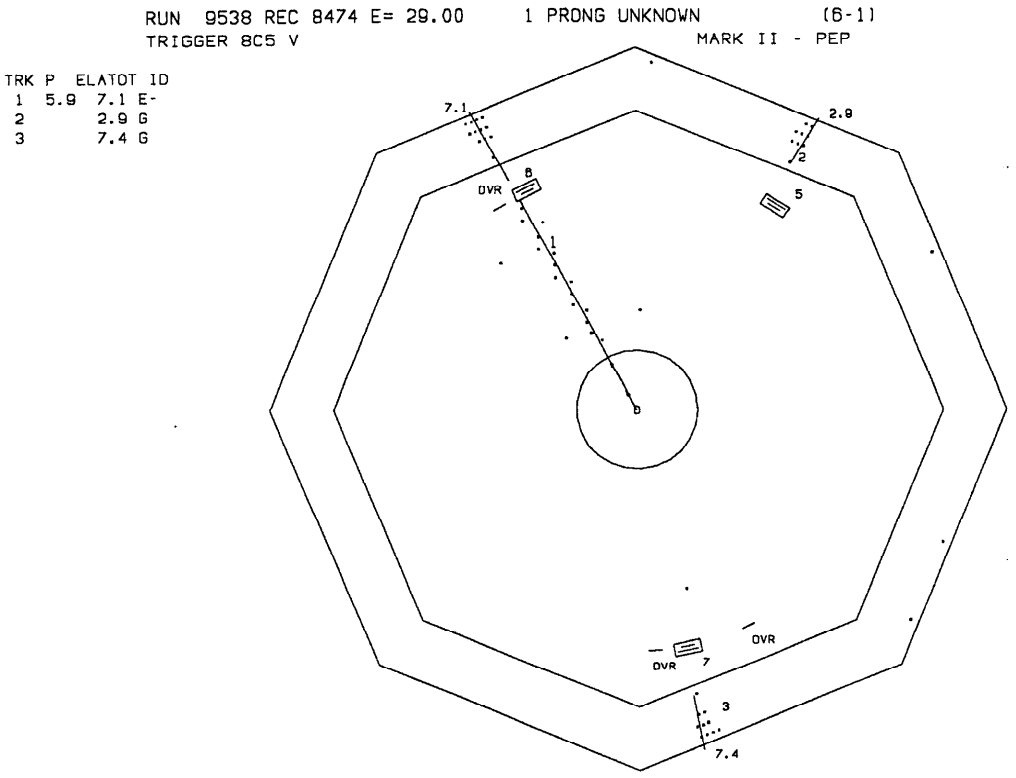

Figure 5.21. An event display of an $(e)e\gamma\gamma$ event in the Mark II detector. The energies of the roughly back to back electron and photon are measured to be 7.1 and 7.4 GeV respectively. The second photon has a measured energy of 2.9 GeV.

There are backgrounds for this topology due to problems in the reconstruction of liquid argon tracks, as discussed in section 5.2.5. In addition, events with the missing electron scattered above 100 mrad must be suppressed. To reduce these and other backgrounds, events are required to be consistent with a four body final state, with the missing electron along the beam direction. By using the angular information alone, the energies of the three observed particles can be calculated, and compared to the measured values. A simple χ^2 is calculated assuming the error in the liquid argon energy measurement is $0.145\sqrt{E}$ and in the drift chamber measurement $\sqrt{0.025^2 + (0.011\,p_\perp)^2}\,p$. The distribution, shown for both data and Monte Carlo in fig. 5.22, is wider than expected for three degrees of freedom since the energy resolution functions of are not Gaussian, and the errors in the angular quantities are

neglected. The data agree well with the Monte Carlo for low χ^2, and the cut on this quantity is arbitrarily placed at $\sqrt{\chi^2} = 6$. In section 5.4.3 below, the events rejected by this requirement are accounted for in terms of various backgrounds. The final requirement made in the event selection is that the calculated energies must each be above 300 MeV. One event was removed from the accepted sample, as described in section 5.4.3, since it has clear evidence for a second charged particle in the central detector.

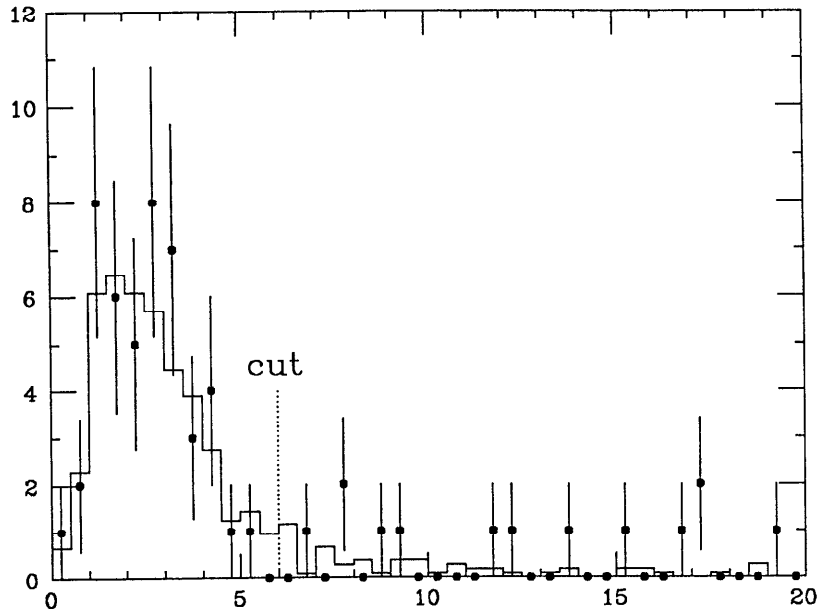

Figure 5.22. $\sqrt{\chi^2}$ distribution of fit for $(e)e\gamma\gamma$ events to a four body hypothesis. Events to the left of the cut line, are accepted in this analysis.

5.4.2 *Comparison to Monte Carlo*

Only 415 of the 105,380 Monte Carlo events referred to in section 5.2.2 pass the event selection; hence the cross section for the acceptance of this analysis is 0.188 ± 0.009 pb. No events from the lowest order Monte Carlo sample pass the selection criteria.

The angular distribution of the electrons and photons are shown with the Monte Carlo predictions in fig. 5.23. The photon distribution is similar to that for the single radiative Bhabha sample, fig. 5.11, but the electron distribution is much less peaked in the forward direction.

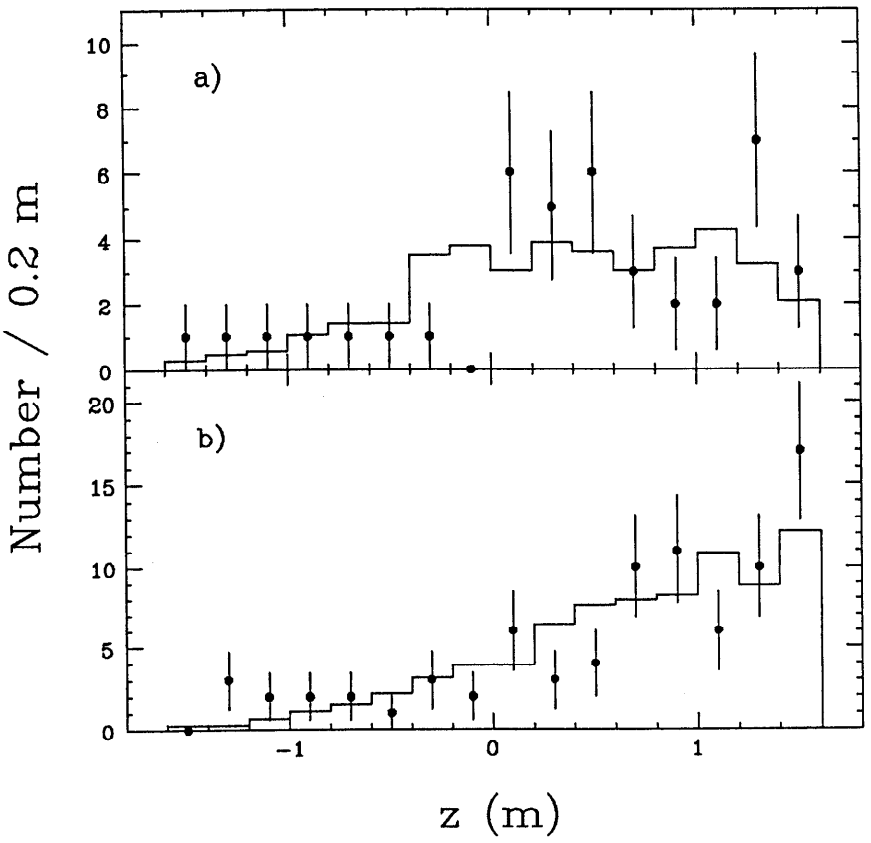

Figure 5.23. The z projection at the nominal trigger gap of the liquid argon system relative to the beam center (roughly proportional to the cosine of the polar angle). The measurements are multiplied by (-1) for events with a wide angle positron. a) electrons and positrons; b) photons (two entries per event).

The properties of the secondary photon are shown in fig. 5.24. In fig. 5.24a, the minimum azimuthal separation of the electron and a photon is given. As expected, the majority of events have one photon close to the electron. In fig. 5.24b, the second largest photon energy is shown, and for low energies, follows the expected $1/k$ distribution.

The sum of the energies of the electron and two photons is shown in fig. 5.25. Unlike the corresponding distribution from the single radiative Bhabha analysis, fig. 5.13, no events populate the region below 16 GeV. This is because of the χ^2 cut in this analysis, that removes the fifth order process with a third photon along the beam line.

Figure 5.26, shows the $e\gamma$, $\gamma\gamma$, and $e\gamma\gamma$ invariant mass distributions, calculated

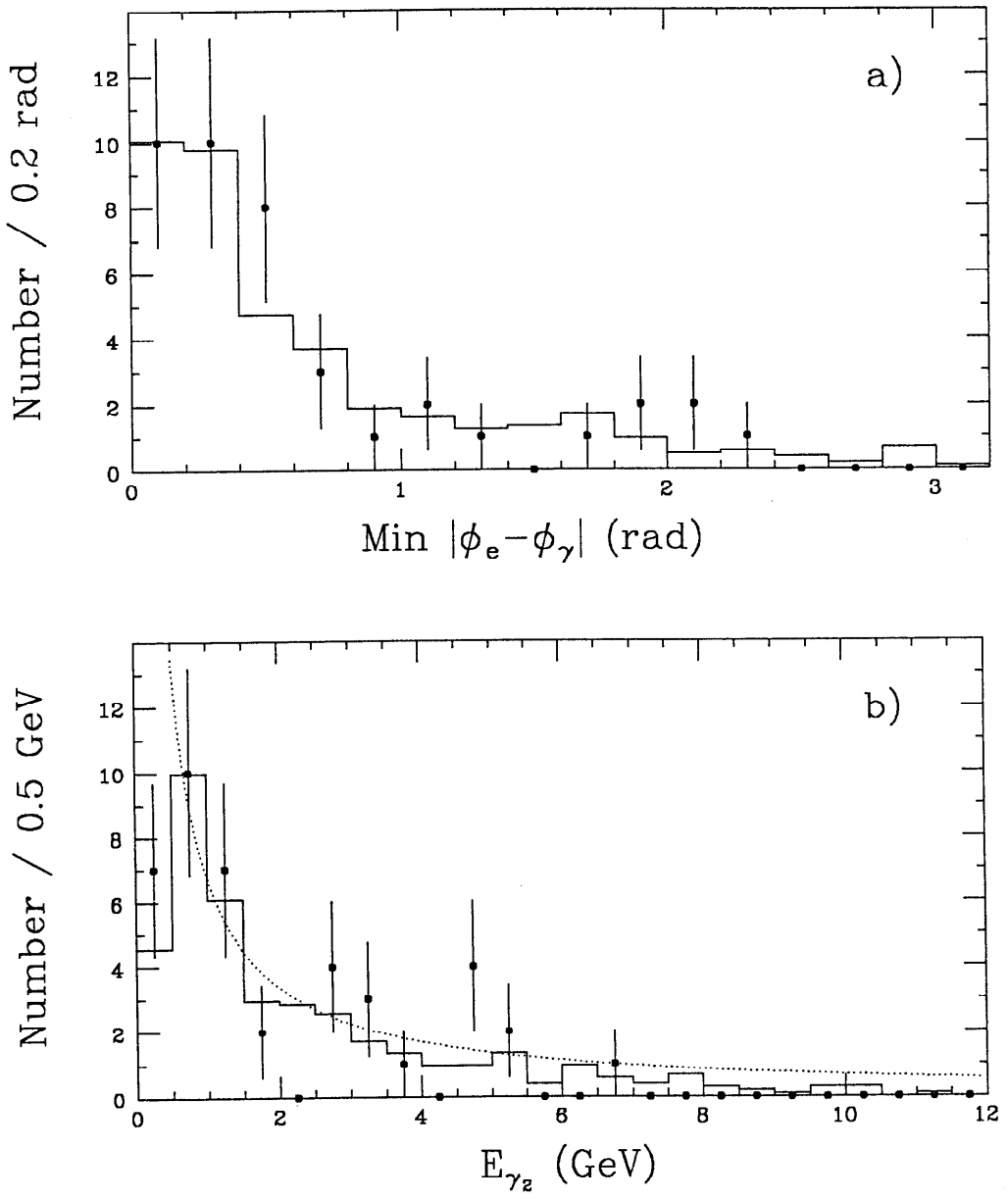

Figure 5.24. Properties of the second photon in $(e)e\gamma\gamma$ events. The data is shown by the points, and the Monte Carlo by the histograms. a) the minimum $e\gamma$ azimuthal separation; b) the second largest energy photon, compared to a $1/k$ distribution given by the dotted curve.

using the kinematically fit energies. Relatively good agreement is seen, except for the excess of events in the region above 28 GeV/c^2 in the $e\gamma\gamma$ invariant mass. This excess is considered in the next section.

Only 41 events in the Mark II data sample pass the selection criteria. In or-

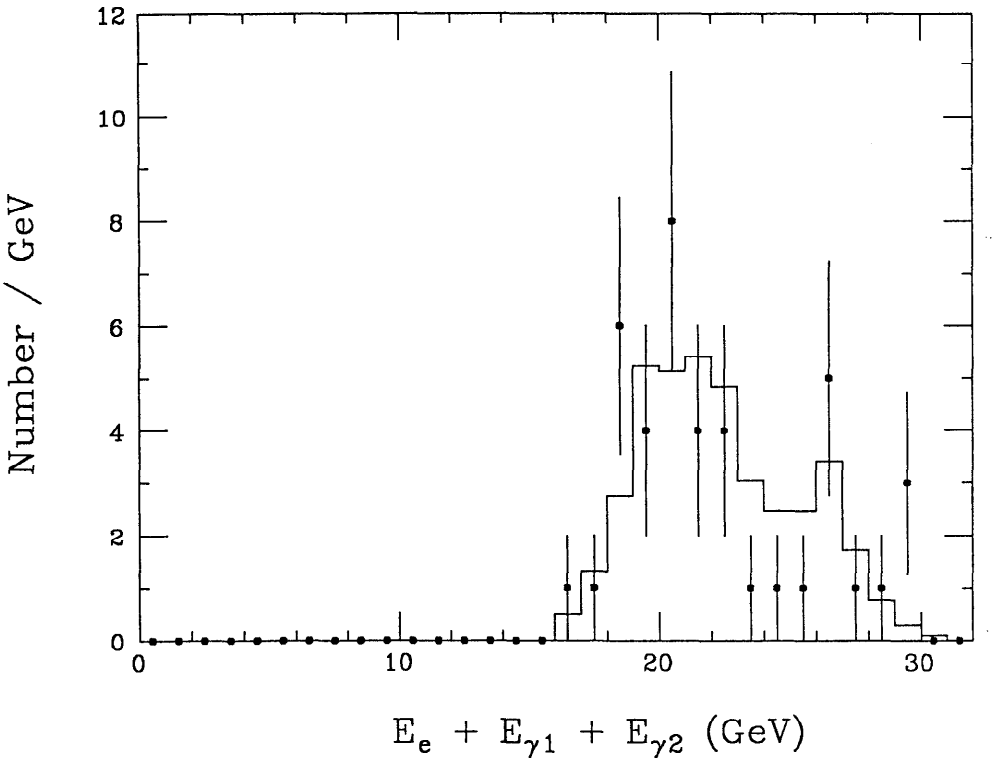

Figure 5.25. The sum of the electron and photon energies in the central detector. The points show the data, and the histogram shows the Monte Carlo prediction.

der to compare this number with that expected, the backgrounds, inefficiencies, and systematic errors are considered in the following sections.

5.4.3 *Background calculations*

Events with an unobserved electron scattered above 100 mrad must be accounted for, since they are not included in the Monte Carlo sample. The requirement that the event be consistent with a four body final state with one electron along the beam direction reduces the number of such events. A fourth order Monte Carlo sample, corresponding to an integrated luminosity of 737 pb^{-1}, with the low angle electron between 100 and 300 mrad, has only 4 events that pass the $(e)e\gamma\gamma$ selection criteria. Furthermore, in the data sample without the topology cut applied, a total of 5 events have an electron in the endcap ($\theta_e > 300$ mrad), none of which pass the χ^2 cut. The number of events accepted with $\theta_e > 100$ mrad is thus estimated to be 1 ± 1.

The background from events with both electrons more than 40° from the beam direction is evaluated using order α^3 Bhabha Monte Carlo events[23]. Two events pass

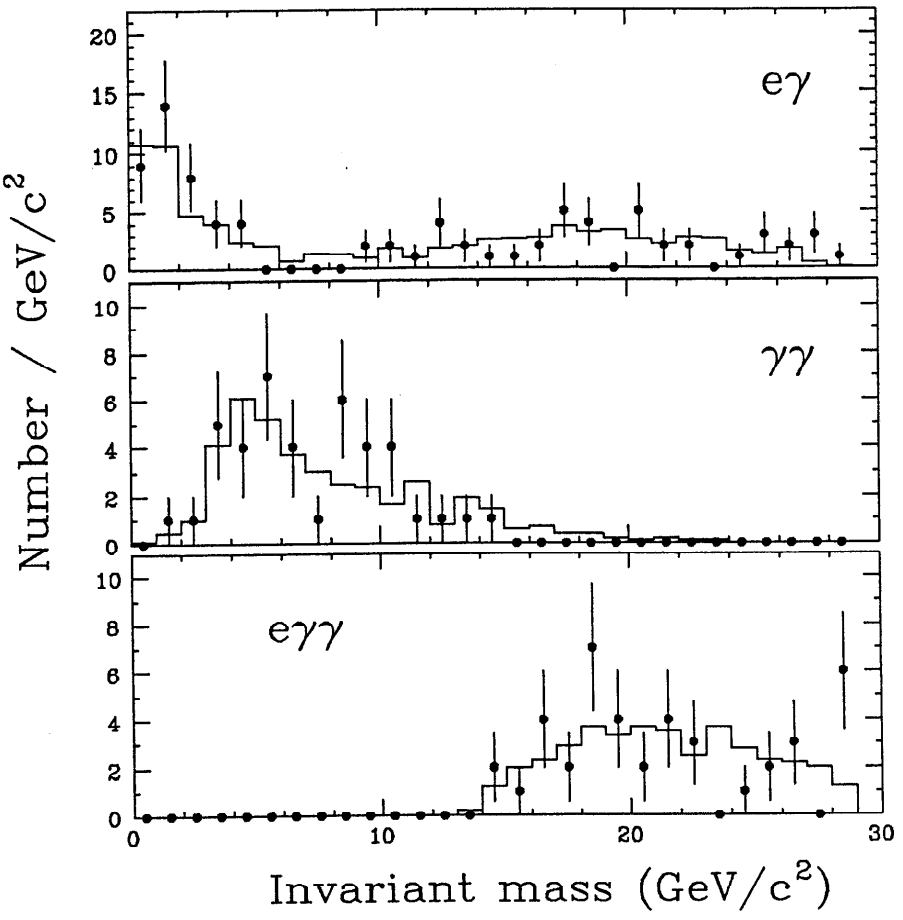

Figure 5.26. The invariant mass distributions for $(e)e\gamma\gamma$ events. The $e\gamma$ distribution has two entries per event. The data is shown by the points, and the Monte Carlo by the histograms.

the $(e)e\gamma\gamma$ selection criteria in the 90.3 pb^{-1} sample. Both events have clear evidence of an untracked electron in the drift chamber. By hand scanning the accepted data sample, one such event is found and removed from the sample.

The background due to shower reconstruction errors in $(e)e\gamma$ events, is evaluated by hand scanning the sample of events that fail the χ^2 cut. A total of 13 events are determined to be due to reconstruction problems, whereas the Monte Carlo sample predicts that there should be only 1.0 ± 0.3 such events. This difference is consistent with the estimated number lost, 12, from the $(e)e\gamma$ efficiency analysis in section 5.2.4. Of these 13 events, only 3 can be fit to the four body hypothesis, and the minimum χ^2 value is over 300. Additionally, there are a total of 8 events failing the χ^2 cut in which one or both of the photon showers are due to noise or cosmic background.

Such events are very distinctive, and none are seen in the accepted $(e)e\gamma\dot{\gamma}$ sample. Hence, no background events are expected from shower reconstruction problems.

The background from two and three photon annihilation events, $e^+e^- \rightarrow \gamma\gamma$ and $e^+e^- \rightarrow \gamma\gamma\gamma$, where one photon converts, is evaluated using Monte Carlo data[65]. Two events in a sample of 234 pb^{-1} are $(e)e\gamma\gamma$ candidates, but only one event is consistent with the four body final state and passes the χ^2 cut. To check this calculation, the analysis is modified as described in section 5.2.3, to select such events which convert in the material between the vertex and main drift chambers. In the data there are 9 conversion events that would be $e\gamma\gamma$ candidates if there were cells hit in the vertex chamber. Of these, 3 events can be fit, each passing the χ^2 cut, but one event has a fitted photon energy less than 300 MeV. From the Monte Carlo, the number of candidate events is estimated to be 16 ± 4, of which 5.4 ± 2.2 events are expected to pass the χ^2 and minimum energy criteria. Again the Monte Carlo predicts a slightly larger background from this source, just as in section 5.2.3. The total number of background events from this source is thus estimated to be 1 ± 1. Events from this background have an $e\gamma\gamma$ invariant mass of nearly 29 GeV/c^2, and hence help explain the excess in the rightmost bin of fig. 5.26.

The background from next order events, $(e)e\gamma\gamma(\gamma)$, has not been evaluated. Just as in the single radiative Bhabha analysis, the dominant effect is the additional events with a hard photon along the beam direction opposite the low angle electron. In the data sample 10 such events are observed, characterized by visible energies less than 14 GeV. All 10 of these events, one of which is shown in fig. 5.27, fail the χ^2 cut.

Table 5.6 summarizes the events that fail the fit to the four body final state. The fact that all the rejected events have a clear interpretation or are otherwise accounted for, confirms that the most important background processes have been considered.

5.4.4 *Efficiency and systematic error calculations*

Since much of this analysis is the same as the single radiative Bhabha analysis presented in section 5.2, many of the same efficiency and systematic error estimates are used here.

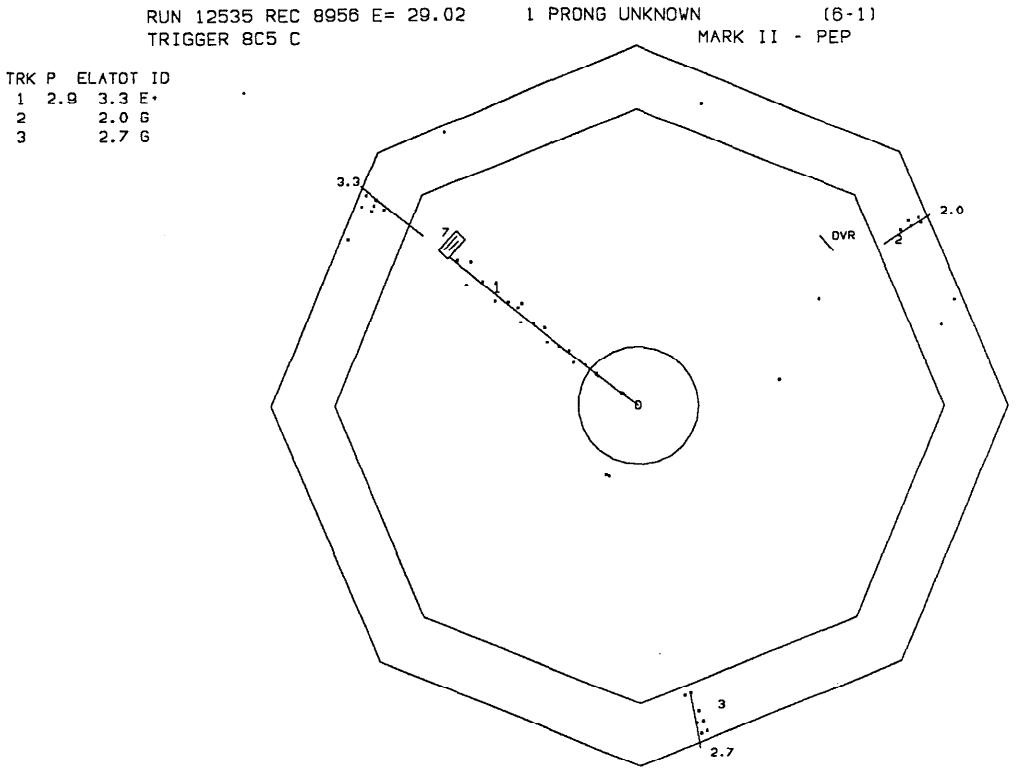

Figure 5.27. An event display of a triple radiative Bhabha event, where all particles are separated by large angles. The positron and two photon energies are 3.3, 2.7, and 2.0 GeV respectively. An electron and a third photon are along the beam line in opposite directions.

The total inefficiency of the analysis that is not simulated for the Monte Carlo data is that of the trigger and drift chamber occupancy requirements. In section 5.2.4, these inefficiencies are shown to be 0.6%.

The systematic uncertainty from simulating the hardware filter track requirements is again 0.5%. The hardware filter energy sum is fully efficient, since the events have visible energies of at least 16 GeV. The remaining systematic uncertainties of the previous measurement apply here.

The dominant systematic uncertainty is in the simulation of the four body topology requirement. The χ^2 distribution is well matched by the Monte Carlo, as seen in

Table 5.6. Summary of $e\gamma\gamma$ events that do not pass the kinematical fit to a four body hypothesis. The event types are determined by inspecting the event display information.

Event type	#	expect	comments
Higher order	10	-	visible energy < 14 GeV order α^5 correction not calculated
Electron in endcap	5	-	no Monte Carlo sample for $\theta_e > .3$ rad
Converting $e^+e^- \to \gamma\gamma$	3	.9±.9	calculated from Monte Carlo
Shower reconstruction errors	13	12±6	inefficiency in $(e)e\gamma$ measurement
LA noise / false photons	8	-	misidentified single e and $e\gamma$ events
Low energy two prong	1	-	clear background event with one very low momentum untracked prong
No obvious problem	18	17±2	calculated with Monte Carlo, $\theta_e < .3$ rad rejected because of poor energy measurements or $p_\perp$ of low angle electron

fig. 5.22. From table 5.6, the number of events rejected by this cut with no obvious problem is 18, compared with the Monte Carlo simulation of 17±2. The systematic uncertainty is hence estimated to be the equivalent of 2 events.

5.4.5 *Summary of cross section measurement*

Table 5.7 summarizes the results of the cross section measurement of low Q^2 double radiative Bhabha scattering. The total cross section is $0.187 \pm 0.029 \pm 0.011$ pb in excellent agreement with the calculated value of 0.188 ± 0.009 pb. The ratio of measured to calculated cross sections is $R = 0.99 \pm 0.16 \pm 0.08$, where the first error is statistical and the second is systematic.

Table 5.7. Summary of the measurement of the $(e)e\gamma\gamma$ cross section. The inefficiencies listed are those not included in the detector simulation. The uncertainty in the background calculation is included in the total systematic error. The z scale uncertainty, separated from the total systematic uncertainty, is partially cancelled in the ratio with the measured luminosity. Listed with the measured cross section are, in order, the statistical, systematic, and z scale uncertainties.

Number of events	41±6.5
Background	
wide angle $e^+e^- \to e^+e^-\gamma$	1±1
converting $e^+e^- \to \gamma\gamma$	1±1
Total Background	2±1.4
Inefficiency	
trigger	0.25%
drift cell occupancy	0.15%
vertex layer occupancy	0.2%
Total Inefficiency	0.6%
Systematic error	
hardware filter: track cuts	0.0±0.5%
track - shower association	0.0±0.5%
z scale	0.4±2.1%
z offset	0.0±0.3%
topology requirement	0.0±4.9%
background uncertainty	0.0±3.3%
Total Systematic error	0.4±6.0±2.1%

Corrected no. of events	39.1	±	6.1	±	2.3	±	0.8
Luminosity (pb^{-1})	209.2	±	0.5	±	1.3	±	2.6
Cross section (pb)	0.187	±	0.029	±	0.011	±	0.002

5.5 Conclusions

The calculations and subsequent measurement of low Q^2 radiative Bhabha scattering presented in this thesis are in excellent agreement. The total $e\gamma$ cross section, measured to a precision of 2.3%, is a sensitive test of the fourth order radiative correction. The measurement of exclusive double radiative Bhabha scattering is less accurate, with a statistical uncertainty of 16%, but is also a strong test of the calculations, since it represents only 1 event for every 4000 wide angle Bhabha events. The agreement indicates that the approximations used in calculating the radiative correction are valid to the accuracy of this measurement, and that no new electron-photon interactions are seen.

The figures shown in this chapter, comparing quantities integrated over the complicated detector acceptance, may not be useful for other experiments. Instead, the calculations, as embodied in the Monte Carlo event generator program, represent the most important products of this work. The program should be very useful in the analysis of future experiments for neutrino generation counting and searches for new particles.

References

1. S. L. Glashow, *Nucl. Phys.* **22**, 579 (1961)

2. S. Weinberg, *Phys. Rev. Lett.* **19**, 1264 (1967)

3. A. Salam and J. C. Ward, *Phys. Lett.* **13**, 168 (1964)

4. There are many sources of information on grand unified theories. An excellent introduction to the subject is found in:
J. L. Rosner, in *Proceedings of the Second Lake Louise Winter Institute on New Frontiers in Particle Physics*, edited by J. M. Cameron, *et al.* (Lake Louise, Canada, 1987), pp. 91-170

5. E. Ma and J. Okada, *Phys. Rev. Lett.* **41**, 287 (1978); **41**, 1759(E)(1978)

6. K. Gaemers, R. Gastmans and F. Renard, *Phys. Rev.* **D19**, 1605 (1979)

7. G. Barbiellini, B. Richter and J. L. Siegrist, *Phys. Lett.* **B106**, 414 (1981)

8. D. L. Burke, in *Proceedings of the Theoretical Advanced Study Institute in Elementary Particle Physics*, edited by H. .E. Haber (University of California, Santa Cruz, 1986), pp. 497-540

9. M. K. Gaillard, I. Hinchliffe and L. Hall, *Phys. Lett.* **B116**, 279 (1982)

10. P. Fayet, *Phys. Lett.* **B117**, 460 (1982)

11. J. Ellis and J. Hagelin, *Phys. Lett.* **B122**, 303 (1983)

12. M. Chen, C. Dionisi, M. Martinez, and X. Tata, CERN preprint EP/87-143, submitted to Physics Reports (1987)

13. H. Terazawa, M. Yasuè, K. Akama and M. Hayashi, *Phys. Lett.* **B112**, 387 (1982)

14. K. Hagiwara and D. Zeppenfeld, *Z. Phys.* **C29**, 115 (1985)

15. A. Courau and P. Kessler, *Phys. Rev.* **D33**, 2024 (1986)

16. D. Karlen, *Nucl. Phys.* **B289**, 23 (1987)

17. S. J. Brodsky and S. D. Drell, *Ann. Rev. Nucl. Sci.* **20**, 147 (1970)

18. S. D. Drell, *Physica* **96A**, 3 (1979)

19. T. Kinoshita and J. Sapirstein, Cornell preprint CLNS-84/617 (1984)

20. C. Kiesling, in *Proceedings of the 20$^{\text{th}}$ Recontre de Moriond*, edited by J. Tran Thanh Van (Les Arcs, France, 1985), pp. 65-86

21. S. M. Swanson, *Phys. Rev.* **154**, 1601 (1967)

22. A. C. Hearn, P. K. Kuo and D. R. Yennie, *Phys. Rev.* **87**, 1950 (1969)

23. F. A. Berends and R. Kleiss, *Nucl. Phys.* **B228**, 537 (1983)

24. J. D. Bjorken and S. D. Drell, *Relativistic Quantum Mechanics*, (McGraw-Hill, New York, 1964)

25. A. C. Hearn, computer code REDUCE Version 3.2, (The Rand Corporation, Santa Monica, CA, 1985)

26. F. A. Berends, P. De Causmaecker, R. Gastmans, R. Kleiss, W. Troost and T. T. Wu, *Nucl. Phys.* **B264**, 265 (1986)

27. M. Martinez and R. Miquel, UAB-LFAE preprint 87-01 (1987)

28. É. A. Kuraev and A. N. Përyshkin, *Sov. J. Nucl. Phys.* **42**, 756 (1985)

29. G. Bonneau and F. Martin, *Nuovo Cim.* **21A**, 611 (1974)

30. V. Gorgé, M. Locher and H. Rollnik, *Nuovo Cim.* **27**, 928 (1963)

31. F. Bloch and A. Nordsieck, *Phys. Rev.* **52**, 54 (1937)

32. F. A. Berends, P. H. Daverveldt and R. Kleiss, *Nucl. Phys.* **B253**, 421 (1985)

33. M. Landrø, K. J. Mork and H. A. Olsen, *Phys. Rev.* **D36**, 44 (1987)

34. W. L. van Neerven and J. A. M. Vermaseren, *Phys. Lett.* **B142**, 80 (1984)

35. Y. S. Tsai, *Phys. Rev.* **120**, 269 (1960)

36. Ó. Klein and Y. Nishina, *Z. Phys.* **52**, 853 (1929)

37. L.M. Brown and R.P. Feynman, *Phys. Rev.* **85**, 231 (1952)

38. D. R. Yennie, S. C. Frautschi and H. Surra, *Ann. Phys.* **13**, 379 (1961)

39. K. J. Mork, Ph.D. thesis, University of Trondheim (1963)

40. K. J. Mork, *Phys. Rev.* **A4**, 917 (1971)

41. K. J. Mork, private communication

42. F. Mandle and T. H. R. Skyrme, *Proc. Roy. Soc.* **A215**, 497 (1952)

43. J. M. Jauch and F. Rohrlich, *The Theory of Photons and Electrons*, (Springer Verlag, New York, 1955), p. 237

44. J. M. Hammersley and D. C. Handscomb, *Monte Carlo Methods*, (Methuen, London, 1964)

45. F. James, *Rep. Prog. Phys.* **43**, 1145 (1980)

46. J. R. Ehrman, *The Care and Feeding of Random Numbers*, unpublished (1981)

47. G. R. Ferrar and F. Neri, *Phys. Lett.* **B130**, 109 (1983)

48. M. Caffo, R. Gatto and E. Remiddi, *Phys. Lett.* **B173**, 91 (1986)

49. M. Caffo, R. Gatto and E. Remiddi, *Nucl. Phys.* **B286**, 293 (1987)

50. C. Mana and M. Martinez, *Nucl. Phys.* **B287**, 601 (1987);
F. A. Berends, private communication

51. G. Bartha, *et al.*, *Phys. Rev. Lett.* **56**, 685 (1986)

52. B. W. LeClaire, Ph.D. thesis, Stanford University, SLAC-Report-321 (1987)

53. R. H. Schindler, Ph.D. thesis, Stanford University, SLAC-Report-219 (1979)

54. K. Kleinknecht, *Phys. Rept.* **84**, 85 (1982)

55. J. A. Jaros, in *Proceedings of the International conference on Instrumentation for Colliding Beam Physics*, edited by W. Ash (Stanford Linear Accelerator Center, Stanford, CA, 1982), pp. 29-33

56. W. Davies-White, *et al.*, *Nucl. Instr. and Meth.* **160**, 227 (1979)

57. G. Abrams, *et al.*, *IEEE Trans. Nucl. Sci.* **NS-25**, 309 (1978); **NS-27**, 59 (1980)

58. R. L. Ford and W. R. Nelson, computer code EGS Version 3 (Stanford Linear Accelerator Center, Stanford, CA, 1978)

59. B. D. Milliken, private communication

60. F. James and M. Roos, *Comp. Phys. Comm.* **10**, 343 (1985)

61. J. R. Smith, Ph.D. thesis, U. of California, Davis (1982)

62. H. J. Bhabha, *Proc. Roy. Soc.* **A154**, 195 (1935)

63. F. A. Berends and R. Kleiss, *Nucl. Phys.* **B177**, 239 (1981)

64. F. A. Berends, R. Kleiss and S. Jadach, *Nucl. Phys.* **B202**, 63 (1982)

65. F. A. Berends and R. Kleiss, *Nucl. Phys.* **B186**, 22 (1981)

66. M. L. Perl, *et al.*, *Phys. Rev.* **D34**, 3321 (1986)

67. L. Lyons, *Prog. Part. and Nucl. Phys.* **10**, 227 (1983)

68. M. E. Peskin, in *Proceedings of the 1981 International Symposium on Lepton and Photon Interactions at High Energies*, edited by W. Pfeil (University of Bonn, Federal Republic of Germany, 1981), pp. 880-907

69. E. J. Eichten, K. D. Lane and M. E. Peskin, *Phys. Rev. Lett.* **50**, 811 (1983)

70. F. E. Low, *Phys. Rev. Lett.* **14**, 238 (1965)

71. S. Narison, *Phys. Lett.* **B167**, 214 (1986)

72. F. Combley, *et al.*, *Phys. Rept.* **68**, 93 (1981)

73. F. M. Renard, *Phys. Lett.* **B116**, 264 (1982)